Imperial College London
Department of Electrical and Electronic Engineering

Completely Wireless Infrastructure for Distributed mm-sized Neural Implants

Peilong Feng

Submitted in part fulfilment of the requirements for the degree of
Doctor of Philosophy in Electrical and Electronic Engineering of
Imperial College London, 31st January 2020

Declaration

I hereby certify that all material in this dissertation which is not my own work has been properly acknowledged.

Peilong Feng

Copyright

The copyright of this thesis rests with the author and is made available under a Creative Commons Attribution Non-Commercial No Derivatives licence. Researchers are free to copy, distribute or transmit the thesis on the condition that they attribute it, that they do not use it for commercial purposes and that they do not alter, transform or build upon it. For any reuse or redistribution, researchers must make clear to others the licence terms of this work.

Peilong Feng

Abstract

Life-threatening medical conditions such as stroke, spinal injuries and traumatic brain injury affects millions of people worldwide. The emerging prospect of neural interfaces provides hope for these patients to regain their ability through treatment. Current examples of neural interfaces have proven their potential, with paralysed patients demonstrating control of robotic wheelchairs and prosthesis through the use of these such devices. Neural interfaces have also served as crucial research tools for neuroscientists working on deciphering the secrets of the human brain in order to reveal the causes of neurological and psychiatric disorders. However, current challenges of neural implants are tissue inflammation and cell death, which are caused by large tethered bulky centralised implanted devices. In order to reduce these detrimental effects, the prevalent concept of next-generation neural interfaces are free-floating distributed millimetre-scaled or sub- millimetre-scaled implants.

This work explores the feasibility of wireless connections for distributed mm-scale neural implants, proposes a novel efficient wireless power transfer, and demonstrates an innovative method of multiple access data communication. The original contributions of this work are summarised as three aspects.

Contribution 1: The selection of receiving coils is critical to the wireless connections of implantable medical devices. It determines the capability of wireless systems for electromagnetic energy delivery and data communication. To the best of author's knowledge, **this work** is the first time to thoroughly compare three types of millimetre-scale CMOS-compatible coils from three perspectives: electromagnetic characteristics, manufacturability and mechanical stability. Consequently, the microfabricated coil is selected as the receiving implantable coil, instead of wire-wound and CMOS coils, because of its excellent electrical properties and stable mechanical structure.

Contribution 2: Inductive links and power management units are the key components in wireless power transmission systems for efficient power transfer and stable power supply. **This work** proposes the passive resonant arrays where are placed in multiple coupled inductive links. They boost the received voltage two times and extend power coverage four times, compared to the conventional inductive link without the resonant arrays. In addition, innovative

self-regulated power management is proposed to solve unpredictable misalignments between transmitter and distributed receivers.

Contribution 3: The low power multiple access data communication system ensures that hundreds of distributed implants simultaneously transmit recoding signals to an external receiver. **This work** demonstrates the backscatter-based data communication technique for multiple passive implantable devices. The multiple access data communication systems achieve 1.25 Mbps data rate per node and 1 mW power consumption per passive device. In addition, the autonomous SoC with the ASK data modulator proves the feasibility of two data carriers detection, which indicate a new direction for passive, low-power, multi-access implantable medical devices.

I envision that this work could eventually be further developed into general purpose wireless infrastructure for implantable medical devices or wearable devices.

Acknowledgements

I would like to express my sincere gratitude to my supervisor Dr Timothy Constandinou. From my masters to my doctoral studies, he has consistently given me patient guidance, insightful advice as well as warm encouragement. I would also like to thank him for giving me a valuable opportunity to be his student. I can still remember the joy I felt receiving my PhD offer letter four years ago like it happened yesterday. It changed my life and allowed me to embark on an enriching academic career, and drastically altered my original path as a coal mine engineer.

I would like to thank all my colleagues from the Next-Generation Neural Interfaces (NGNI) Lab and Centre for Bio-Inspired Technology, Imperial College London. It has been extremely pleasurable to work and study with everyone, and I have had an unforgettable four years with you. Thank you so much, and I will never ever forget you all no matter what happens. Also, I would like to express my gratitude to Darly for proofreading my thesis.

I would like to thank my family for the endless love and support during my life. I would like to thank my wife for the wonderful daughter she has given me.

Contents

1 Introduction **1**

1.1 Motivation 3

1.2 Technical Challenges 7

1.3 Research Objectives 9

1.4 Thesis Outline 10

2 Literature Review **13**

2.1 Historical Review of EM Transmission 13

2.2 Wireless Power Transfer 15

2.3 Wireless Data Communication 31

3 Chip-Scale Receiving Coils for Millimetre-Sized Bio-Implants **34**

3.1 State of the art 35

3.2 Analytical Model 37

3.3 Coil Design and Fabrication 42

3.4 Results 51

3.5 Discussion 59

3.6 Summary 62

4 EM-Lens Enhanced WPT and Autonomous Power Management 64

4.1 ENGINI System Overview 65

4.2 EM-Lens Enhanced Wireless Power Transfer 67

4.3 AC-DC Conversion Components 78

4.4 Inductive Link and Rectifier Co-design 85

4.5 Self-Regulated Power Management 88

4.6 Measured Results 92

4.7 Summary 94

5 Multi-Node Data Transmission for Implantable Medical Devices 96

5.1 Multiple Access for Multiple Implantable Devices 97

5.2 Wireless Information and Power Transmission 98

5.3 Autonomous SoC for Wireless Data Communication 104

5.4 Summary 108

6 Conclusions and Future Work 110

6.1 Original Contributions 111

6.2 Future Work 112

6.3 Concluding Remarks 113

Bibliography 114

A Abbreviations **134**

B Publications **137**

List of Tables

2.1 Comparison of various electromagnetic power transfer methods. 18

3.1 Comparison between planar spiral coil and solenoid. 37

3.2 Coefficients for in-CMOS and above-CMOS coil inductance calculation. 41

3.3 Optimal geometries and electrical properties of Rx coils. 44

3.4 Comparison between around-CMOS, above-CMOS, and in-CMOS coils. 60

3.5 Comparison between different types of mm-scale Rx coils. 61

4.1 Design geometry and electrical properties of the proposed two-tier inductively coupled WPT system. 73

5.1 Comparison between different coding techniques. 98

List of Figures

1.1 Neural interface development timeline. 2

1.2 Various types of neural interfaces from non-invasive to invasive. 4

1.3 Comparison between non-invasive and invasive neural interfaces. 5

1.4 Current development of multielectrode arrays from wired connections to wireless interfaces. 7

1.5 Thesis structure is displayed into wireless information and power transmission system. 12

2.1 Typical wireless power transfer techniques for implantable medical devices . . . 16

2.2 Block diagram of conventional 2-coil inductive link 19

2.3 Power transfer efficiency of entire inductive coupled power transmission system. 19

2.4 Inductive link theory - reflected load model 21

2.5 Inductive link theory - two-port network model 23

2.6 Examples of electromagnetic power transfer systems for distributed implants . . 26

2.7 Examples of ultrasonic power transfer systems for distributed implants 30

3.1 Examples of mm-scale around-CMOS coils 36

3.2 Examples of mm-scale above-CMOS and in-CMOS coils 37

3.3 3D models and equivalent circuit models for around-CMOS, above-CMOS, in-CMOS coils 38

3.4 Cross-section of the HFSS simulation model 43

3.5 Equivalent circuit models for 2-coil inductive link and Rx coil with a silicon substrate 46

3.6 Iterative design procedure for 2-coil link PTE optimisation under constrained SAR. 47

3.7 Simulated SAR in head model at optimal frequencies for in-CMOS, around-CMOS and above-CMOS coils with fixed 10 mW Tx power. 49

3.8 Process steps of the above-CMOS (micro-fabricated) coil. 51

3.9 Fabricated around-CMOS; above-CMOS; and in-CMOS coils 51

3.10 In air measurement setups for Rx coil characterisation 53

3.11 *Ex vivo* measurement setups for 2coil link characterisation 54

3.12 In air measured, simulated and calculated results of three different types of CMOS-based Rx coils 55

3.13 *Ex vivo* measured, simulated and calculated results of around-CMOS, above-CMOS, and in-CMOS coils 56

3.14 Measured PTE of 2-coil inductive links to deliver power to the 4 mm×4 mm around-CMOS, above-CMOS, and in-CMOS Rx coils. 60

3.15 Cross-section of Around-CMOS, Above-CMOS, and In-CMOS coils. 61

3.16 Different concepts for probe integration with mm-scale coils 62

4.1 System architecture of the 2-tier inductively coupled network. 66

4.2 Equivalent circuit models for proposed EM-lens enhanced WPT system 67

4.3 Cross-section of HFSS 3D simulation model for EM-lens enhanced WPT system 69

4.4 Optimisation process of 2-tier inductively coupled WPT system to achieve reasonable PTE and uniform power distribution. 71

4.5 Optimal operating frequency of ENGINI wireless power transfer system 72

4.6 The maximum PTE and PDD across the 18 mm×18 mm covered area for different unit cell spacings d_{unit} within the multiple coil array. 74

4.7 Comparison of simulated PTE and PDD between conventional 2-coil link and the proposed 2-tier inductive link 75

4.8 Measurement setup for EM-lens enhanced WPT 76

4.9 Measured results of return loss about Tx, EM-lens and Rx. 77

4.10 Measured results of EM-lens enhanced WPT 78

4.11 Various AC-DC converter topologies 79

4.12 Schematics of two passive full-wave rectifier 81

4.13 Simulated results for three different rectifiers 82

4.14 Chip microphotograph of cross-coupled rectifier, standard threshold and low threshold diode-connected rectifiers 83

4.15 Experimental setup of PCE evaluation in terms of operating frequency. 84

4.16 Measured PCE of cross-coupled rectifier, standard threshold and low threshold diode-connected rectifiers. 85

4.17 Inductive link and rectifier equivalent circuit model. 86

4.18 Simulated PCE in terms of W/L and input power. 89

4.19 Proposed self-regulated power management system 90

4.20 Schematic of supply voltage detector and state diagram of auto-tune finite-state machine. 91

4.21 Digital tune capacitor schematic. 93

4.22 Measured reflection coefficient of the secondary LC tank to show its self-resonant frequency. Insets depict the transfer above-CMOS coil integration with active CMOS chip. 93

4.23 ENGINI chip microphotograph with a close-up of the electronic subsystem. . . . 94

4.24 Measurement results of ENGINI chip 95

5.1 Comparison between FDMA, TDMA,and CDMA. 97

5.2 Proposed architecture of EM-lens enhanced wireless power transfer and multiple nodes data communication system for implantable medical devices. 99

5.3 Simplified block diagram of external devices, implanted wireless interface and equivalent circuit model of EM-lens. 100

5.4 Experiment setup and Rx power consumption breakdown. 102

5.5 Time diagram of 2-node backscatter-CDMA data communication 103

5.6 System architecture of autonomous SoC for wireless data communication. 105

5.7 Simulated results of entire wireless data communication system. 106

5.8 Experimental setup and chip microphotograph. 107

5.9 Measured spectrum of induced Rx voltage at the secondary LC tank. 108

Chapter 1

Introduction

"The brain is the most complex and least understood organ in the human body."

– Medical Research Council, 2009

Brain-computer interfaces are defined as physical connections between the brain and electronic devices. On the other hand, the term 'neural interface' is a broader definition of brain-computer interfaces. It refers to the interactions between the central or peripheral nervous system with external devices.

The origins of neural interfaces can be traced back to ancient Egypt and Rome, where records show the use of electric catfish to treat arthritis and headaches [1]. In modern scientific research, the earliest experiments on bio-electric collars were recorded in 1780. Italian biologist Luigi Galvani discovered that the leg muscles of frogs would tremble when they were exposed to electric sparks [2]. He became one of the first few people involved in the field of bio-electricity. In the 1860s, Gaiffe's transcutaneous electrical nerve stimulation (TENS) became the world's first neural stimulation device [3]. In 1875, British physiologist Dr Richard Caton successfully performed the first electroencephalography (EEG) recording on rabbits, cats and monkeys using a galvanometer [4]. The human EEG was first published by the German psychiatrist Hans Berger between 1929 and 1938 [5]. In 1952, Spanish neuroscientist Jose M Delgado discovered that electrically stimulating the brain affected the emotions and behaviours of animals and

humans [6].

In 1961, American otologist William House invented the cochlear implant and successfully performed patient implantation in 1969 [7]. Many neurostimulation-based medical devices emerged in the 1990s. The US Food and Drug Administration approved deep brain stimulation (DBS) for the treatment of Parkinson's disease in 1997 [8], DBS for dystonia in 2003 [8], the Argus II retinal implant system in 2013 [9], and DBS for epilepsy in 2018 [10].

At the same time, neural recording systems also made significant progress. In 1988, EEG signals could be used to control robotic movement [11]. In 2005, an invasive neural interface called Braingate was first applied to quadriplegic patient Matt Nagle to control a computer cursor [12]. In 2013, Braingate used invasive neural interfaces to control the robotic arm [13]. In 2016, American entrepreneur Elon Musk purchased Neuralink to develop high-bandwidth neural interfaces [14]. In 2017, the US Defense Advanced Research Projects Agency (DARPA) and Facebook launched separate neural interface projects [15, 16].

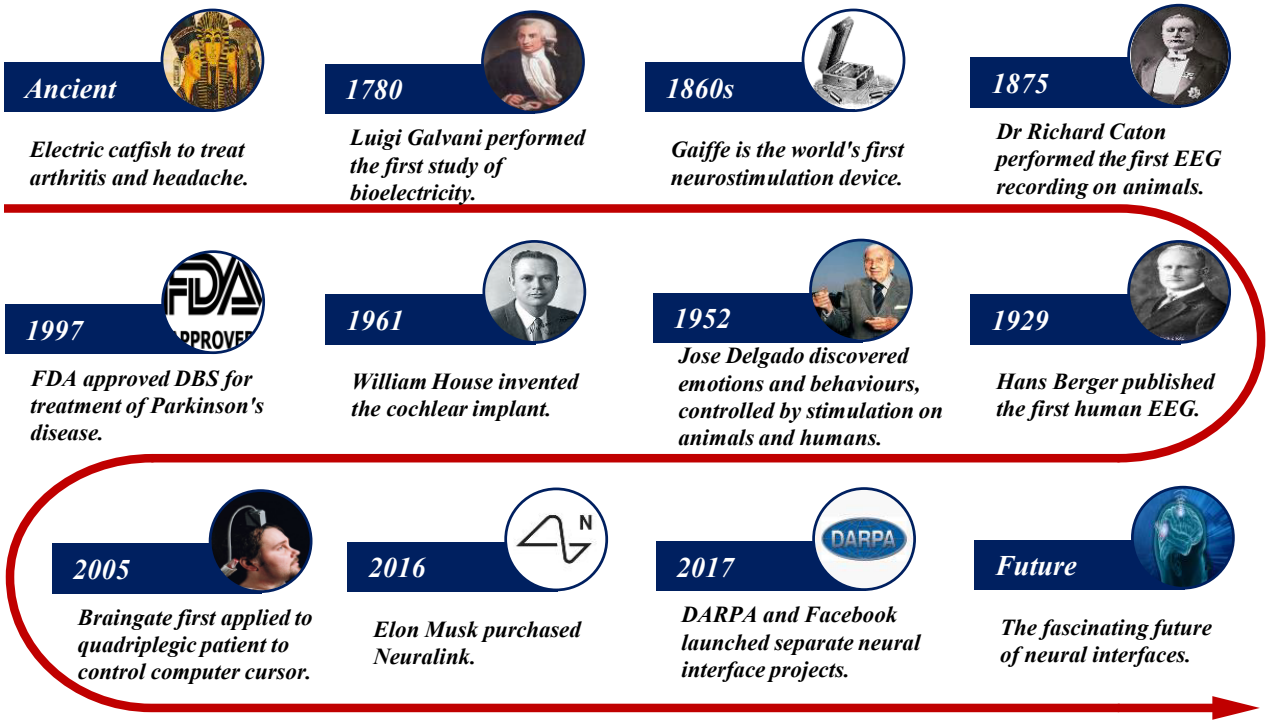


Figure 1.1: Neural interface development timeline.

1.1 Motivation

Brain-computer interfaces have experienced rapid development, specifically over the past 20 years. Neuroscientists have successfully recorded the action potentials of cortical neurons to explain the process of intracellular electrical signalling transmission and intercellular electrochemical transduction mechanisms. Recent experiments have involved recording a small fraction of nerve cells in a matter of hours. Currently, investigators are successfully recording hundreds of nerve cells for periods of weeks, months, or even years, with well-developed bio-compatible devices. Technical progress has now allowed us to experiment on rodents and primates. At hand, investigators have begun to bring neural interfaces into treatment for human neurological diseases. For example, the most successful neural interface applications today are cochlear implants for congenital deafness and DBS for Parkinson disease. Recent trends in the development of neural interfaces focus on the recorded channel increments and volume minimisation.

With regard to recording neural signals, there are three different methods for implementing neural interfaces - these vary according to the degree of invasion and the spatial resolution of the neural signals. They are *non-invasive*, *partly invasive* and *invasive*. Examples of these three neural interfaces are shown in Figure 1.2.

A completely *non-invasive* EEG records superimposed regional neural signals and is considered the safest way to record brain activity since sensors are simply placed on the scalp. However, a key limitation is that EEG suffers from low spatial and frequency resolution (approximately 10 mm at 100 Hz) [17] due to the acquisition position being approximately 2 cm away from the neurons. The biological tissues composed of the skull and skin act as a low-pass filter to reduce the signal intensity to approximately 10 μV. This limitation is inherent to non-invasive brain-computer interfaces and cannot be overcome in theory or practice.

To overcome superposition of regional neural signals, *partly-invasive* methods have been proposed for electrocorticography (ECoG), whereby sensors are embedded on the dura mater and pia mater. Due to its comparably higher resolution and frequency content than EEG-based BMI, ECoG-based BMI provides higher accuracy in the readings. It can also produce finer

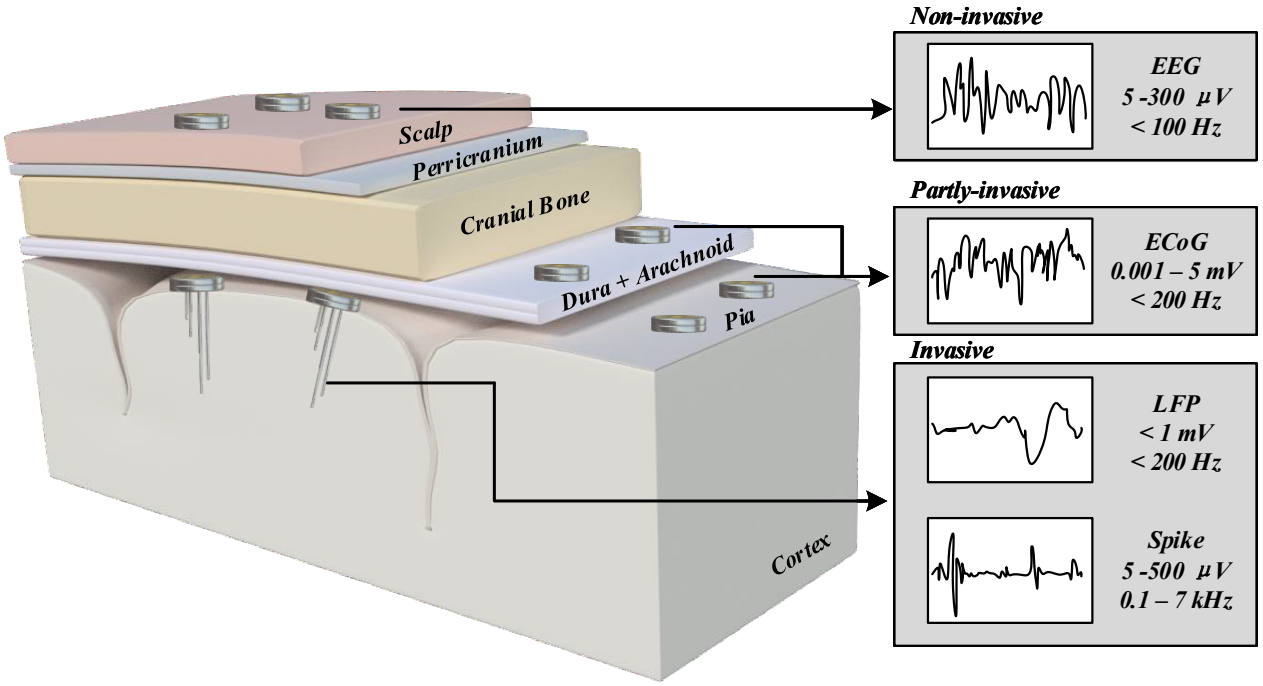


Figure 1.2: Various types of neural interfaces from non-invasive to invasive.

spatial resolution (millimetre level) and record higher frequency neural signals (10-200 Hz) [17]. Thus, ECoG has been widely used in the study of epilepsy in humans. To obtain the highest resolution neural signals to control prostheses, invasive intracortical electrodes achieve excellent spatial resolution (sub-millilitre) [18] and high frequency resolution (up to kHz) [17].

The *invasive* brain-computer interface provides high-quality neural activity signals, but with limited coverage area while requiring time-consuming surgical interventions. Regulatory approval of invasive brain-computer interfaces is more stringent than that of non-invasive interfaces as these are embedded in patients and scientific research subjects for a longer period of time. This stringent regulation criterion arises mainly from medical problems that could be associated with neurosurgery and implants. In comparison, the most prominent advantage of non-invasive brain-computer interfaces is the ability to monitor large-scale neural activity at low cost and almost zero risk. Hence, most common commercial brain machine interfaces are now non-invasive [19], such as Dreem, Thync, BrainCo, Bitbrain Technologies and so on.

1.1.1 Why Invasive?

For research purposes, invasive neural interfaces can provide more detailed and accurate neural activity data than non-invasive neural interfaces. Therefore, my work focuses on exploring the future potential development of invasive neural interfaces from technical perspectives. Three apparent benefits of invasive neural interfaces are summarised as follows.

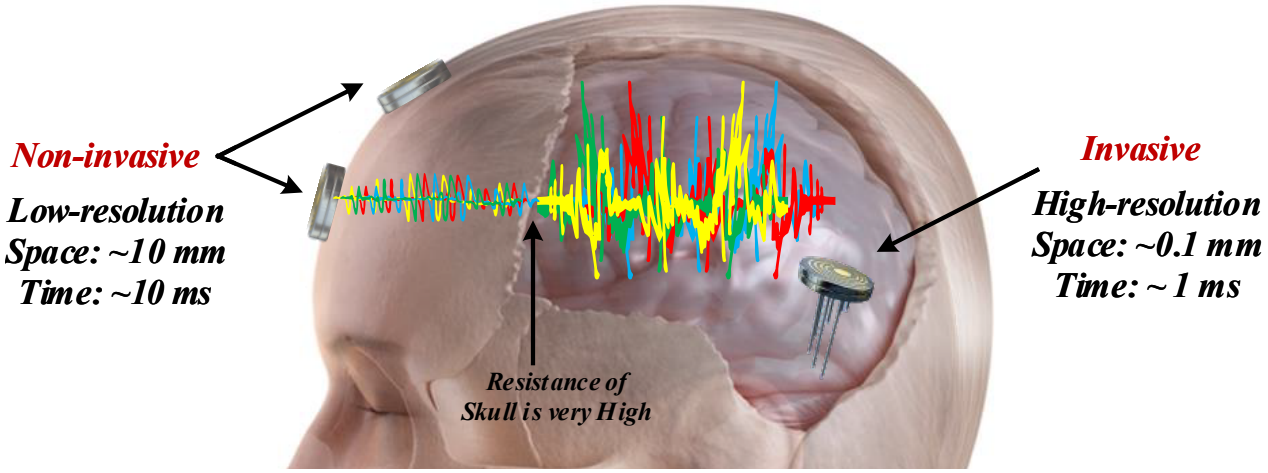


Figure 1.3: Comparison between non-invasive and invasive neural interfaces.

(1) High Spatial Resolution: The invasive neural interface can detect neural activities at specific locations, but the non-invasive neural interface can detect only regional neural activity. Since electric fields generated by neurons decay exponentially with distance, the non-invasive neural interface at a long distance is limited to detect superposed electric fields that are composed of a large number of neurons in the cortex. Non-invasive neural signals in the region are extracted from the EEG by completely removing the noise of the muscles and the eye motion. In contrast, invasive neural interfaces can directly detect intracellular potentials, extracellular action potentials (APs), and local field potentials (LFPs) via implanted electrodes.

(2) Wide Signal Bandwidth: Invasive neural interfaces detect neural signal frequencies from Hz to KHz, while non-invasive neural interfaces can detect only neural activity of less than 90 Hz. Only because the body tissue acts as a low-pass filter, it usually attenuates the higher-frequency signals and hides them in the background noise.

(3) Low Spatial Distortion: The invasive neural interface can detect neural signals that are less distorted during transmission. The extracellular space consists of media with different electrophysiological properties that affect the propagation of the field before being detected as LFPs. In addition, the electric field diffuses in the cerebrospinal fluid, skull, and scalp, causing further spatial distortion before reaching the EEG electrodes. Complex head models and algorithms, combined with high-density EEG masks, mitigate the distortion of signals above a certain noise level [20]. However, invasive nerve implants can directly acquire nerve signals with less spatial distortion through the electrodes.

1.1.2 Why Wireless?

Blackrock Microsystems platform (previously BrainGate) [12, 13] uses multielectrode arrays and skull-mounted connectors to collect neural signals and transmit them through delicate wire bundles, as shown in Figure 1.4(a). Amplification and recording electronics are then done outside the human body. This wired scheme has four inevitable obstacles to neural signal acquisition:

(1) Wired Connections: Percutaneous wires are likely to cause inflammation or infection of biological tissues.

(2) Noise Interference: External noise and interference signals are easily coupled to weak neural signals transmitted on wire bundles.

(3) Biological Failure: Skull-mounted connector and anchored array are undesirable. They may cause biomaterial-induced foreign body response or neural damage, which limit long term stability of neural implants.

(4) Device Failure: Packaging failure, electrode breakage or implants' damage during the implantation procedure are likely to result in devices failures.

To eliminate these problems, data from electrodes should be amplified, digitised at the recording site and then transmitted wirelessly outside the human body. In the 1990s, wireless neural

recording systems were constructed from discrete commercial components [21]. Current wireless systems have utilised integrated circuits for both signal amplification and power rectification [22,23]. Therefore, it is essential to apply microelectronic systems at recording sites to amplify, condition, and digitise neural signals. Ideally, the implanted microelectronic systems should supply power and exchange data wirelessly, as shown in Figure 1.4(b).

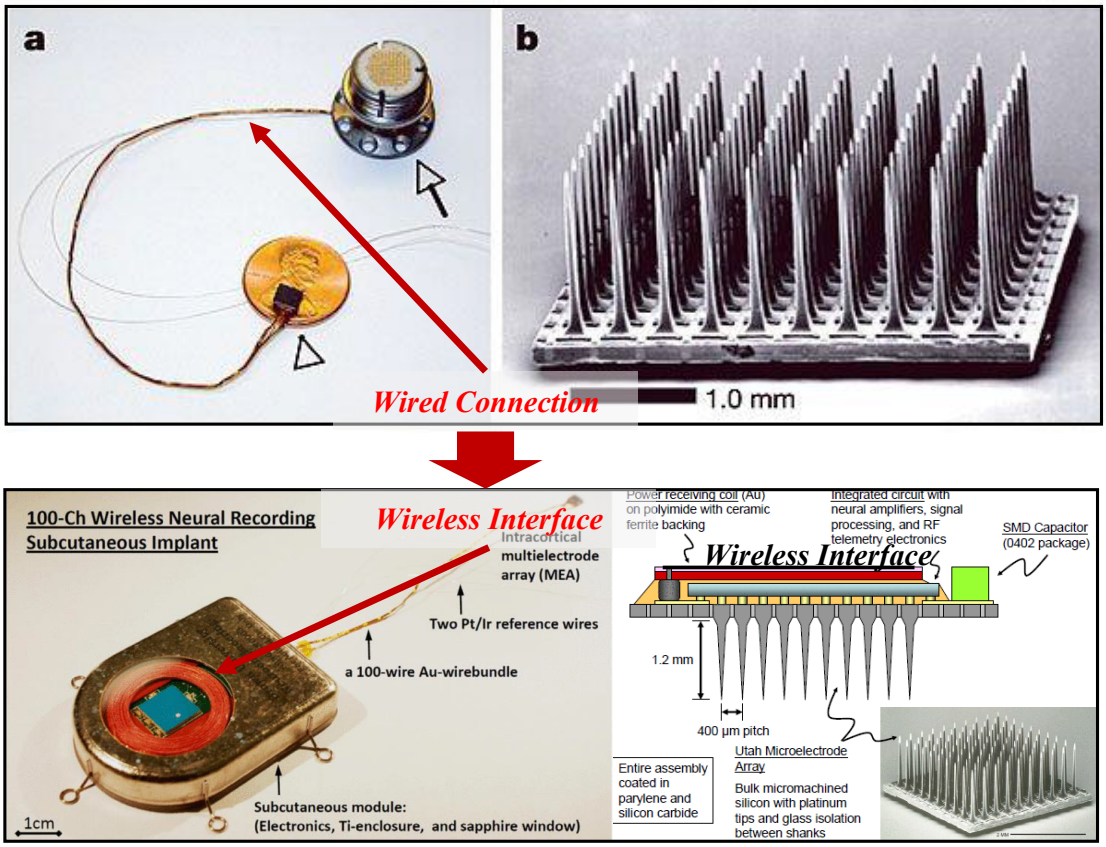


Figure 1.4: Current development of multielectrode arrays from wired connections to wireless interfaces.

1.2 Technical Challenges

The general purpose of invasive neural interfaces is to keep extracting the required neural signals without disturbing normal neuron activities during the maximum life expectancy of the subjects. Therefore, we analyse the existing technical challenges of neural implants from the following three aspects: chronic stability, scalability, and wireless capability.

1.2.1 Chronic Stability

Neural implants require reliable biocompatible packaging while minimising damage to neurons and biological tissues to extend the lifetime of these medical devices. The typical failure modes are summarised from biological, material, and mechanical perspectives [24]. Biological failure involves the symptoms caused by implant surgery, such as bleeding, cell death, inflammation, scar growth, gliosis and other clinical conditions. Material failures are frequently caused by packaging failure and electrode breakage. Mechanical failures relate to the implants' damage during the implantation procedure, or implants accidentally pulling out due to brain micro-movements or dural stitches.

1.2.2 Scalability

The brain has distributed information processing, and thus the locations for monitoring the neural activities must be discretely distributed over the cerebral cortex. In this case, the desired number of recording channels should exceed thousands, which could provide the possibility for accurate analysis and understanding of neural signals. Thus, scalable neural implants development is a balance between having sufficient data communication, channel calibration, and energy dissipation at the cost of device volume to achieve optimal spatiotemporal resolution.

1.2.3 Wireless Capability

As mentioned in subsection 1.1.2, the wireless solution for implants avoids transcutaneous wire bundles and bulky connectors. The existing challenge is how to achieve efficient wireless power transfer through biological tissues while establishing robust data communication.

1.2.4 Summary

Based on the above statement, the vision of the next generation neural interface are summarised as the following three points.

(1) Wireless Connection: Neural interfaces require a fully complete wireless interface that is able to deliver sufficient power to multiple implants as well as transmit large amounts of recording data back to the external device.

(2) Miniaturised Volume: The second one is the miniaturisation of the dimensions of implantable medical devices, which may shrink from a single centimetre-sized device to multiple millimetre-sized devices and even sub-millimetre-sized.

(3) Distributed System: The last point is to develop scalable, distributed, free-floating implantable devices instead of centralised, tethered designs.

All these technological challenges inspire researchers to develop the next generation of neural interfaces. Hopefully, these implantable medical devices will help disabled patients to improve the quality of their life and provide powerful tools for neuroscientists to explore the human brain. The last challenges are the foremost motivations of this work. The remainder of this thesis will investigate the wireless capability of neural interfaces and then propose feasible solutions.

1.3 Research Objectives

The principal objective of this work is to establish efficient wireless power transfer and robust data communication for distributed mm-scale neural implants. Three research questions and technical issues will be addressed in this thesis.

Objective 1: How to design CMOS compatible electromagnetic energy harvesters for mm-scale implantable medical devices? What is the maximum power transfer efficiency of resonant inductive links for different types of receivers? How much power can be received from mm-scale coils in distributed wireless networks within the safety level? To solve these questions, geometrical optimisation of inductive links will trade-off between the quality characteristic, operating frequency, and load resistance to achieve the optimal power transfer efficiency.

Objective 2: How can we extend the power coverage for multiple distributed receivers? How can each implantable micro-system autonomously harvest sufficient power through biological tissues? We should investigate mm-scale distributed wireless inductive networks between multiple coupled coils for powering implantable neural micro-systems and explore an autonomous power harvesting architecture for the distributed neural interfaces. An innovative on-chip power harvesting approach will be developed to ensure that each of the freely positioned implants receives adequate power and supply stable voltage regardless of their location and orientation.

Objective 3: How can data be transmitted from multiple sensor nodes by using mutually coupled networks? How can interference between the power carrier and the data modulation be reduced by employing the single receiving device? We should develop distributed transcutaneous data links formed by multiple independent sources with near-field coupling to a receiver outside the body.

1.4 Thesis Outline

Chapter 2 reviews the typical wireless power and data transfer techniques for implantable medical devices to reveal the existing technological challenges and indicate the trends of current research. This chapter can be summarised as the following technical details.

- Comparison between different wireless power transfer techniques;
- Theoretical model of inductive links for power transfer efficiency analysis;
- Comparison between passive and active data telemetry.

Chapter 3 thoroughly compares mm-scale Rx coils from the perspective of analytical modelling, simulation, fabrication, and measurement. Then, the specific Rx coil type is selected for CMOS integration and implantable micro-systems based on their manufacturability, hermeticity, mechanical stability and electrical properties. The technical details of this chapter are as follows.

- Measurement verified electromagnetic analytical and simulation models of three different types of Rx coils;
- Power transfer efficiency comparison of conventional 2-coil link with different types of Rx coils in biological environments.

Chapter 4 proposes multiple resonant arrays with enhanced wireless power transfer for boosting the received voltage and extending the power coverage for multiple implantable devices against the Tx-Rx angular and positional misalignment. The two aspects in this chapter are summarised as below.

- EM-Lens enhanced wireless power transfer prototype experimental verification;
- Auto-tune self-regulated power management with theoretical analysis and measured results.

Chapter 5 presents a novel wireless multiple-node data communication scheme for distributed implantable medical devices. Two technical points of this chapter are listed as below.

- Backscatter modulation and code division multiple access technique that address the simultaneous multiple nodes data communication;
- Develop wireless powered data senders based on discrete devices and receiver platform that enables real-time data decoding.

Chapter 6 summarises the original achievements by considering how the proposed wireless infrastructure can be technically improved from power transfer efficiency and data rates. Reflecting on the proposed system we conclude the further effort to approach hermetic application integration.

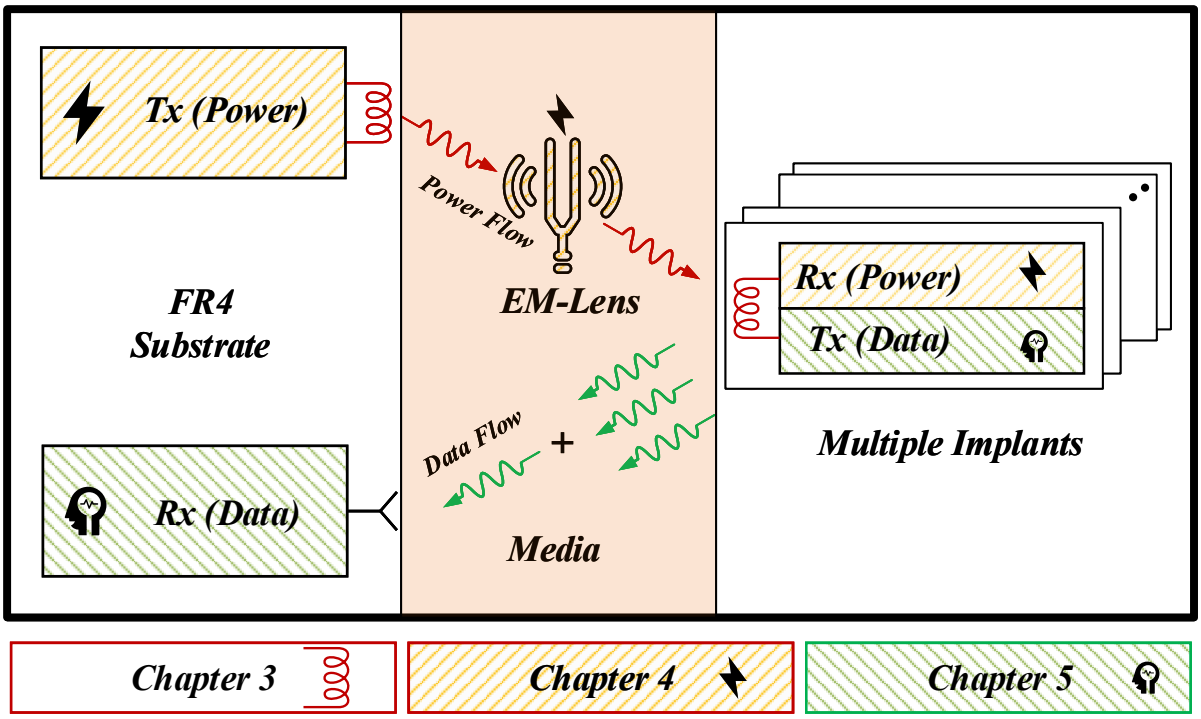


Figure 1.5: Thesis structure is displayed into wireless information and power transmission system.

Chapter 2

Literature Review

"Nothing is too wonderful to be true, if it be consistent with the laws of nature; and in such things as these, experiment is the best test of such consistency."

– Michael Faraday, 1791 - 1867

This chapter firstly reviews the history of wireless power transmission and data communication, then summarises the existing challenges and forthcoming trends of wireless technologies in implantable medical devices based on the recent researches and experiments.

2.1 Historical Review of EM Transmission

The development of electromagnetic (EM) fields and waves has three crucial historical stages: theory establishment, scientific experiment, and practical application. A remarkable milestone of EM theory was achieved in 1861, when James Clerk Maxwell published his world-famous equations based on Faraday's experimental results and predicted the transmission of electrical and magnetic fields in the vacuum. In 1887, Heinrich Hertz first confirmed the existence of EM

A portion of this chapter has been rewritten as the last section of book-chapter in Handbook of Neuroengineering [25]. This book chapter is currently under review.

waves through his ingenious half-wavelength dipole antenna. Since then, classical EM theory has been established by Maxwell and Hertz.

During the second phase, EM theory was applied to wireless power transmission and wireless data communication independently. A well-known figure in the field of wireless power transmission is Nikola Tesla. From 1899 to 1910, he proposed the world-famous Warden Clifford for transatlantic radio and power transmission experiments; although this project was eventually suspended due to lack of funds, he received high media attention. His aura and unfulfilled goals continue to the point where they still exit today, and his dramatic sci-fiction story triggered my interest in this field. Almost at the same time, Guglielmo Marconi completed the golden era of wireless data communications, opened by transatlantic radio transmission experiments. Since then, the research development of wireless data communication is far faster than wireless power transmission.

The third phase is the military and commercial applications. During World War Two, the applications of wireless communication technology were quickly applied for military purposes, then transferred into people's daily telecommunications such as broadcasting, cellular networks, radio navigation-satellite services, wireless sensing networks, and short-distance point-to-point communications. However, the applications of wireless power transmission are still limited. Typical applications include wireless charging for consumer electronics (such as toothbrush, mobile phone, and so on.), radio-frequency identification (RFID), and electric vehicle wireless chargers. The most successful wireless power transfer applications are in implantable medical devices, such as cardiac pacemakers, and cochlear implants. Wireless power transfer is used in cardiac pacemakers to avoid the inconvenience of battery replacement. The application of wireless power transmission to cochlear implants also avoids the presence of transcutaneous wired connections.

2.2 Wireless Power Transfer

As shown in Figure 2.1, typical wireless power transfer techniques for implantable medical devices include ultrasonic, electromagnetic, and optical power transmission, and recently emerging thermal, biochemical, and kinetic energy harvesting. For neural interfaces, ultrasonic power transmission is being considered for the peripheral nervous system because ultrasonic waves cannot effectively penetrate high-density biological tissues, in particular the spine and skull. Electromagnetic power transmission is widely adopted in peripheral and central nervous system implants. Because the magnetic permeability variations in biological tissues are negligible, they result in effective magnetic penetration inside the body. The current development of wireless transmission systems usually focuses on power transfer efficiency enhancement under stringent safety and health regulations [26, 27] with respect to body tissue exposure to different energy radiation. Other emerging biological energy harvesting methods utilise temperature variations, biochemical (glucose [28] or ATP [29]) energy, or kinetic energy, but the power density varies from 12.6 $\mu W/mm^2$ to 61.25 $\mu W/mm^2$ [30–33], which is not sufficient to achieve the minimum power budget ($\sim$ 100 $\mu W/mm^2$) of microelectronic systems. In the following subsections, we first review various wireless power transmission methods and subsequently compare them to guide the selection of implantable medical devices.

2.2.1 Electromagnetic Power Transfer

Electromagnetic power transfer is a prevalent method of WPT. It can be divided into three regions: near-field, mid-field, and far-field, according to the wavelength relative to the transmitter-receiver distance. The boundary of mid-field region is not strictly defined. If consider the electromagnetic waves, the near-field waves is complicated and unpredictable, while the far-field EW is considered as uniform. The near-field and far-field can be specified by Fraunhofer distance [35], which is defined as

$$d_f = 2d_o^2/\lambda \tag{2.1}$$

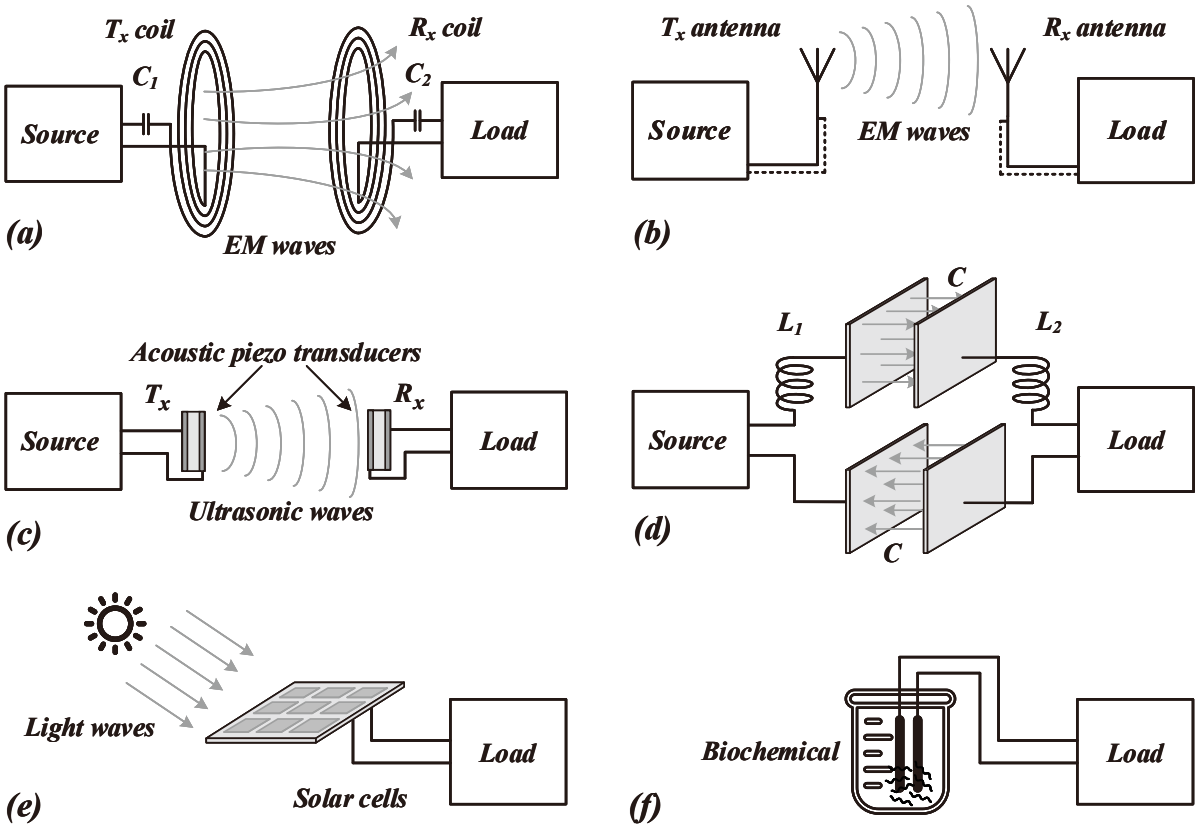


Figure 2.1: Typical wireless power transfer techniques for implantable medical devices [34]: (a) electromagnetic inductive coupling; (b) electromagnetic radiation or beamforming; (c) ultrasonic waves; (d) capacitive coupling; (e) Solar energy harvesting; (f) biochemical energy harvesting.

where d_f is the boundary between near-field and far-field. d_o is the outer diameter of coils and λ is the EM wavelength in the transmission medium.

The near-field and mid-field regions are widely applied for wireless power transmission in implantable medical devices, such as providing continuous power to cochlear implants, or recharging implanted batteries in DBS systems, while far-field power transmission is limited to extreme low power transfer efficiency (PTE) over long distances, due to massive loss in GHz operating range [36]. Most importantly, the far-field power transmission is not suitable for implantable medical devices because the safety requirements regarding the electromagnetic radiation to the human body limit the incident RF energy level. Researchers [37] suggested moving the operating electromagnetic frequency from kHz to tens of MHz for powering implantable medical devices in the near-field region. Although electromagnetic radiation is negligible for biological

tissue at such low frequencies, the relatively long quarter wavelength (5.6 m at 10 MHz in water) prevents the miniaturisation of implantable medical devices, which results in the achieved minimum Rx diameter at the order of centimetres. Recently, the operating frequency has moved to hundreds of MHz, which leads to the diameter reduction of the implanted Rx and PTE improvement [38]. Furthermore, the transmission of mid-field electromagnetic transmission has recently been proposed by [39], and the operating frequencies increase up to GHz. This approach has the convenience of further miniaturisation of implanted devices, but electromagnetic radiation with respect to biological tissue requires special attention.

Three key parameters of electromagnetic power transfer are the transmitter-receiver (Tx - Rx) distance d_{Tx-Rx}, the diameter of receiver D_{Rx}, and the operating frequency f. The Tx - Rx distance d_{Tx-Rx} is determined by the implantation position. For the human central nervous system, the brain-scalp distance varies with age and region of skull from 7 mm to 20 mm, and a typical value is 12 mm [40]. The Rx Diameter D_{Rx} must comply with the miniaturisation trend of the implanted devices since their volume is crucial for the patients' safety. Millimetre-scale or sub-millimetre-scale devices reduce the surgical risks, such as inflammation and foreign body reactions. Currently, advanced microelectronic fabrication technology can undoubtedly meet the requirements of implants due to the evolution of Moore's Law. In addition, recent progress in microfabrication has reduced its mechanical structure remarkably, such as in microelectrode arrays. However, the Rx devices' miniaturisation is against the power transfer efficiency enhancement.

The crucial parameter that must be optimised is the operating frequency f of the electromagnetic waves. Depending on the operating frequencies, there are different employed techniques: inductive coupling (near-field), EM radiation (mid-field), and beamforming (far-field), as shown in Table 2.1. Inductive coupling usually operates from kHz to hundreds of MHz. It features high power transfer efficiency within a short distance (millimetres to a few centimetres). In addition, it is important to guarantee the precise Tx/Rx coil alignment. The transfer distance is increased from 4 to 10 times the diameter of the coil by implementing magnetic resonant coupling with tuned coils or lumped element resonators. EM radiation employs segmented antennas to achieve mid-distance transmission (up to several centimetres) in the sub-GHz to the

tens of GHz frequency range. The drawback of this solution is the low power transfer efficiency and troubling safety and health risks. In the GHz to THz frequency range, the beamforming scheme achieves a high energy concentration and low interference with existing communication systems, but its extremely high EM radiation is hazardous, thus it is not suitable for medical or consumer electronics products.

Table 2.1: Comparison of various electromagnetic power transfer methods.

EM Region	Technology	Frequency	Range	Benefit	Drawback
Near-field	Inductive coupling	kHz to MHz	Millimetres to centimetres	High efficiency	Short distance
Mid-field	EM radiation	Sub-GHz to GHz	Centimetres to metres	Small receiver	Low efficiency
Far-field	Beamforming	GHz to THz	Up to kilometres	Long range	Health hazard

Therefore, inductive coupling is the most suitable technology for implantable medical devices in the electromagnetic power transmission region. The following subsections will reveal the existing challenges and present the future directions of inductive coupling. A conventional 2-coil inductive link is taken as an example, where we briefly describe its operating principles and coupled-mode theory in resonance-based WPT.

A. Operating Principle of Inductive Link

Fig 2.2 shows a simplified 2-coil inductive link. It consists of an external transmitter on the primary side and single implanted receiver at the secondary side. The external transmitter is connected to the battery or the power supply and converts electrical power into electromagnetic fields. These fields transmit through the biological tissue, then are coupled to multiple receivers. The Rx coil at the secondary side converts the sensed electromagnetic fields into AC electrical energy. After power rectification and regulation, the stable DC voltage supplies the implantable microelectronic system. The external circuitry on the primary side includes a power amplifier for power transmitting, and data modulation/demodulation for downlink and uplink. Implanted circuitry on the secondary side usually contains the active or passive rectifier, low-dropout regulator (LDO), and data transceiver.

The power transmission efficiency of the entire system consists of the power-added efficiency (PAE) of the power amplifier, AC - DC power conversion efficiency (PCE $_{\text{AC-DC}}$) of the rectifier,

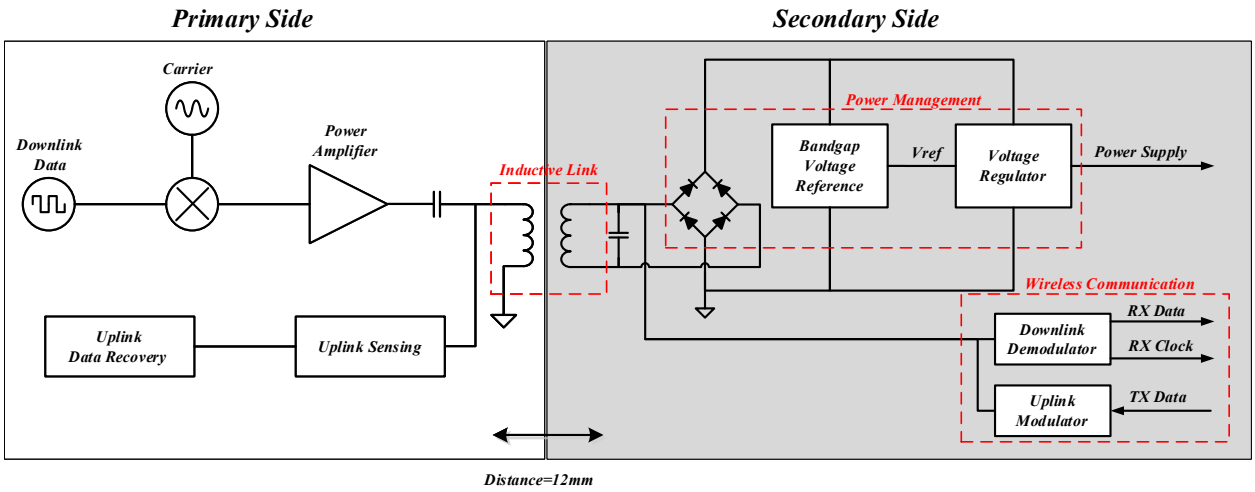


Figure 2.2: Block diagram of conventional 2-coil inductive link

DC - DC power conversion efficiency (PCE $_{\text{DC-DC}}$) of the regulator, and power transfer efficiency (PTE) of the inductive link, as shown in Figure 2.3. A class-E power amplifier and on-chip power conditioning (rectification and regulation) are likely to achieve high power conversion efficiency. However, the inductive link is the weakest part of the overall energy transfer flow [41]. Since the Tx and Rx are in a weak coupling condition, a large portion of the incident electromagnetic energy is absorbed or reflected by biological barriers. Thus, the PTE of a 2-coil link for brain-machine interfaces is usually less than 10%, even though several advanced techniques have been proposed, such as, tissue absorption reduction by optimising the operating frequency [38], special patterns of the transmitting EM field generation [42] or coil resistance reduction by optimising the geometrical dimensions of the inductive link [43].

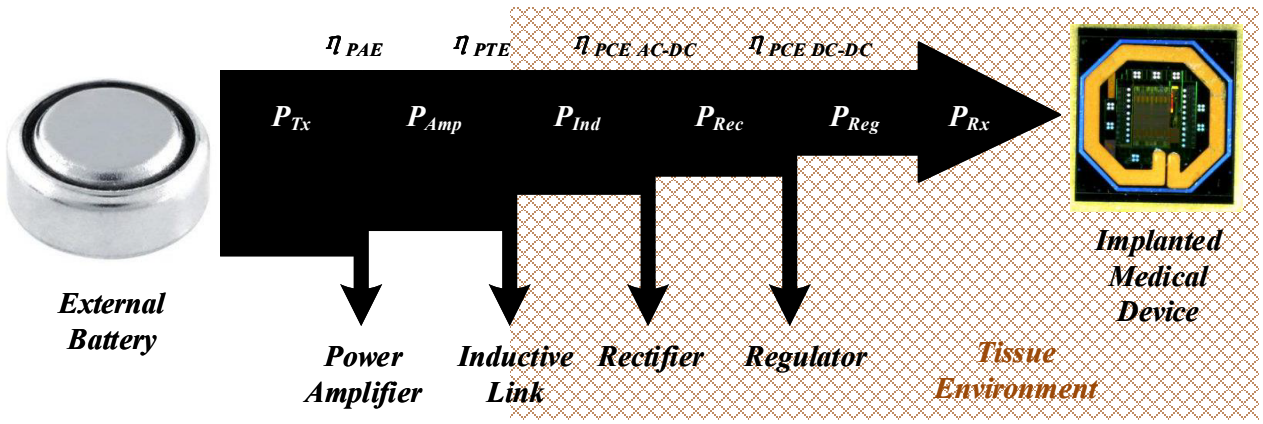


Figure 2.3: Power transfer efficiency of entire inductive coupled power transmission system redrawn from [41].

B. Inductive Link Theory

The inductive link is the key component in the entire wireless power transmission system. Optimisation of the wireless links is a vital step towards achieving the maximum PTE. The PTE of a 2-coil inductive link can be derived from a reflected load model [44, 45] or two-port network model [38, 46].

B1. Reflected Load Model

The reflected load model is based on resonant inductive coupling. The resonant frequency is usually defined as

$$\omega = 2\pi f = \frac{1}{\sqrt{L_1 C_1}} = \frac{1}{\sqrt{L_2 C_2}}. \tag{2.2}$$

The reflected load theory assumes that all inductance and capacitance cancel each other under the resonant conditions. The equivalent model is simplified as a resistor divider to evaluate the power transfer efficiency effectively and a simplification process of the inductive link presented in Figure 2.4(a). The Q factors of each inductor L_1, L_2, and load resistance R_L are expressed as

$$Q_1 = \frac{\omega L_1}{R_1}, \tag{2.3}$$

$$Q_2 = \frac{\omega L_2}{R_2}, \tag{2.4}$$

$$Q_L = \frac{R_L}{\omega L_2}. \tag{2.5}$$

The loaded Q factor of secondary inductor L_2 is defined as

$$Q_{2L} = \frac{Q_2 Q_L}{Q_2 + Q_L}. \tag{2.6}$$

After bringing the secondary LC tank with load resistance to the primary side as parallel reflected RLC components, L_1, C_1 and L_{ref}, C_{ref} cancel out due to the resonant conditions and

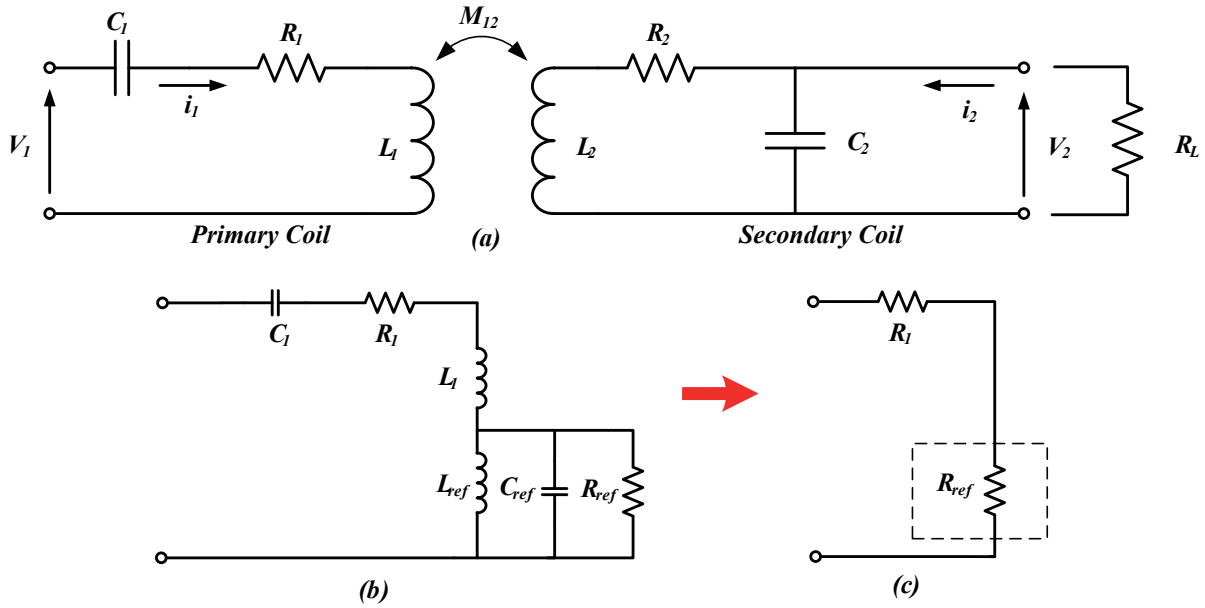


Figure 2.4: Reflected load model redrawn from [45] (a) Simplified 2-coil inductive link; (b) Equivalent circuit with reflected load from secondary side; (c) Resistive divider of 2-coil inductive link.

the remaining resistors R_1 and R_{ref} form a resistive divider. The reflected resistor R_{ref} can be written as

$$R_{ref} = k_{12}^2 \omega L_1 Q_{2L}. \tag{2.7}$$

Consequently, the power transfer efficiency is expressed as [44, 45, 47]

$$\eta = \frac{k_{12}^2 Q_1 Q_{2L}}{1 + k_{12}^2 Q_1 Q_{2L}} \frac{Q_2}{Q_2 + Q_L}. \tag{2.8}$$

According to the above equation, the coupling coefficient k_{12} is the dominant factor since PTE is proportional to the square of k_{12} , where k_{12} is defined as

$$k = \frac{M_{12}}{\sqrt{L_1 L_2}}. \tag{2.9}$$

When all equations (2.2-2.6, 2.9) are substituted into the PTE equation 2.8, we find that η is independent of the inductance of the primary coil L_1.

$$\eta = \frac{M_{12}^2 \omega^4 L_2 R_L}{R_1(\omega^2 L_2^2 + R_2 R_L)^2 + M_{12}^2 \omega^2 R_L(\omega^2 L_2^2 + R_2 R_L)} \tag{2.10}$$

In addition, the optimal load resistance R_L derived from equation (2.8) can be expressed as

$$R_L = \frac{\omega L_2 Q_2}{\sqrt{1 + k_{12}^2 Q_1 Q_2}}. \tag{2.11}$$

B2. Two-Port Network Model

The inductive link is usually considered to be a two-port network, as shown in Figure 2.5 (a). The scattering matrix (S-parameters) of this two-port network can be simulated in the EM field solver or measured by a vector network analyser (VNA). The S-parameters represent the ratio of the incident voltage and the reflected voltage on the ports. However, the Z-parameters, which depict complex ratio of the voltage and current in AC circuits, are the key to analysing the power transfer efficiency of the system. The conversion from the S-parameters to the Z-parameters of a two-port network can be performed by means of the following expressions[1]. The relationship between the input and output voltage (V_1, V_2) and the current (i_1, i_2) are described as an impedance matrix [Z]. We assume that this impedance matrix is symmetric ($Z_{12} = Z_{21}$) since there are no active devices.

$$\begin{bmatrix} \mathrm{V}_1(s) \\ \mathrm{V}_2(s) \end{bmatrix} = \begin{bmatrix} Z_{11} & Z_{12} \\ Z_{21} & Z_{22} \end{bmatrix} \begin{bmatrix} i_1(s) \\ i_2(s) \end{bmatrix} = \begin{bmatrix} R_1 + L_1 s & M_{12} s \\ M_{12} s & R_2 + L_2 s \end{bmatrix} \begin{bmatrix} i_1(s) \\ i_2(s) \end{bmatrix} \tag{2.12}$$

This two-port Z-network can be simplified into a T equivalent circuit (as shown in Figure 2.5 (b)), and then, PTE is derived based on this impedance network, similar to the previous reflected load model [46].

[1]The characteristic impedance Z_0=50 Ω, since the standard impedance of the VNA ports is 50 Ω. [48]

$$\begin{aligned}
Z_{11} &= Z_0 \tfrac{(1+S_{11})(1-S_{22})+S_{12}S_{21}}{(1-S_{11})(1-S_{22})-S_{12}S_{21}}; \\
Z_{12} &= Z_0 \tfrac{2S_{12}}{(1-S_{11})(1-S_{22})-S_{12}S_{21}}; \\
Z_{21} &= Z_0 \tfrac{2S_{21}}{(1-S_{11})(1-S_{22})-S_{12}S_{21}}; \\
Z_{22} &= Z_0 \tfrac{(1-S_{11})(1+S_{22})+S_{12}S_{21}}{(1-S_{11})(1-S_{22})-S_{12}S_{21}};
\end{aligned}$$

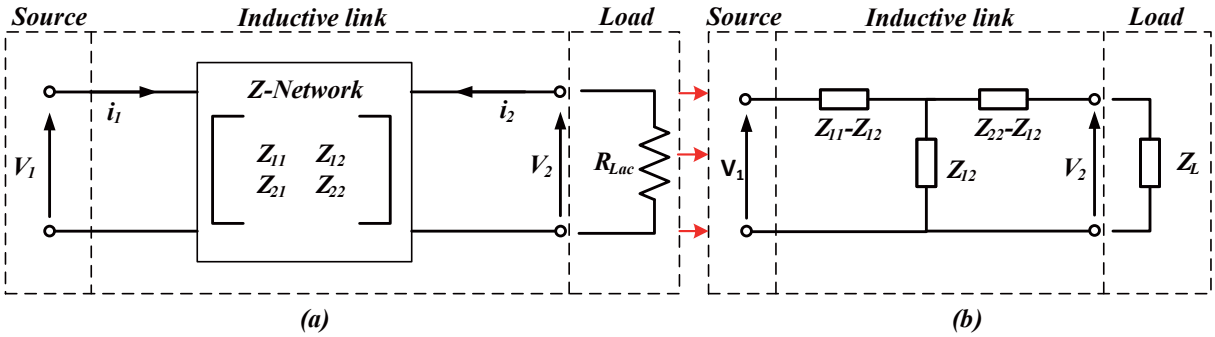


Figure 2.5: Two-port network model redrawn from [49] (a) Simplified Z-network of 2-coil inductive link; (b) Equivalent circuit with Z parameters.

$$\eta = \frac{\mathrm{Re}(Z_L)}{\mathrm{Re}(Z_{in})}\left(\frac{|Z_{21}|}{|Z_{22}+Z_L|}\right)^2 \approx \frac{\mathrm{Re}(Z_L)}{\mathrm{Re}(Z_{11})}\left(\frac{|Z_{21}|}{|Z_{22}+Z_L|}\right)^2, \tag{2.13}$$

where $Z_{in} = Z_{11} - Z_{12}Z_{21}/(Z_{22}+Z_L) \approx Z_{11}$ due to having a weak coupling factor between the primary and secondary coils (< 0.01) [38]. This impedance-based equation contains resistors, inductors, and capacitors, and is treated as an accurate PTE calculation method in simulation and in measurements under weak coupling conditions. Thus, this equation can be further simplified as [38]

$$\eta = \frac{|Z_{21}|^2}{|\mathrm{Im}(Z_{11})\mathrm{Im}(Z_{22})|}\frac{|\mathrm{Im}(Z_{11})|}{R_{11}}\frac{|\mathrm{Im}(Z_{22})|}{(R_{22}+R_L)}\frac{R_L}{(R_{22}+R_L)} = k^2 Q_{Tx} Q_L \eta_{Rx}. \tag{2.14}$$

B3. Comparison

The PTE (η) expression 2.10 in the reflected load model and expression 2.14 in the two-port network model are basically the same. The expressions 2.10 in the reflected load model can be derived from the Z-parameters 2.12 by substituting into 2.14. The major difference between these two models is caused by their assumptions.

The assumption of the reflected load model is the same resonant frequency on both the primary and secondary sides to allow all imaginary parts of the impedance to be cancelled out. With the aid of this model, designers intuitively analyse the relationship between the PTE and Q factor/coupling strength k_{12}. However, this relationship will inevitably lead to an optimistic estimation of the PTE, since the assumptions cannot be fully met due to the ideal resonant

conditions of the entire system. Thus, the reflected load model gives the theoretical maximum upper limit of the PTE in 2-coil inductive links.

The assumption of the two-port network model is the weak coupling factor k_{12} between the primary and secondary coil such that the input impedance Z_{in} depends mainly on the primary coil. This two-port network model is suitable for predicting the actual PTE based on the measured S-parameters. The PTE expressions from both models provide a theoretical background for identifying key parameters (k_{12}, ω, Q_2) in the inductive link. In addition, these equations provide the foundation for the geometric optimisation of inductive links.

C. Recent Trends in Electromagnetic Power Transfer

Several years ago, the major effort in wireless power transmission for implantable medical devices focused mainly on PTE improvement, while satisfying the corresponding specific absorption rate (SAR) requirements for biological tissue, regardless of the power coverage extension for distributed implants [38, 50, 51]. The most prevalent approach of the PTE optimisation focuses on the selection of key geometric dimensions of the receiver and transmitter, such as the number of turns and trace width/spacing ratio [52, 53]. Different iterative algorithms [38] and theoretical models [41, 54] have been proposed to perform PTE optimisation based on coil geometry.

Recently, distributed neural interfaces require extensive uniform power coverage to provide continuous energy to multiple free-positioned implants. A conventional 2-coil inductive coupled link is no longer able to meet the power coverage requirement. In addition, 2-coil links suffer from low power transfer efficiency due to the weak coupling coefficiency and centrally focused power coverage because of non-uniform electromagnetic fields generated by a single transceiver [38]. A well designed 2-coil link is the encapsulated neural interfacing acquisition chip (ENIAC) from the University of California San Diego [55], shown in Fig 2.6(a). The power and signal paths have been designed as a H-tree to avoid eddy current in the loop connections, to increase the Q factor of the Rx in-CMOS coil. The voltage gain in a 2-coil link is not sufficient to drive the micro-system at the secondary side, and thus, the multi-mode buck-boost resonant

regulating rectifier (B^2R^3) has been proposed to boost the rectified voltage. After implementing these advance techniques, the power transfer efficiency achieves 3.4% [55], but the scheme for powering distributed implants is not clear.

The 3-coil inductive link has been demonstrated to have higher PTE than the 2-coil link [56] and to extend the power coverage within a limited area. This scheme has been widely used in current distributed neural interfaces [57–63] to partly overcome the positional misalignment and to extend the power coverage. A single circular resonator is added between the transmitter and receivers to improve the PTE to 9.13% after following a complex iterative optimisation algorithm [60], as shown in Figure 2.6(b). Another example (Figure 2.6(c)) of a 3-coil architecture is Neurograins from Brown University, which is designed for a human [62] and rodent neural interface [63]. Different 4-quadrant coils are designed and fabricated according to the experimental objects. The 4-quadrant coil acts as a resonator in the 3-coil link to improve PTE. Also, it ensures that the magnetic field strengths in the two central symmetrical quadrants are consistent, which suppress differences of energy distribution at Rx side.

The intracortical visual prosthesis (ICVP) system in Figure 2.6(d) attempts the same coil for a wireless power supply and data transmission, and it also proposes the concept of a distributed system [64, 65]. In addition, the Yoon Lab [66] from the University of Michigan also proposed distributed wireless ECoG recording systems in Figure 2.6(e) . Each built-in intra-skin module has a rechargeable battery with a wireless inductive link, and thus, the problem of a concurrent wireless power supply for multiple modules has been avoided. In addition, there is a conceptual distributed scheme called scattered microbead [67] from Johns Hopkins University, as shown in Figure 2.6(f). Multiple transmitters supply power for sub-millimetre implantable wireless neural stimulator in different areas. Nevertheless, the power transfer efficiency deteriorates to 0.008%, and the power delivered to the load is less than 100 μW.

Some solutions to the uneven power coverage issue for distributed implants are inspired by the rodents' cage experiments [68], such as meshed overlapped transmitting coils to improve the distribution of the power density over a wide range. These also compensate for the robustness of the angular and positional offsets. Thus, it is worthwhile to note the wireless cage development

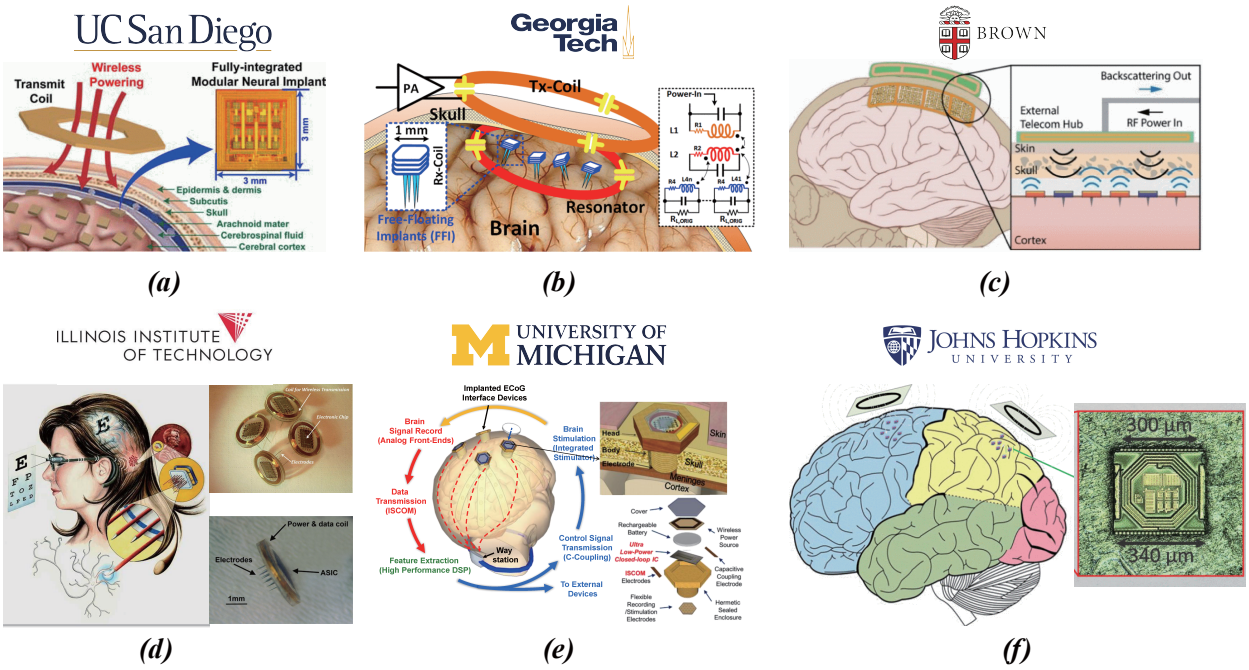


Figure 2.6: Examples of electromagnetic power transfer systems for distributed implants: (a) Encapsulated neural interfacing acquisition chip (ENIAC) [55]; (b) Distributed free-floating wireless implantable neural recording (FF-WINeR) system [57, 58]; (c) Human neurograin network with a 4-quadrant resonator [62]; (d) Wireless floating microelectrode array (WFMA) for intracortical visual prosthesis (ICVP) [64, 65]; (e) Distributed wireless ECoG recording systems [66]; (f) Scattered microbead implantable wireless neural stimulator [67].

for rodents over the past decade. There has been significant work on retrofitting cages with a wireless power transfer system to provide uniform power coverage of an entire cage [68, 69]. For example, 3D resonators wounded around the cage can extend the power coverage effectively. Overlapping planar coils with dedicated phase control [59] improves the delivered power to free-positioned Rx devices. A simplified approach in [61] utilises an array of planar PCB non-overlapping Tx coils to keep SAR within the safe limits for sub-mm Rx coils.

In addition, we cannot disregard the influence of the distance variation between the receiver and the transmitter on the wireless power transmission efficiency. A common way to attenuate this influence is to add relays among them such as resonators [70] or meta-materials [71]. Interference between wireless power transmission and wireless data communication has also attracted widespread attention, with separate data and power transmission coils [72] or multiplexed coils using different frequency carriers [69].

D. Technical Challenges

The technical challenges of wireless power transmission for neural interfaces in the central nervous system are summarised according to the following four aspects.

Challenges 1- Low power transfer efficiency: This property is caused by weak coupling between the transmitter and receiver over a large distance (a distance larger than Rx outer diameter $d_{Tx-Rx} \gg D_{Rx}$), scattering and reflection of electromagnetic fields on the surface of the biological tissues, as well as absorption of electromagnetic fields in biological tissues.

Challenges 2 - Non-uniform power coverage: The emerging distributed implantable devices require a wide range of power coverage. The free-positioning concept demands robust WPT against angular/positional misalignment and distance variation, especially considering the folded cerebral cortex and the brain micro-movement in the skull.

Challenges 3 - Interference and intermodulation: Interference between the wireless power and data carriers, and intermodulation among communication channels are inevitable. The wireless power transmission requires a narrow band antenna with a high Q factor to maximise the power transfer efficiency, but a wide bandwidth and low quality factor antenna is desirable for the wireless data communication system to achieve a high throughput data rate. If the same antenna is multiplexed with power wireless transmission and wireless data communication, the antenna design specifications must be conformed to a compromised scheme.

Challenges 4 - Safety limitations: The safety considerations for implantable medical devices focus on heat dissipation and EM radiation. The neurons in the central nervous system are the extremely sensitive to heat dissipation, and the recommended temperature variation is less than 1°C [73]. Inductive power transfer for implantable medical systems must meet the safety standards of the IEEE standard C95.1-2005 of SAR requirements ($< 1.6\,\mathrm{W/kg}$) [26]. Also, the EM interference safety of implantable medical devices should take into consideration, such as the compatibility with metal detectors at airports, and MRI in hospitals. Finally, cyber security has also attracted public attention, as implantable devices have network access capabilities [74].

2.2.2 Ultrasonic Power Delivery

Ultrasound has been widely used in many fields including medical imaging, non-destructive testing, underwater communication and wireless power transfer via biological tissues or through steel walls. However, ultrasonic wireless power transmission did not attract attention because of the low wireless power transfer efficiency in short-range compared with electromagnetic wireless power transmission. Recently, researchers [75, 76] have attempted to utilise ultrasonic energy to deliver power wirelessly for implantable medical devices because the ultrasound propagation in biological tissues is safer than that of electromagnetic fields. In the following subsections, we first introduce the operating principles and then we reveal the current trends and technical challenges.

A. Principle of Operation

The core component of an ultrasonic transmission system is the piezoelectric transducer, as shown in Figure 2.1(c). Both the transmitting and receiving devices have piezoelectric transducers for electrical and vibration conversion. The brief workflow of the entire system is that the transmitting device first converts the electric energy into ultrasonic waves which propagate into the body tissue to the implanted receiver. Next, the receiving piezoelectric transducer converts the ultrasonic vibration into an alternating voltage and passes through the power management circuitry, which provides the power supply for the implantable microelectronic system.

B. Ultrasonic vs. Electromagnetic Power Transfer

Ultrasonic waves have the following three advantages over electromagnetic waves in the biological environment.

(1) Low Loss in Tissue: The ultrasonic loss in biological tissues is considerably less than that of electromagnetic waves. Since the transmission of sound waves is through compression and stretching of biological tissues, it avoids electromagnetic radiation and displacement

currents on the surface of the skin and eddy currents in body tissues.

(2) Short Wavelength: The low propagation speed of the ultrasonic wave (10^5 times slower than the electromagnetic waves) makes the wavelength of the ultrasonic wave shorter at low frequencies, which is advantageous to Rx miniaturisation.

(3) Undemanding Safety Regulations: Ultrasonic safety regulations with regard to the human body are relatively loose compared to the stringent regulations for electromagnetic radiation. The intensity of the ultrasound that biological tissue can withstand is approximately nine times that of the electromagnetic fields. [26, 27]

C. Technical Challenges

Ultrasound can effectively penetrate most soft biological tissues except for bones. This capability occurs because of an impedance mismatch between hard bone and other soft tissues. Thus, ultrasound has been widely used in medical imaging and diagnosis. Figure 2.7 shows examples of ultrasonic power transfer through biological tissues. For neural interfaces, ultrasonic power delivery systems usually apply to the peripheral nervous system [75, 77, 78] since the biological central nervous system is shielded by bones such as the skull or the spine. In addition, it is difficult for ultrasonic waves to achieve high transmission efficiency and power density over a short distance. According to recent research [79], the efficiency of ultrasonic transmission is usually less than that of electromagnetic power transmission. However, ultrasound provides deeper penetration in body tissues and supplies sufficient energy for the implants over extended distances, while electromagnetic power transmission has entered the far-field region where its efficiency decreases significantly. It is necessary to account for the horizontal positional variations and angular offsets caused by biological movement during wireless transmission, and ultrasonic transmission is very susceptible to misalignment; there is no practical solution, yet.

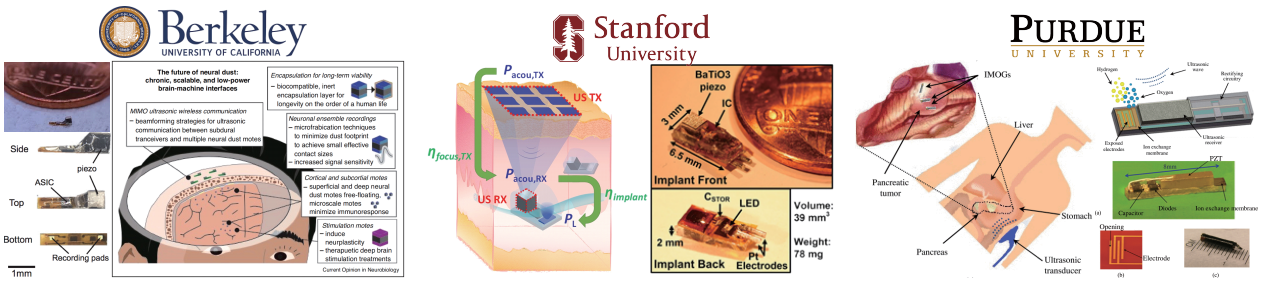


Figure 2.7: Examples of ultrasonic power transfer systems for distributed implants: (a) neural dust [75]; (b) ultrasound powered mm-sized implant [76, 80]; (c) implantable micro-oxygen generator [81].

D. Current Trends

The development trends of ultrasonic energy transmission systems are similar to those of electromagnetic transmission systems. The focus is on the improvement of transmission efficiency, the minimisation of the implanted devices, and the uniform energy coverage for distributed nodes. Similar to electromagnetic power transfer, three key parameters that affect the power transfer efficiency are the effective sensing area of the receiver A_{Rx}, the distance between the transmitter and the receiver d_{Tx-Rx} and the operating frequency f. For millimetre-depth implantable devices, electromagnetic wave wireless energy transfer is more efficient, while for centimetre-depth implants, ultrasonic energy transfer is preferred.

2.2.3 Other Energy Harvesting

The optical power transmission method relies on photovoltaic cells to harvest optical energy from an external energy source (such as LEDs, laser diodes), as shown in Figure 2.1(e). It often uses near-infrared or infrared regions, also known as therapeutic window wavelengths [82], to take advantage of the minimal loss mechanisms in biological tissues. The efficiency of photoelectric energy conversion depends on the area of the photovoltaic cells, the distance from the light source [83], material, structure, and thickness of photovoltaic cells [18]. Optical energy transmission is proportional to the effective area of the photovoltaic cell instead of the area squared, as compared to electromagnetic coupling. This feature makes optical power transfer

into implanted electronics a worthwhile investigation. However, optical energy transmission also has undeniable weaknesses. The light penetration loss in tissue mainly caused by the light absorption in epidermis layer and dermis layer [84]. Also, the reflections and refractions not to be neglected due to propagation in multi-layered biological tissues and scattering in anisotropic biological tissues. These effects determine the inherent inefficiencies of optical transmission.

Among emerging energy harvesting methods in Figure 2.1(f), for example, glucose [28] or adenosine triphosphate [29]currently can not provide sufficient power levels for the required form factor or the acceptable lifetime.

2.3 Wireless Data Communication

The requirements for neural interface data communications vary from 10 Kbps to 100 Mbps data rate, from several millimetres to centimetres in distance, and from simplex, half-duplex to full-duplex modes. Typically, we define the downlink and uplink according to the direction of data transmission in the neural interface where the downlink is defined as the communication from the external transmitter to the implantable devices; the opposite direction is referred to as the uplink. The downlink is usually utilised to send commands to the implants, while the uplink transmits raw or compressed recorded data from electrodes to the external devices. For distributed implanted devices, the throughput demands for the uplink rapidly increase as the number of distributed implanted devices increases.

2.3.1 Downlink Data Telemetry

There are two main implementations of the downlink: data carrier modulation [72, 85], and pulse based modulation [86]. The most common implementation is the use of a single carrier for amplitude (ASK), phase (PSK), frequency (FSK) and load shift keying (LSK). The advantage of this approach is the simple system structure for low power consumption with limited data throughput. The proposed scheme in [72] has separate power and data carriers in or-

thogonally positioned coils to reduce the interference, but this approach increases the volume and complexity of the wireless system. Pulse-based data telemetry has been proposed by using pulse harmonic modulation [87] or pulse delay modulation [72] to transmit sharp pulses at a certain amplitude or timing to represent 0 or 1 data bits. The advantage of this approach is the minimum interference between the power and data transmission, but the receiving side requires complex demodulation circuitry.

2.3.2 Uplink Data Telemetry

In general, uplinks are classified into passive and active data telemetry. Most researchers [85, 88, 89] regard passive data telemetry as a practical solution for neural interfaces because it consumes orders of magnitude of lower power than conventional radio communications due to the backscattering principle, which reflects the energy from the transmitter. Conventional methods of passive data telemetry are ASK, FSK, on-off keying, and LSK. The other advantages of backscattering are the following: (1) the multiplexed antenna between receiving the power and transmitting data, thereby saving the volume of the implant; (2) the elimination of the data carrier by avoiding the power-hungry oscillator and mixer, thereby simplifying the modulation circuit.

The apparent disadvantage of passive data telemetry is the challenge of maintaining simultaneous stable power transfer and high throughput data transmission. Thus, the throughput of passive data telemetry is generally less than 10 Mbps. When the uplink requires high data throughput, it applies UWB-based active data telemetry. This active transmission requires a considerable amount of power to generate the data carrier and can achieve a data throughput of over 100 Mbps. The innovative IR-UWB [86, 90] can use a sharp digital pulse to drive a wideband antenna to simplify the modulation module in the implant microelectronic system with a reduction in the power consumption. Recently, low-power, high-throughput active data links [91, 92] are proposed based on IR-UWB combined with pulse position modulation (PPM) and pulse width modulation. Although these modulations simplify the structure of the electronic circuits at the implanted side, it complicates the external demodulation circuits and

requires a large amount of energy for demodulation.

Commercial medical implant communication system (MICS) band of 402 MHz - 405 MHz has been utilised in data communication for implantable medical devices and wearable devices. Texas Instruments and Microsemi (previously Zarlink) have released commercially available MICS components CC1101 and ZL70103. These data transceivers have been implemented into pacemakers, implantable insulin pumps, bladder control monitors and other medical devices [93].

The challenging requirements have also been placed on wireless data communication to conform to the trend of distributed medical implants. The massive data collected from multiple implants demand to be transmitted to an external receiver. Current preliminary research, mainly based on mature wireless communications in modern mobile technologies, can be divided into three categories: time division multiple access (TDMA), frequency division multiple access (FDMA), and code division multiple access (CDMA). The CDMA technique has been applied to the ultrasonic powered Neural Dust [94]. It implements amplitude modulation by employing ultrasonic echoes. Neurograin [62] leverages TDMA technology to enable simultaneous communication with 64 ASICs by using binary phase-shift keying (BPSK). In addition, ENGINI [95] uses an on-chip tuning LC tank to achieve frequency modulation to realise frequency division technology.

Chapter 3

Chip-Scale Receiving Coils for Millimetre-Sized Bio-Implants

"The aim of science is to seek the simplest explanations of complex facts."

– Alfred North Whitehead, 1861 - 1947

This chapter presents three different types of mm-scale Rx coils for implantable medical devices. They are named as *in-CMOS* (standard CMOS process), *above-CMOS* (planar coil post-fabricated on silicon substrate) and *around-CMOS* (helical wirewound coil around silicon substrate). The analytical and simulation models have been developed and verified through fabrications and experimental measurements in air and biological environment. This chapter selects the basic 2-coil inductive link as a reference system architecture to demonstrate the advantages and disadvantages of these three types of receiving (Rx) coils.

This work was done in collaboration with Pyungwoo Yeon, Yuhua Cheng, and Maysam Ghovanloo. Pyungwoo Yeon and Maysam Ghovanloo were with the GT-Bionics Laboratory, Georgia Institute of Technology, Atlanta, USA. Yuhua Cheng is with Hangzhou Dianzi University, Hangzhou, China. The Analytical model of the around-CMOS coil was contributed by Yuhua Cheng. The simulation, fabrication and measured results of the around-CMOS coil were contributed by Pyungwoo Yeon. All other aspects were my contribution. A portion of the work presented in this chapter has been published in [96–98]

3.1 State of the art

The inductive coupled link is one of the most crucial components in wireless power transmission systems because it has the weakest power transfer efficiency compared to other components. Furthermore, the inductive link design determines the overall performance of the peripheral power management circuitry due to impedance matching and resonance tuning frequency. In particular, the quality (Q) factor of the receiving coil determines the efficiency of the inductive link. Thus, the Rx coil is a key component and designing high Q factors is the first step to build the entire wireless system.

Since the size of the implant is restricted to the millimetre level or preferably sub-millimetre level with strict biocompatibility requirements, conventional copper coils on the market are not suitable in implantable biomedical systems. The toxicity of copper is well known. The recent EU Medical Device Regulations (MDR) and US Food and Drug Administration (FDA) guidance are required all implants to be compliant with MRI from May 2020 [99]. However, most conventional coils are made of copper or have a ferrite core, these materials are not compatible with the MRI system. Therefore, the implantable inductive coil have to design in house with biocompatible conductors, core materials or substrates.

A silicon substrate is desired biocompatible material, because the microelectronic system requires a full-custom integrated chip (IC) for power management, data communication, neural signal recording or processing. Depending on the position of coils relative to silicon substrates, the types of coils are divided into *around-CMOS*, *above-CMOS*, *in-CMOS*. The around-CMOS coils are solenoids which the conductor is wound around the periphery of the silicon substrate. The above-CMOS and in-CMOS coils have planar spiral coils structures on a silicon substrate, which are usually defined by photolithography. Relevant types of coils in the current references will be reviewed separately in accordance with the above three categories.

3.1.1 Around-CMOS coil (Solenoid)

Around-CMOS coils have three-dimensional structures which can generate uniform magnetic fields. The fabrication method for mm-scale around-CMOS coils are categorised as: wirebonding, release folding, and surface micromachining.

Most mm-scale coils' fabrication relies on semi-automatic or automatic wire bonders and fully customised fixtures to define their geometric dimensions, such as outer diameter and trajectory spacing. 1 mm diameter wire-bonding around-CMOS coil achieves Q = 10 at 50 MHz [100], as shown in Figure 3.1(a). However, the exposed wire is inconvenient to form an enclosed cavity regarding implantable medical devices, especially from the packaging perspective.

The release folding process generates standing mm-sized solenoid on silicon substrate, after metal layer deposition and patterning. 2 mm standing solenoid has Q = 100.9 at 300 MHz [101], as shown in Figure 3.1(b). However, the fragile structure is not suitable for the integration of biological implants.

Hollow core solenoids are fabricated by surface micromachining processes, such as substrate etching, anodic bonding, metal deposition, pattern, electrode plating [102], as shown in Figure 3.1(c). The hollow cavity can provide the protection for inside microelectronics, but this hollow core solenoid lacks electromagnetic characteristic measurement.

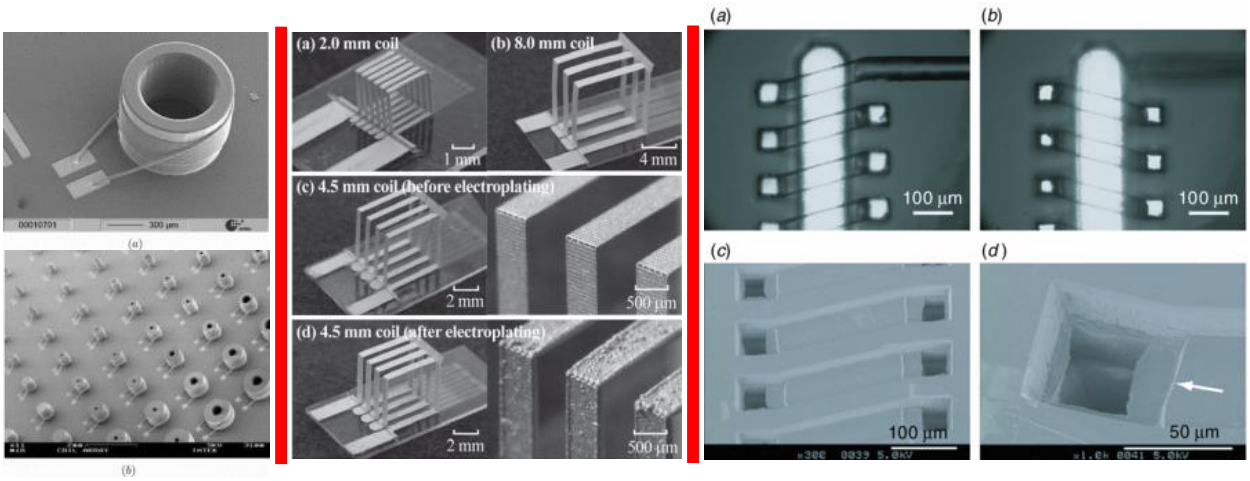


Figure 3.1: Examples of mm-scale around-CMOS coils (solenoid): from left to right: (a) Bonding wire wounded coil [100]; (b)Standing coil [101]; (c)Hollow core solenoidal microcoils in borosilicate glass [102]

3.1.2 Above-CMOS and in-CMOS coil (Planar spiral coil)

Above-CMOS and in-CMOS coils represent planar spiral structures which are mainly based on surface micromachining processes. These coils have a compact structure to ease microelectronic integration into implantable medical devices, while their fabrication can be accomplished by advanced CMOS technology. Unfortunately, planar coils designed and fabricated adopting commercially available CMOS processes typically have low inductances and high resistances which causes the Q factor to be limited to less than 10 in mm-scale [103]. However, post surface micromachine techniques have been applied to create a suspended coil [104] by etching the underneath silicon substrate or 90-degree coil [105] using surface tension and delicate structure design. These sophisticated methods improve the Q factor of the planar coil to approximately 20.

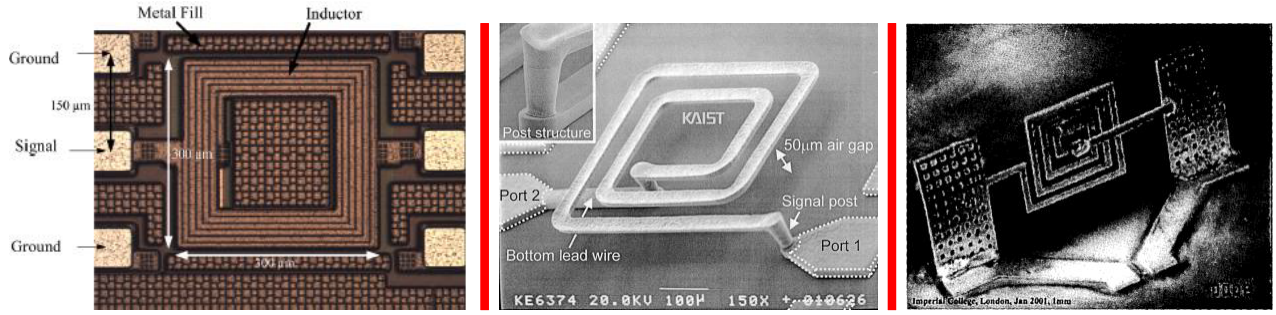


Figure 3.2: Examples of mm-scale above-CMOS and in-CMOS coils (planar coil): from left to right: (a) CMOS coil bt 90 nm CMOS RF technology [103]; (b)suspended spiral coil [104]; (c)vertical coil [105]

Table 3.1: Comparison between planar spiral coil and solenoid.

Parameter	Planar coil	Solenoid
Q factor	Low	High
Magnetic field uniformity	No	Yes
Volume	Low	High
Fabrication	Easy	Hard

3.2 Analytical Model

The analytical models of solenoids and planar coils are presented in this section. With the aid of these analytical models, we can quickly estimate the electrical characteristics of each coil

based on their geometry. Also, these models facilitate the optimisation of the 2-coil inductive link.

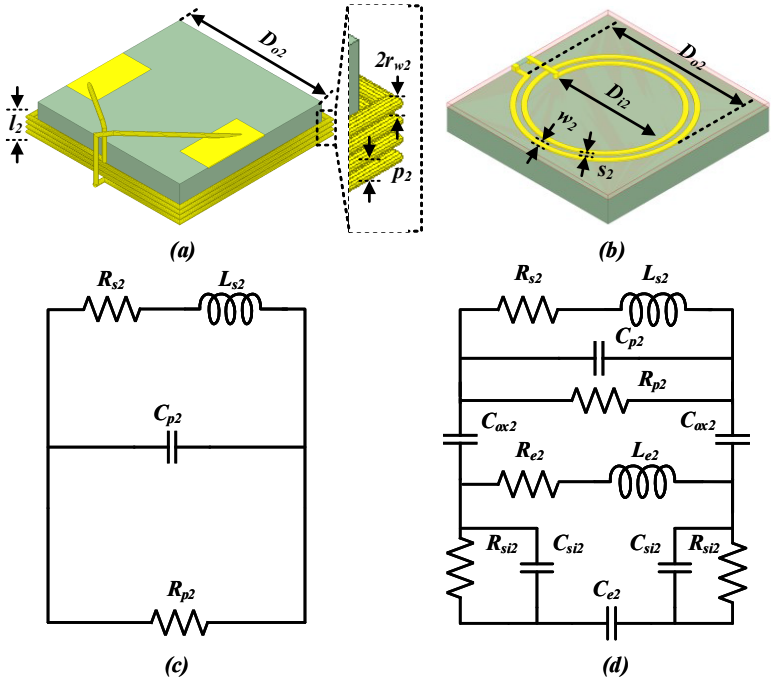


Figure 3.3: 3D models for (a) around-CMOS (i.e. wirewound) coil; and (b) in-CMOS and above-CMOS (i.e. on silicon substrate) coils, and equivalent circuit models for (c) around-CMOS coil and (d) in-CMOS and above-CMOS coils.

3.2.1 Around-CMOS (wirewound) coil model

The around-CMOS coil has a relatively simple equivalent circuit model because the silicon substrate loss is neglectable due to the considerable spacing between the silicon substrate and coil conductors. Key geometric parameters 3D model and equivalent circuit of the *around-CMOS* coil are illustrated in Figure 3.3(a, c). D_{o2} and D_{i2} are outer and inner diameter of all types of coils. r_{w2} is the wire radius and p_2 is the pitch among adjacent turns from centre to centre with l_2 being the solenoid height. The lumped elements in equivalent circuits depend on the geometric dimensions. Here we adopted the analytical model of from [106] for mm-scale *around-CMOS* coil. In order to calculate Q factor of this type of coil, the serial and parallel resistance R_{s2}, R_{p2}, serial inductance L_{s2}, and parallel capacitance C_{p2} in equivalent circuit has to be calculated individually. The serial inductance L_{s2} is proportional to the square of turns N_2. We introduces two correction factors K_P and K_L to accurately estimate serial inductance

L_{s2}. They are effective pitch K_P due to proximity effect and non-uniform magnetic filed K_L across the solenoid, respectively.

$$L_{s2} = \mu_{eff}\pi r_{HF}^2 N_2^2 K_P K_L, \tag{3.1}$$

$$K_P = 0.00875(\frac{p_2}{r_{w2}})^2 + 0.035\frac{p_2}{r_{w2}} + 0.83, \tag{3.2}$$

$$K_L = \frac{1}{l + 0.4502D_{o2}}. \tag{3.3}$$

In above equation 3.1, U_{eff} is effective magnetic permeability determined by the relative permeability of surrounding materials. r_{HF}, the effective wire radius considering the skin effect at operating frequency, can be written as [106]

$$r_{HF} = \frac{0.5D_{o2}(1-(2r_{w2}/D_{o2})^2)(p_2/2r_{w2}-1)+D_{o2}-2r_{w2}+2r_{w2}/N_2}{p_2/2r_{w2}+1}. \tag{3.4}$$

In order to calculate its Q factor, serial R_{s2} contains skin effect resistance, R_{sk}, and proximity effect resistance R_{pr} can be expressed as

$$R_{s2} = R_{sk} + R_{pr}, \tag{3.5}$$

where R_{sk} and R_{pr} can be expressed as

$$R_{sk} = \frac{R_{dc}m}{2}\left(\frac{ber(m)bei'(m)-bei(m)ber'(m)}{(ber'(m))^2+(bei'(m))^2}\right), \tag{3.6}$$

$$R_{pr} = \frac{-4\pi R_{dc}m}{\sigma}\left(\frac{ber_2(m)ber'(m)-bei_2(m)bei'(m)}{(ber(m))^2+(bei(m))^2}\right)\left(\frac{H_n}{I_0}\right)^2, \tag{3.7}$$

$$m = r\sqrt{\frac{\omega\mu_r\mu_0}{\rho}}, \tag{3.8}$$

$$R_{dc} = \frac{\rho l}{A} = \frac{2\mathrm{N}_2\rho}{\mathrm{r}_{w2}}, \tag{3.9}$$

where $ber(m)$ and $bei(m)$ are Kelvin functions [106]. ρ is the conductor resistivity, and H_n is the magnetic fields under the net current flowing through the solenoid coil I_0, μ_r is the relative permeability of the conductor. C_{p2} and R_{p2} are predicted by practical curve-fitting coefficients

in [106]. The total impedance of this equivalent circuit can be written as

$$Z = (R_{s2} + \omega L_{s2}) \parallel \frac{1}{\omega C_{p2}} \parallel R_{p2}. \tag{3.10}$$

Thus, the Q factor of the all types of coils can be expressed as

$$Q = \frac{\mathrm{Im}(Z)}{\mathrm{Re}(Z)}. \tag{3.11}$$

3.2.2 In-CMOS and Above-CMOS (substrate-based) coil model

Figure 3.3(b) is the 3D model and Figure 3.3(d) is the equivalent circuit model. They are valid for both in-CMOS and around-CMOS coils. These two types have more complex analytical model than around-CMOS one, because of non-negligible substrate loss where the conductor is close to the silicon substrate. key geometrical parameters are w_2 the trace width, and s_2 the spacing between adjacent traces. D_{o2} and D_{i2} are outer and inner diameter, respectively. The substrate loss can be modelled by parasitics elements: R_{si2} the substrate resistance determined by majority carrier concentration, C_{si2} the substrate capacitance caused by the relative permittivity of silicon substrate, and C_{ox2} the silicon oxide capacitance [107]. The eddy current generates in the silicon substrate due to current flow in inductor. It can be estimated using lumped resistance R_{e2}, inductance L_{e2}, and capacitance C_{e2}. The serial inductance of this type can be precisely calculated by using current sheet approximation technique from [108].

$$L_{s2} = \frac{c_1 \mu_{eff} {N_2}^2 D_{avg}}{2} \left(\ln\left(\frac{c_2}{\phi}\right) + c_3\phi + c_4\phi^2 \right) \tag{3.12}$$

where average diameter ϕ is

$$D_{avg} = \frac{\mathrm{D}_{o2} + D_{i2}}{2}, \tag{3.13}$$

where filling factor ϕ can be expressed

$$\phi = \frac{D_{o2} - D_{i2}}{D_{o2} + D_{i2}}. \tag{3.14}$$

Coefficients c_1 to c_4 are relate to the shapes of the this type of coils and their values are listed in below table [108].

Table 3.2: Coefficients for in-CMOS and above-CMOS coil inductance calculation.

Shape	**C1**	**C2**	**C3**	**C4**
Circle	1.00	2.46	0.00	0.20
Octagonal	1.07	2.29	0.00	0.19
Hexagonal	1.09	2.23	0.00	0.17
Square	1.27	2.07	0.18	0.13

Similar to around-CMOS coil, parasitic series resistance R_{s2} is the sum of R_{sk} and R_{pr}. The equation for R_{pr} can be borrowed from (3.7). But R_{sk} can be simply estimated by

$$R_{sk} = \frac{R_{dc} t_2}{\delta(1 - e^{-t_2/\delta})}, \tag{3.15}$$

$$R_{dc} = \frac{\rho l_2}{w_2 t_2}, \tag{3.16}$$

$$\delta = \sqrt{\frac{\rho}{\pi \mu_r \mu_0 f}}, \tag{3.17}$$

where t_2, w_2 and l_2 are the thickness, width and length of conductor tracks, respectively. Same to the around-CMOS coil model, the parallel parasitic capacitance C_{p2} and resistance R_{p2} are caused by the inherent dissipation of electromagnetic energy in dielectric coating materials and the biological tissues. Besides, substrate loss is represented by substrate capacitance C_{si2}, substrate resistance R_{si2}, and silicon oxide capacitance C_{ox2} from [109].

$$C_{si2} = \frac{l_2 w_2 C_{Sub}}{2}, \tag{3.18}$$

$$R_{si2} = \frac{2}{l_2 w_2 G_{Sub}}, \tag{3.19}$$

$$C_{ox2} = \frac{l_2 w_2 \varepsilon_{ox2}}{2 t_{ox2}}, \tag{3.20}$$

where the unit capacitance and conductance of silicon substrate are represented as C_{Sub} and G_{Sub}. t_{ox2} and ε_{ox2} are the thickness and permittivity of silicon dioxide. Parasitic inductance L_{e2} and resistance R_{e2} are evaluated by empirical equations of eddy current in silicon substrate

from [110–112].

$$L_{e2} = 10^{-6} {d_{o2}}^{0.98} {w_2}^{4.39} {s_2}^{-0.99} {N_2}^{-1.84} {L_{s2}}^{0.68}, \tag{3.21}$$

$$R_{e2} = 39 {N_2}^{1.3} (w_2 + s_2)^{0.93} {l_2}^{-1.4}. \tag{3.22}$$

The total impedance of this equivalent circuit can be written as

$$\begin{aligned} Z = {} & (R_{s2} + \omega L_{s2}) \parallel \tfrac{1}{\omega C_{p2}} \parallel R_{p2} \parallel \\ & \left(\tfrac{1}{2\omega C_{ox2}} + \left((R_{e2} + \omega L_{e2}) \parallel \left(\tfrac{1}{2} \left(R_{si2} \parallel \tfrac{1}{\omega C_{si2}} \right) + C_{e2} \right) \right) \right) \end{aligned} . \tag{3.23}$$

Thus, the Q factors of the above-CMOS and in-CMOS coil are written as equation 3.11.

3.3 Coil Design and Fabrication

3.3.1 Description of Simulation Model

HFSS (ANSYS, Canonsburg, PA) is a 3D full-wave EM field solver based on finite element analysis (FEA). EM properties of the three types of two-coil inductive links are simulated and evaluated by meshing 3D geometric models. The cross-section of the simplified six-layer human head model with three types of mm-scale Rx coils is shown in Figure 3.4. The volume of the head model is 10 cm×10 cm×5 cm. Rx coils L_2 are placed in CSF and above the brain layer, covered with 100 μm of polydimethylsiloxane (PDMS). Tx coil L_1 is placed above head model with a 0.6 mm air gap. The dielectric properties of skin, fat (subcutis), skull, cerebrospinal fluid (CSF), dura, and brain vary according to operating frequency. Their dielectric value from 10 MHz to 1 GHz is fed into this EM simulation model based on [113].

The geometric dimensions and material properties of the Tx and Rx coils are presented in Table 3.3. Six different Tx coils are used to maximise the PTE of the three types of 2-coil links in two different surrounding environment (in air and head models). All Tx coils are designed in cm-scale with cooper foil on FR4 substrate for fast prototyping. The conductivity of copper ($5.96 \times 10^7 S/m$) is higher than gold ($4.10 \times 10^7 S/m$) or aluminium ($3.77 \times 10^7 S/m$),

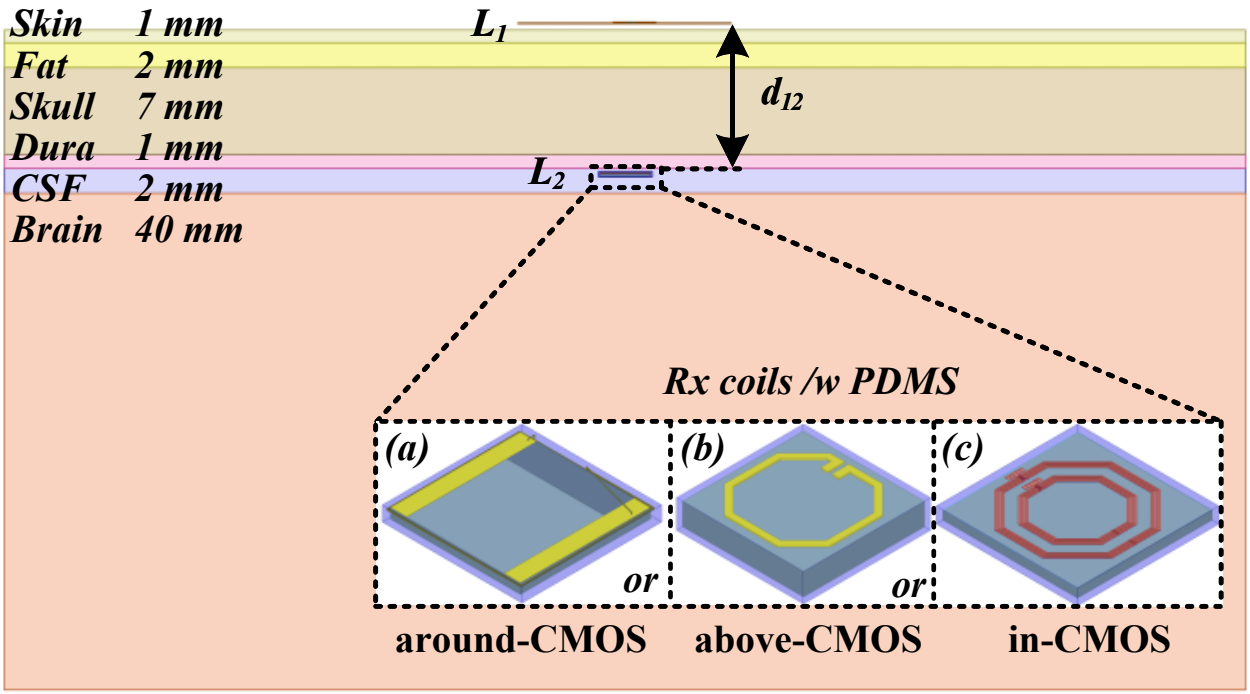


Figure 3.4: Cross-section of the HFSS simulation model to indicate the relative positions of the Tx L_1 and Rx L_2 coils. Inset: Rx coil models with PDMS coating (a) *around-CMOS* (wirewound coil, WWC); (b) *above-CMOS* (microfabricated MEMS); (c) *in-CMOS* coils.

and this reduces track resistance and improves the Q factor of Tx coil. Detailed specifications of the the Tx coils are listed in Table 3.3. The inset in Figure 3.4 shows the three different Rx coil structures:*around-CMOS* (with insulated bond-wire); *above-CMOS* (post fabricated); and *in-CMOS* coils. The *around-CMOS* coil consists of an insulated Au bond wire with a 25 μm diameter and a 4 mm×4 mm silicon substrate with two bonding pads. The design process of the in-CMOS coil has three steps. First, we develop Visual Basic for Applications (VBA) scripts to automatically generate 3D STL files in CST Microwave Studio (Dassault Systèmes Simulia Corp., Vélizy-Villacoublay, France), in order to adjust the key geometric parameters of in-CMOS coil conveniently for dimensions sweep. Second, the generated 3D models are simulated in HFSS by using frequency-domain EM solver to identify the optimal design. The last step is importing GDS files into the Virtuoso Layout Suite (Cadence Design Systems Inc., San Jose, CA). However, the in-CMOS coil has to obey the design rules of mature CMOS technology (AMS 0.35 μm 4M, 2P, 50 V, H35B4S1, ams AG, Austria). The final layout is generated by Skill polygon creation scripts, and all coordinates are calculated in Matlab (MathWorks, Natick, Massachusetts, USA). In AMS H35B4S1 process, all metal layers are made of aluminium. Layer

3 and layer 4 are connected in parallel using VIA3 to achieve 4 μm thickness for conductive track. Five 10 μm slots must be added to metal traces to meet the design rules and relieve the surface tension of the large metal layers. The structure of the above-CMOS coil has a thick gold layer 25 μm on silicon substrate, which is relatively simple in comparison with other two types.

Table 3.3: Optimal geometries and electrical properties of Rx coils.

Types	*Around-CMOS*		*Above-CMOS*		*in-CMOS*	
Medium	Air	Tissue	Air	Tissue	Air	Tissue
Material	Cu	Cu	Cu	Cu	Cu	Cu
L_1[nH]	29.9	38.5	42.9	20.2	46.5	24.56
$R_1[\Omega]$	0.304	0.907	0.11	0.13	0.38	0.41
Q_1	370.8	80.2	269.55	58.58	321.2	124.2
D_{o1}[mm]	28	17.2	32	24	36	26
w_1[µm]	5000	600	6000	6000	6000	6000
t_1[µm]	70	70	35	35	35	35
p_1[µm]	N/A	N/A	N/A	N/A	N/A	N/A
N_1	1	1	1	1	1	1
Material	Au	Au	Au	Au	Al	Al
L_2[nH]	82.5	63.7	4.56	4.57	6.51	5.68
$R_2[\Omega]$	10.05	4.97	0.15	0.09	1.47	1.39
Q_2	38.93	24.23	21.02	18.45	11.82	8.47
Q_{2L}	25.95	15.29	18.56	10.81	8.11	4.24
D_{o2}[mm]	4	4	4	4	4	4
w_2[µm]	25	25	250	250	175	175
t_2[µm]	25	25	25	25	4	4
p_2[µm]	30	30	N/A	N/A	N/A	N/A
N_2	2	2	1	1	1	1
d_{12}[mm]	12	12	12	12	12	12
k_{12}	0.013	0.0093	0.018	0.009	0.010	0.008
f_0[MHz]	600	300	110	60	426	330
PTE[%]	26.3	3.88	19	2.12	8.18	1.68

3.3.2 Optimisation

According to equation 2.14, the PTE optimisation can be divided into two figures of merit due to weak coupling between Tx and Rx, which is less than 0.01. The PTE is expressed as

$$PTE = k_{12}^2 Q_1 \times Q_{2L}\eta_{Rx} = Tx_{FoM} \times Rx_{PRS} \tag{3.24}$$

where the Tx figure of merit (FoM), Tx_{FoM}, indicates the Tx power transmission capacity. This parameter shows how much power can be transmitted by Tx through a weak coupling inductive link. Rx power reception susceptibility, Rx_{PRS}, represents Rx power acceptance efficiency. It displays the amount of received power at load side [38]. In equation 3.24, k_{12} is the inductive link coupling coefficient between Tx and Rx coils. Q_1 and Q_{2L} are the Q factors of the Tx and Rx coils with the load resistance. η_{Rx} depends on the power loss in the secondary LC tank due to its parasitic resistance, R_{s2}.

The geometric optimisation of Tx and Rx coils is performed independently, based on [38, 106, 114]. The simplified equivalent circuit models of 2-coil inductive links are shown in Figure 3.5(a). For the specific tuned resonant frequency f_0, the primary side is chosen as a serial $L_{s1}C_1$ tank to keep input resistance as R_{s1}, as compared to $1/(\omega^2 R)$ input resistance for parallel LC tank. The parallel $L_{s2}C_2$ tank is preferred for the secondary side, since it results in a larger loaded Q factor [38,106]. The secondary side circuit for all types of coils are simplified with substrate loss as shown in Figure 3.5(b). The equivalent load resistance $R_L = \omega L_{s2}^2/(R_{L,O}||R_{p2})$ in parallel with substrate impedance $R_{sub} = \mathrm{Re}\left(1/(jwC_{ox2}) + R_{si2} \parallel 1/(jwC_{si2})\right) = R_{si2}/\left(1+\omega^2 C_{si2}^2 R_{si2}^2\right) \approx$ R_{si2} is composed of the practical load impedance on the secondary side. For instance, the resistance for a high-resistivity silicon substrate with p-type $7.22 \times 10^{12} cm^{-3}$ doping concentration is $R_{si2} \approx 2.69 k\Omega \cdot cm$ [115], which is suitable for low-loss, high-performance microwave components, especially for high-Q inductors. If the load resistance R_L is larger than R_{si2}, the substrate loss cannot be ignored.

There are several methods to reduce the substrate loss for above-CMOS and in-CMOS coils. From design perspectives, advanced techniques are parallel connected multiple metal layers [116], or patterned ground shields [117], shown in Figure 3.2(a). These techniques have resulted in modest Q factor improvements. From microfabrication perspectives, many CMOS-compatible post-fabrication methods have been proposed to boost the Q factor such as developing suspended coils above the substrate [104, 118] as shown in Figure 3.2(b), or replacing silicon substrate with the polymer by using through-silicon-vias [119].

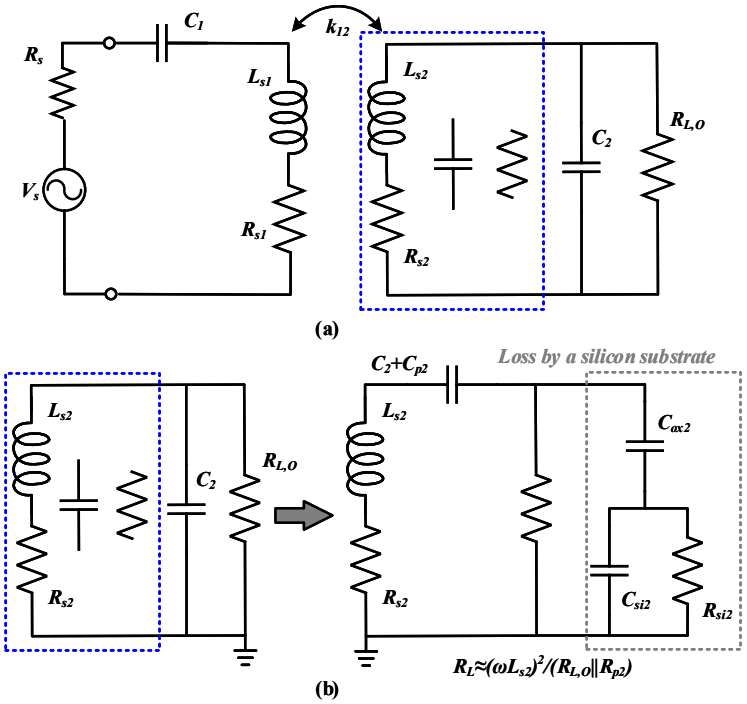


Figure 3.5: Equivalent circuit models for: (a) 2-coil inductive link for powering mm-scale Rx coil; (b) mm-scale Rx coil with a silicon substrate.

A. Design Constraints

The typical distance between the Tx and Rx coil is considered to be $d_{12} = 12\,\text{mm}$ [40] for fair PTE comparison among three types of coils, which is the nominal scalp-to-cortex distance. Tx and Rx coils are aligned in the centre to achieve maximum PTE. Before performing individual optimisations for these 2-coil inductive links, the load resistance is selected as 9 kΩ at 1 V_{rms} for delivering 111 μW in the secondary LC tank. Also, the size of the silicon substrate is chosen to be 4 mm×4 mm based on the area estimation of the integrated electronics and packing for implantable devices.

For the around-CMOS coil, pitch p_2 and wire radius r_w are non-adjustable parameters because p_2 cannot be controlled precisely by semi-manual wire bonder. The maximum wire diameter for this semi-manual wire bonder is 25 μm. The gold bonding wire is chosen over an aluminium one to minimise serial resistance. The constraints of in-CMOS coils are the conductor thickness and the type of material. Metal thickness is defined by the CMOS process, and all metal material is aluminium for the AMS 0.35 μm 4M, 2P, 50 V process. The typical thickness of the first three metal layers is 0.64 μm. The top metal layer is 3 μm thick and interconnection via is 0.36 μm.

There are fewer constraints for the above-CMOS coil, due to its highly customizable geometric dimensions by the in-house microfabrication process.

After applying the common design constraints as stated above, Tx and Rx coils are designed by following conventional inductive links' optimisation procedure in [38, 43, 120] to maximise PTE within constrained SAR.

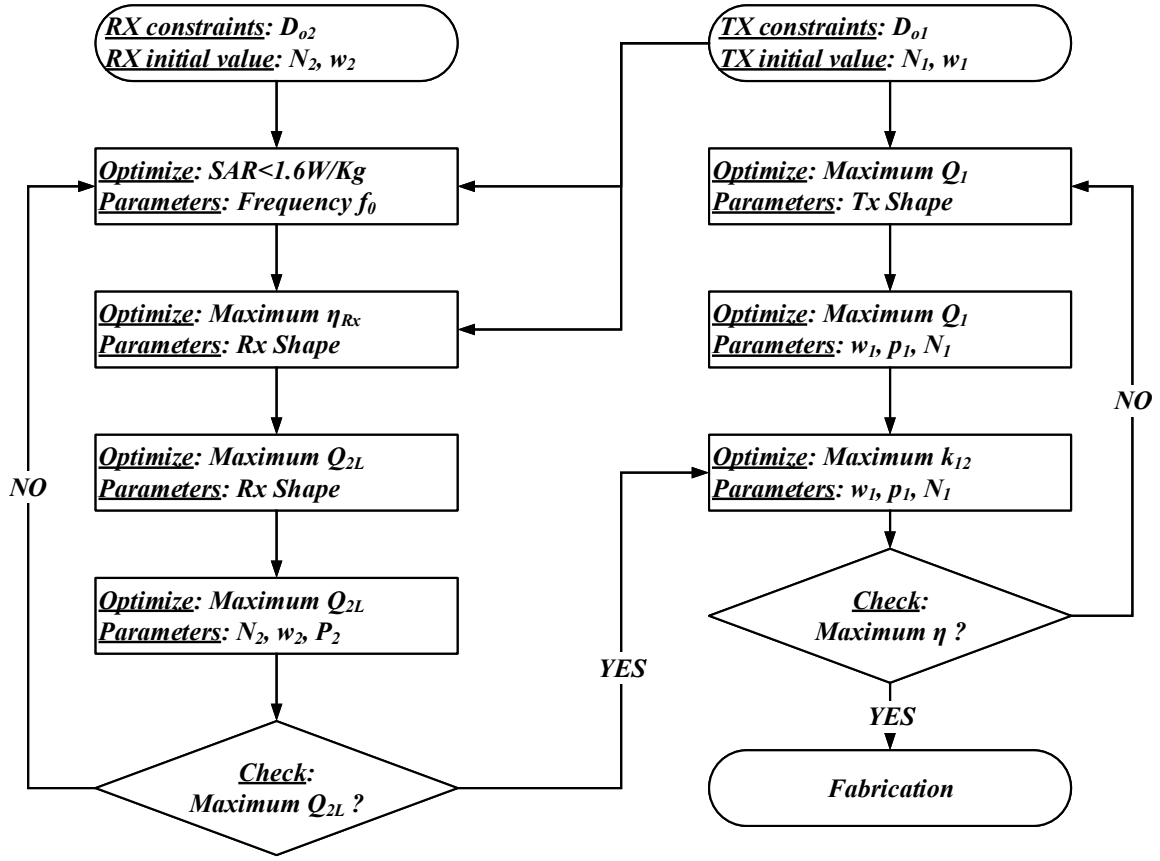


Figure 3.6: Iterative design procedure for 2-coil link PTE optimisation under constrained SAR.

B. Optimising Rx power reception susceptibility, Rx_{PRS}

According to equation 3.24, Rx power reception susceptibility Rx_{PRS} relates to loaded Q factor, Q_{2L}=$wL_{s2}/(R_{s2}+R_L)$, and the Rx internal efficiency, $\eta_{RX} = R_L/(R_{s2}+R_L)$). Serial inductance L_{s2} and resistance R_{s2} are defined in equations 3.1, 3.5, and 3.12, which relate to Rx geometric dimensions, such as turns N_2, track width w_2, thickness t_2, and spacing p_2.

For the around-CMOS coil, only the number of turns N_2 of the Rx coil can be optimised. It is

firstly swept by using Matlab, based on analytical model presented in Section 3.2, then verified in the HFSS 3D full-wave EM solver. For the in-CMOS coil, the planar structure limits its inductance, so its Q factor is mainly determined by the parasitic resistance [118]. The key parameters for optimisation are the number of turns N_2 and width-to-space ratio w_2/p_2 to reduce its serial resistance R_{s2} and parallel resistance R_{p2} caused by the proximity effect [53]. For the above-CMOS coil, the material of the conductor is selected as gold (Au) for its high conductivity and biocompatibility. The geometric dimensions can be optimised through the thickness metal layer t_2, width-to-space ratio w_2/p_2 and the number of turns N_2.

After following Rx optimisation process in Figure 3.6, the desired geometry of the implantable Rx coil tends to be one or two turns and the optimal trace width is smaller than the one in air. These results indicates that potential loss can be reduced by shrinking the contacting area with surrounding materials. The optimised geometric dimensions of three different types of Rx coils are listed in Table 3.3. In addition, comparisons of surrounding environment between air and biological tissue are performed in HFSS simulations to demonstrate the alterations of EM properties.

C. Optimising Tx figure of merit, Tx_{FoM}

This subsection states the Tx geometry optimisation process, since the Tx figure of merit contains the Q_1 factor and coupling coefficient k_{12}. According to equation 3.24, Tx_{FoM} is proportional to k_{12}^2 (<0.01). Thus, k_{12} is the key parameter to determine the Tx figure of merit. Coupling coefficient k_{12} is generally defined as [121]

$$k_{12} = \frac{M_{12}}{\sqrt{L_1 L_2}} = \frac{1}{[1 + 2^{-4/3}(\frac{d_{12}}{\sqrt{D_{o1} D_{o2}}})^2]^{3/2}}. \tag{3.25}$$

Note that k_{12} is independent of the number of turns N_1 and N_2, since L_1 and L_2 are proportional to N_1^2, N_2^2 and M_{12} is proportional to $N_1 N_2$. Also, k_{12} depends on the outer diameter of Tx and Rx coils, D_{o1} and D_{o2}. The optimal outer diameter of Tx coil, D_{o1} needs to take both the k_{12} and Q_1 into consideration. In addition, k_{12} is inversely proportional to the cube of distance d_{12}

between Tx and Rx coils. This implies Tx_{FoM} is mainly depends on the distance. However, the distance d_{12} is fixed at 12 mm in the simulation model according to the nominal scalp-to-cortex distance [40].

The SAR of 2-coil inductive links is a vital parameter to ensure biological tissues exposure to electromagnetic radiation is less than 1.6 W/Kg [26]. The simulated results of SAR in different tissues are shown in Figure 3.7 when transmitting power is fixed to 10 mW. For the above-CMOS coil, the inductive link operates at a lower 60 MHz frequency. The total SAR is far below to the limit. The rest of the two Rx coils operate at higher 100s MHz frequencies and their total SARs are below 0.75 W/Kg.

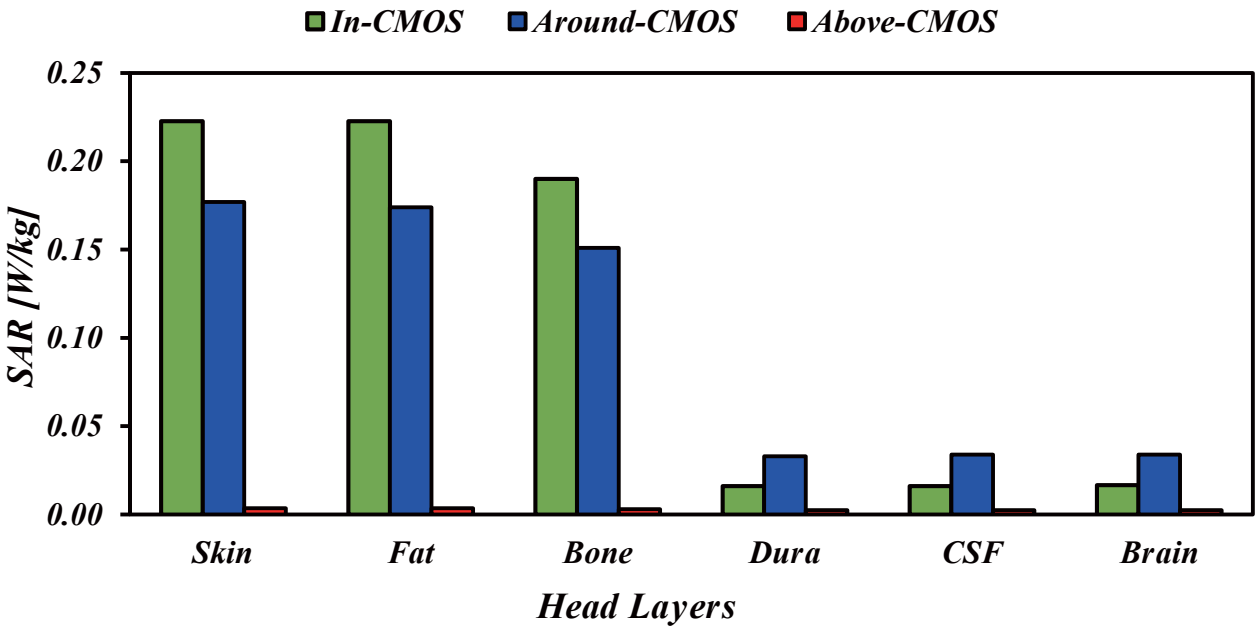


Figure 3.7: Simulated SAR in head model at optimal frequencies for in-CMOS, around-CMOS and above-CMOS coils with fixed 10 mW Tx power.

After optimization, the final geometrical dimensions and electrical properties of the 2-coil inductive link for three types of Rx coils are summarised in Table 3.3.

3.3.3 Fabrication

A. Wire-wound around-CMOS coil

The winding process of the around-CMOS coil begins by fixing a 4 mm×4 mm passive silicon die on the testing PCB, then ultrasonically bonding one terminal of insulated gold wire to the gold pad on the testing PCB, by means of the manual wire-bonder (Westbond 7476D, Anaheim, CA). The next step is stably rotating the PCB to ensure the bonding wire is wounded around silicon die by using a stepper motor to form the desired geometric dimensions of the coil. After reaching a targeted number of turns, the second terminal of bonding-wire is bonded to the other pad on the testing PCB. To keep the shape of coil and release the tension on two bonding points, instant glue is dripped onto the four corners of the die. For this case, wirebonding to PCB is only convenient for measuring purposes. In actual implantable devices, two terminals of coils will be connected to pads on the active CMOS die. More details of the fabrication procedure have been reported in [58].

B. Micofabricated above-CMOS coil

The microfabrication techniques of the above-CMOS coils contain photolithography and metal deposition. Its fabrication process is depicted in Figure 3.8. Firstly, a 50 nm chromium (Cr) adhesive layer and 100 nm Au seed layer are attached to a four-inch silicon wafer by electron-beam physical vapour deposition (PVD). Afterwards, positive photoresist AZ4562 (Microchemicals GmbH, Germany) is spin-coated twice on the wafer to achieve 28 μm thickness, then exposed and developed in Dilase 250 photolithography system (Kloe, France) to form the profile of coil. The final step is to increase the thickness of the gold layer up to 26 μm by 183 min electrochemical deposition. After removing global seed Au and adhesive Cr layer, the coil structure is left on the silicon wafer.

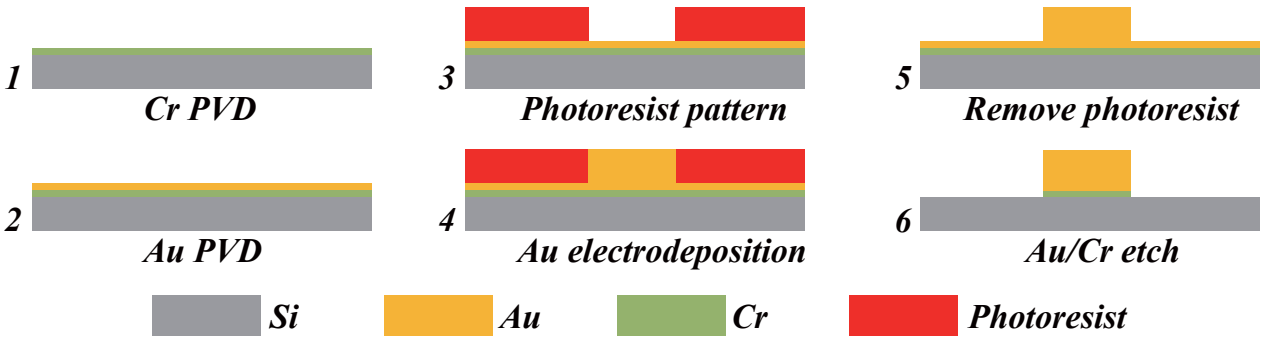


Figure 3.8: Process steps of the above-CMOS (micro-fabricated) coil.

C. Standard in-CMOS coil

The 0.35 μm CMOS technology chosen has a 3 μm thick top metal layer, which is preferable to passive RF devices. The AMS foundry is responsible for the in-CMOS coil fabrication. The pad arrangement is designed to comply with the pitch of Picoprobe Model 40A RF probe (GGB Industries, Inc., Naples, USA.) as ground-signal-ground-signal-ground (GSGSG) configuration. The photomicrograph of these types of coils can be found in Figure 3.9.

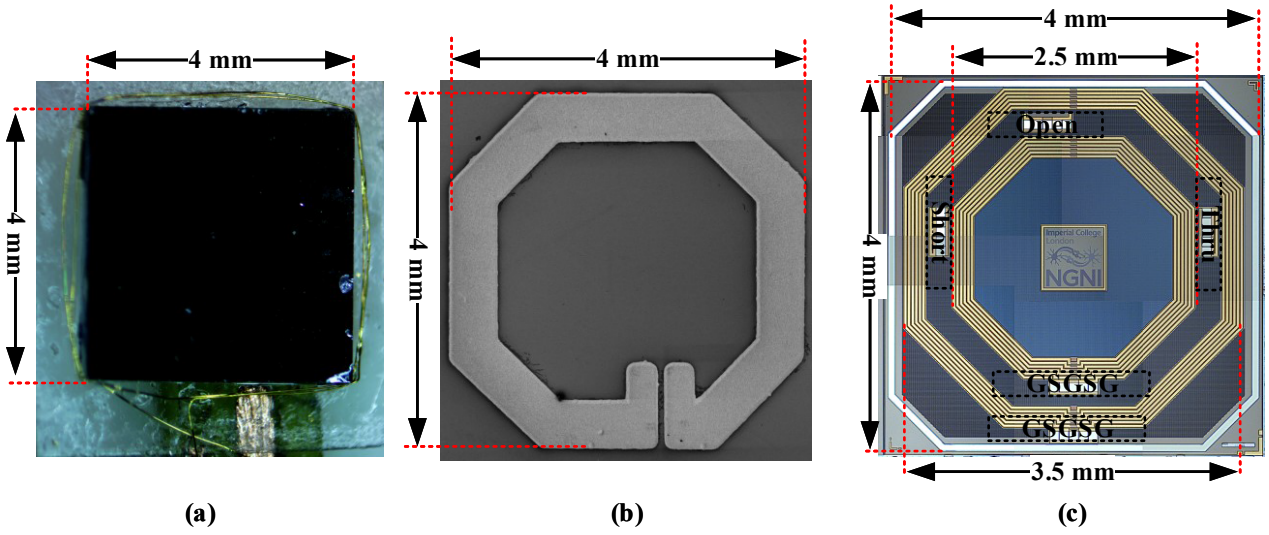


Figure 3.9: Fabricated (a) around-CMOS; (b) above-CMOS; and (c) in-CMOS coils.

3.4 Results

Three types of coils are measured in air and in biological environments to reveal offset of electrical characteristics. Also, the measured results are compared with analytical and simulated

results to verify models we presented in previous sections. The measured PTE of 2-coil link with three types of Rx coils provide guidelines for Rx coil selection.

3.4.1 Measurement Setup

A. In air measurement setup

The around-CMOS measurements are measured using a vector network analyser and interconnection T-shaped PCB with SMA connector. Two terminals of the around-CMOS coil have been bonded to pads on the PCB and connected to a 3.5 mm SMA connector. Parasitic inductance and capacitance from interconnection structures are usually greater than the inherent ones of the around-CMOS coil. Thus, the open-short de-embedding technique based on [38, 43] is necessary to remove parasitics. The parasitic capacitance is removed by subtracting the imaginary parts of Z parameters in open-circuit PCB and interconnection track resistance is eliminated by subtracting the real parts of Z parameters in short-circuit PCB.

The above-CMOS and in-CMOS coils are measured by using Model 40A RF probe (GSGSG 100 μm pitch, Picoprobe, FL, USA) and ACP350 RF probe (GS 350 μm pitch, Cascade Microtech, Oregon, USA), a probe station (Cascade Summit 9101, OR, USA) and E8361A network analyser (Agilent, CA), as shown in Figure 3.10(a). The short-open-load (SOL) de-embedding technique is applied to move reference plane from network analyser ports to probe tips. Then, open-through [97] de-embedding technique is adopted to remove the parasitics caused by measuring pads.

B. *Ex vivo* measurement setup

In order to observe the variation in electrical characteristics of the 2-coil inductive link with the presence of biological tissue, we selected two *ex vivo* measurement conditions. They are set in similar biological environments with different Tx - Rx distances d_{Tx-Rx}. One is lamb rib with 12 mm thickness to mimic the human head model and the other one is pig head with

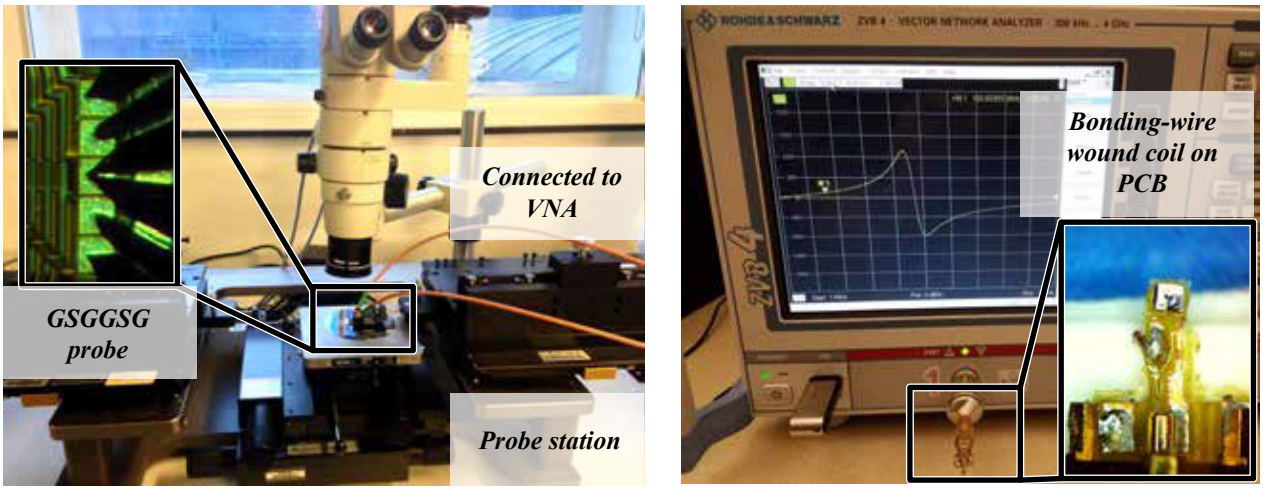


Figure 3.10: In air measurement setups for: (a) the planar (*in-CMOS* and *above-CMOS*) coils; and (b) the wirewould (*around-CMOS*) coil.

d_{Tx-Rx} at 28 mm. The thickness of the pig's skull is 20 mm, which is almost three times thicker than human. Figure 3.11 shows the experimental setup for both *ex vivo* measurements. Since Tx and Rx coils need to be connected to the vector network analyser (VNA) for S-parameter measurements, both coils connect to matching networks to eliminate the impedance mismatch between the coil terminals and the standard 50 Ω VNA ports. The Rx coil connects to the frequency tune capacitor and the SMA port on a 2 cm×5 cm PCB through bonding wires. PCB based Tx coil is also tuned to the same frequency to ensure the requirements of resonant based inductive link are met.

3.4.2 mm-scale Rx coils

Three types of coils are measured in two different environments (in air and around biological tissues). All calculated, simulated and measured inductance, resistance, and Q factor within 10 MHz to 1 GHz frequency range are presented and analysed in Figs. 3.12 and Figs. 3.13.

In the low frequency range (< 500 MHz), the calculated, simulated and measured results of three coils are identical. Inductance is easier to predict in calculation and simulation than resistance, since the inductance remains constant when measuring frequency is far from self resonant frequency (SRF). There are obvious differences between measured and calculated/simulated

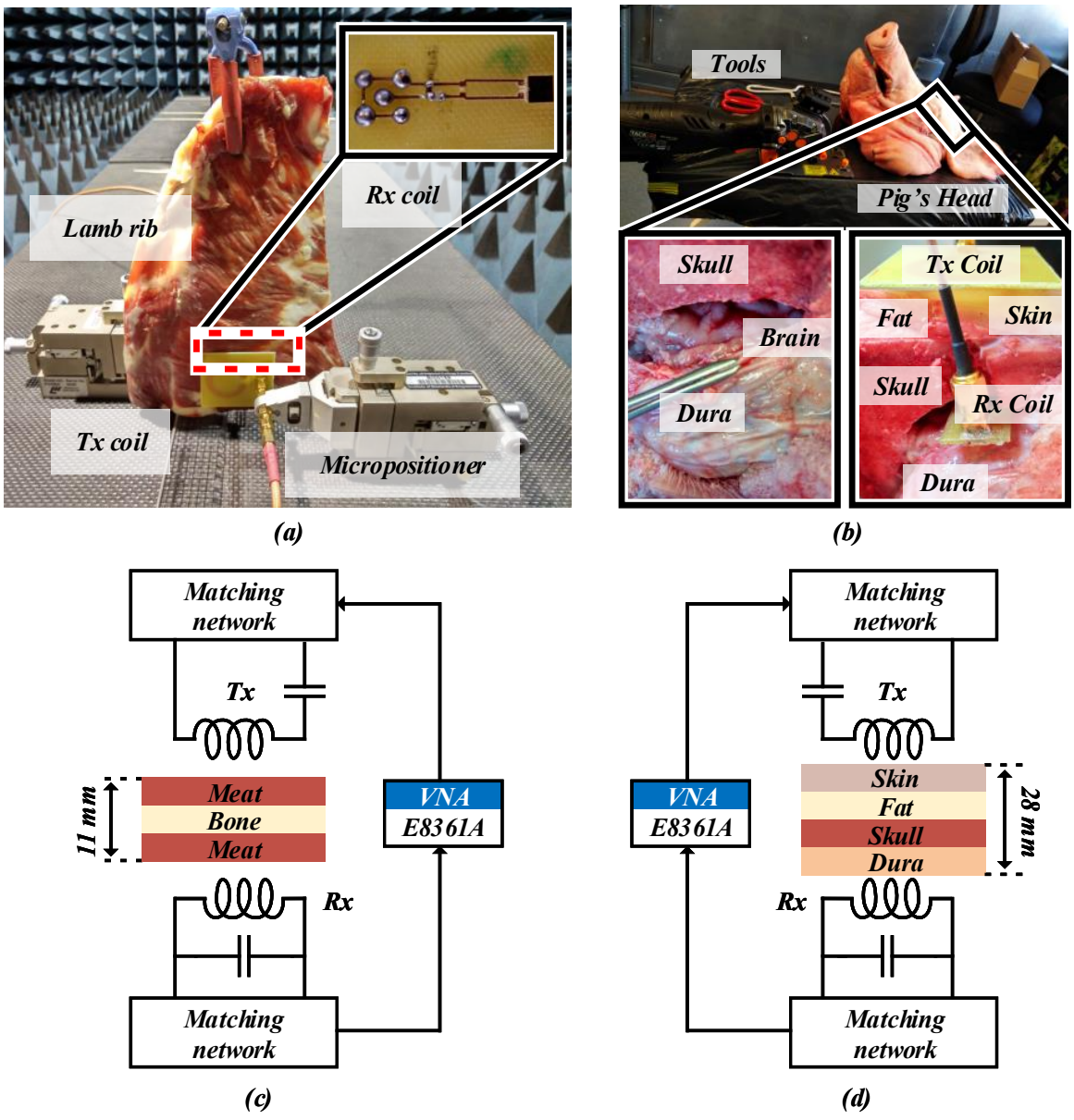


Figure 3.11: *Ex vivo* measurement setups: (a) 2-coil links measured with lamb rib and (b) schematic of measurement setups.

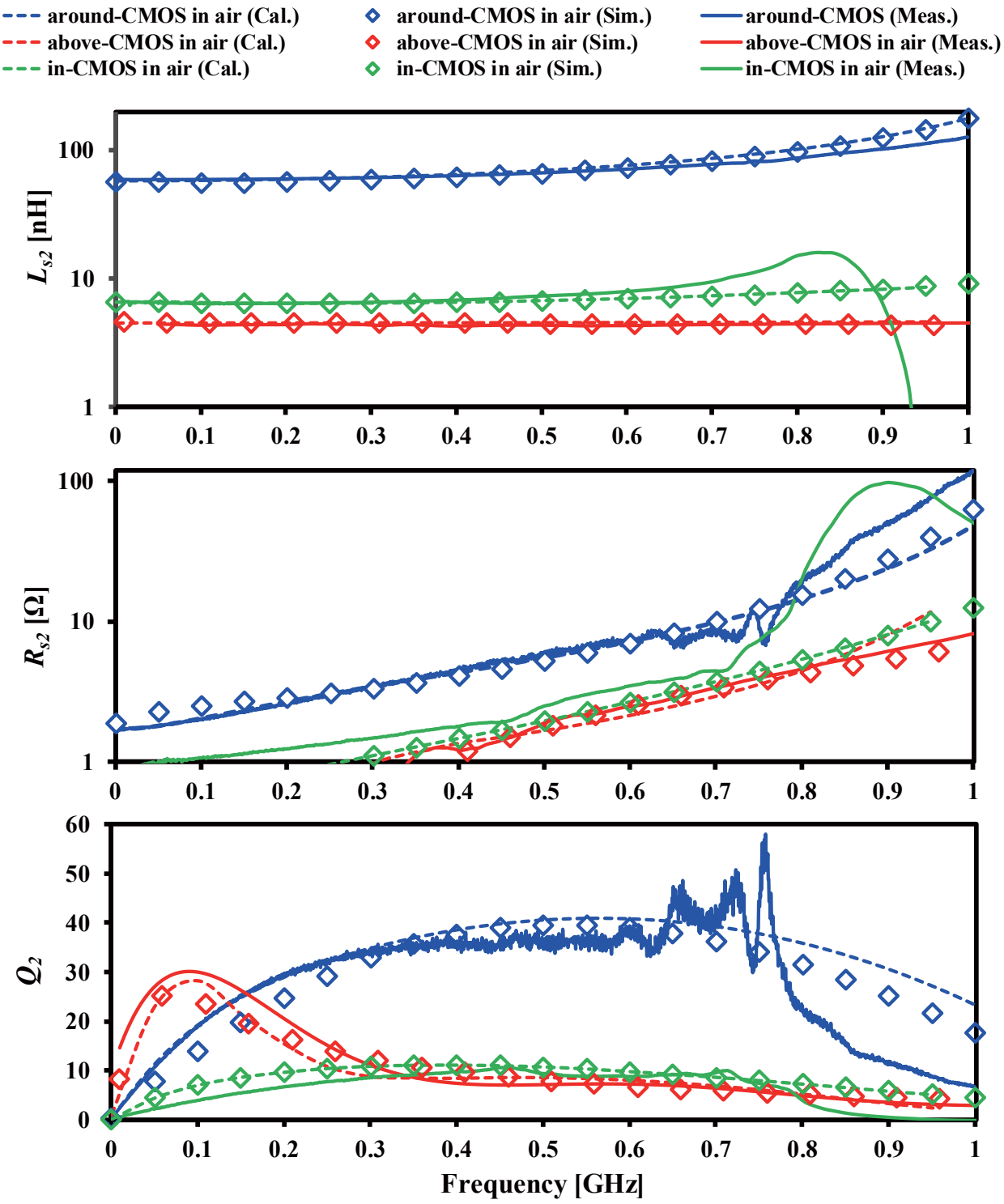


Figure 3.12: In air measured around-CMOS (blue), above-CMOS (red), and in-CMOS (green) coils compared with simulated and calculated results showing: (a) inductance; (b) resistance; (c) Q factor.

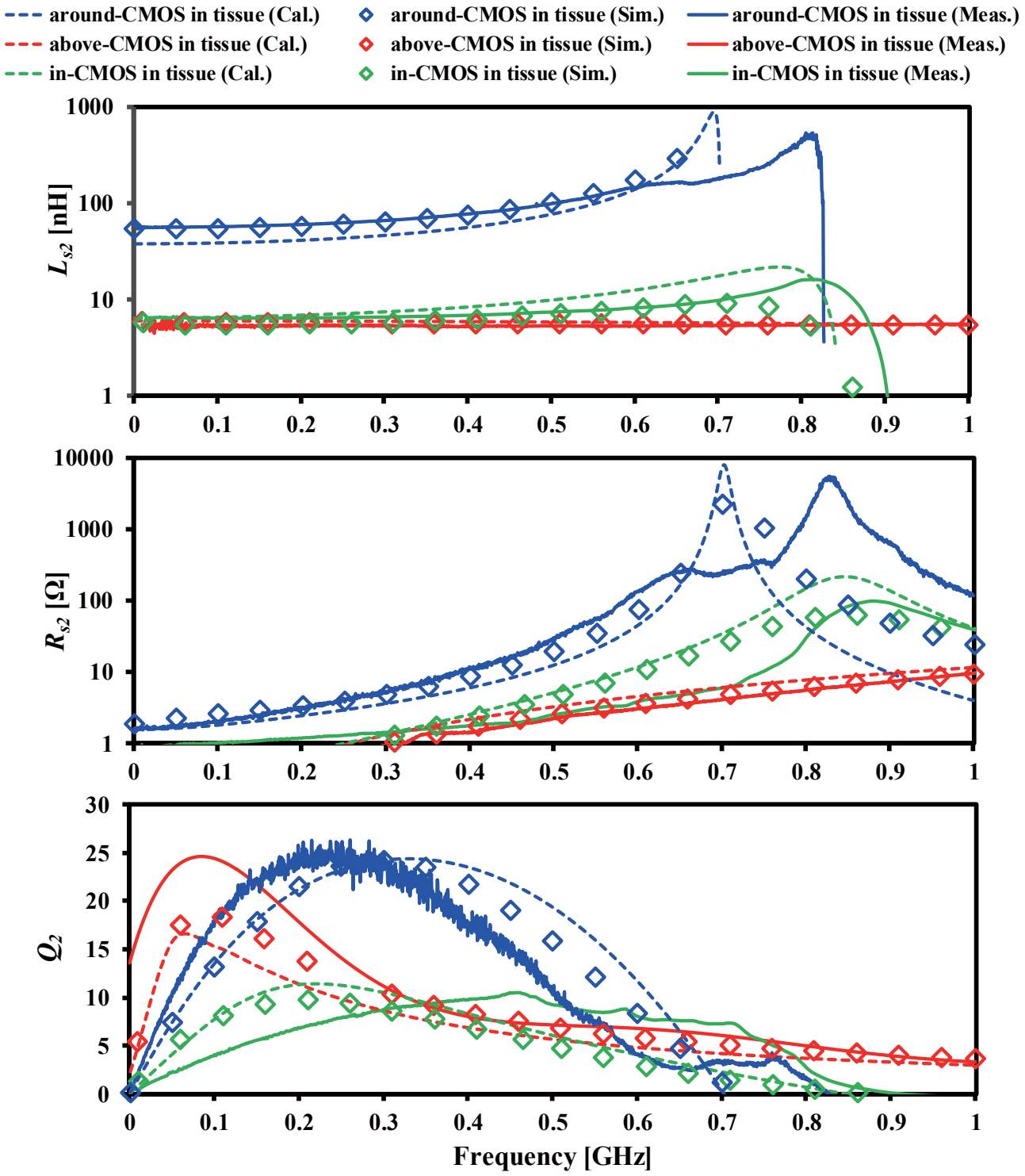


Figure 3.13: *Ex vivo* measured *around-CMOS* wirewound (blue), *above-CMOS* micro-fabricated (red), and *in-CMOS* integrated (green) coils compared with simulated and calculated results showing: (a) inductance; (b) resistance; (c) Q factor.

resistance. This deviation is caused by inaccurate estimation of skin effects and proximity effects at high frequency, resulting in drastic variations of parasitic resistance.

By comparing Figures 3.12 and 3.13, the apparent variation in electrical characteristics caused by the Rx coil approaching to biological tissues can be summarised as follows.

• Their SRFs decrease from approximately 1 GHz to 700-800 MHz when Rx coils approach to biological tissues. Since SRF is inversely proportional to the square root of capacitance $SRF \propto 1/\sqrt{C}$, surrounding biological tissues introduced extra parallel parasitic capacitance C_{p2}.

• Q factors of all coils have a noticeable decline with the presence of biological tissues. This is due to increasing resistance R_{p2} in the surrounding tissue environment and slight decrease of inductance L_{s2}.

The comprehensive analysis on EM properties of around-CMOS, above-CMOS, and in-CMOS coils are successively presented in the following subsections.

A. Around-CMOS coil

Results of HFSS simulation and analytical calculation in air match well with measured results, when operating frequency is less than 650 MHz. The measured Q factor has an apparent fluctuation from 650 MHz to 750 MHz. It is caused by deviations between the measured R_{s2} and simulated values because the resonant frequency PCB interconnected structure falls into this frequency range.

Measured results in tissue have different resonant frequencies comparing to simulated and calculated results. This deviation is caused by ideal homogeneous biological tissue models adopted in the simulation/calculation. However, it is worth noting that the trend of measured Q factors and the maximum values are similar to simulated/calculated results. By comparing the measurements in air and biological tissues, the maximum Q_2 decreases from 37.5 at 555 MHz

in air to 26.23 at 283 MHz in *ex vivo*. Also, the inductance has a slight drop to 69.5 nH from 80.3 nH in air.

B. Above-CMOS coil

Measured inductance of the above-CMOS coil in Figure 3.12 and Figure 3.13 show a good correlation between the simulated and calculated results. The measured Q factor in both air and tissue is higher than simulated/calculated values at the low-frequency range (< 300 MHz). This inaccurate measurement occurs when the serial resistance is close to the bottom limits of PNA. The measured resistance R_{s2} is 0.08 Ω @ 90.4 MHz in air and 0.13 Ω @85.0 MHz in tissue. Their sheet resistances are equal to $\sim$1.93 mΩ/sq in air and $\sim$3.14 mΩ/sq in tissue, where sheet resistance R_{st} refers to the ratio between resistivity ρ and sheet thickness t, regardless of the length or width ($R_{st} = \rho/t$).

The measured inductance L_{s2} has slightly dropped from 4.37 nH to 5.42 nH when the above-CMOS coil is close to the surface of lamb rib. The highest Q factor (30.09 @ 90.4 MHz) in air has slightly decreased to 24.61 @ 85.0 MHz. Similarly, as to the around-CMOS coil, the deviations of Q factor in tissue are more obvious than that in air, because of the unexpected inhomogeneous electromagnetic properties of lamb rib. The parasitic parameters C_{p2} and R_{p2} in the analytical models are adopted from [106], where they were using beef to mimic biological tissue environments. These differences cause the apparent deviations among measured, simulated and calculated curves.

C. In-CMOS coil

For the in-CMOS coil, the measured SRF has a significant discrepancy with simulated and calculated values. The SRF in simulation and analytical models cannot consider all structural details such as metal fills and interconnected structures. So ignored tiny structures generates parasitic capacitance, then leads to lower measured SRF (940 MHz) than the simulated value(1.35 GHz). There is no apparent change of the highest Q factor ($\approx$ 10.5) in air, though

the operating frequency has dropped from 509 MHz to 450.3z MHz.

3.4.3 Two-Coil Inductive Link

The two coil link is employed to compare the three different types of Rx coils fairly[1]. All Rx coils are measured and find their maximum Q factor at different operating frequencies. After following the optimisation process introduced in subsection 3.3.2, the Tx coils are individually optimised and tuned to desired frequencies. All Tx coils are single-turn devices and fabricated on 70 μm copper foil or RO4000 hydrocarbon ceramic laminated PCB with 1 oz copper (Rogers Communications Inc., Canada). All geometrics of these 2-coil link are summarised in Table 3.3. In order to investigate the PTE of each 2-coil links, the two-port S-parameters are measured from primary and secondary terminals by VNA. PTE is calculated based on the measured S-parameters according to the equation below [120].

$$PTE = \frac{|S_{21}|^2 R_L}{50} \times 100\% \tag{3.26}$$

where S_{21} represents the received power at the Rx coil relative to the input power at the Tx coil. The highest PTE is found in around-CMOS Rx coil system at 25.84% @ 497.3 MHz, then 24.12% @114.7 MHz, and 7.81% @423.2MHz for above-CMOS and in-CMOS coils' system, when Tx and Rx coils are perfectly aligned at the fixed 12 mm distance. All 2-coil links face the severe deterioration of PTE within biological environments, and also have a significant reduction of operating frequencies. The PTE through tissue medium has dropped to 3.05%, 2.09%, and 1.64% at operating frequencies, 318.8 MHz, 82.9 MHz, and 355.8 MHz for around-CMOS, above-CMOS and in-CMOS coils.

3.5 Discussion

The comparison between different types of mm-scale Rx coils is summarised in Table 3.5.

[1]The author acknowledges that multi-coil links can achieve higher PTE than that of two-coil links. The design of the multi-coil link to improve PTE will be introduced in Chapter 4.

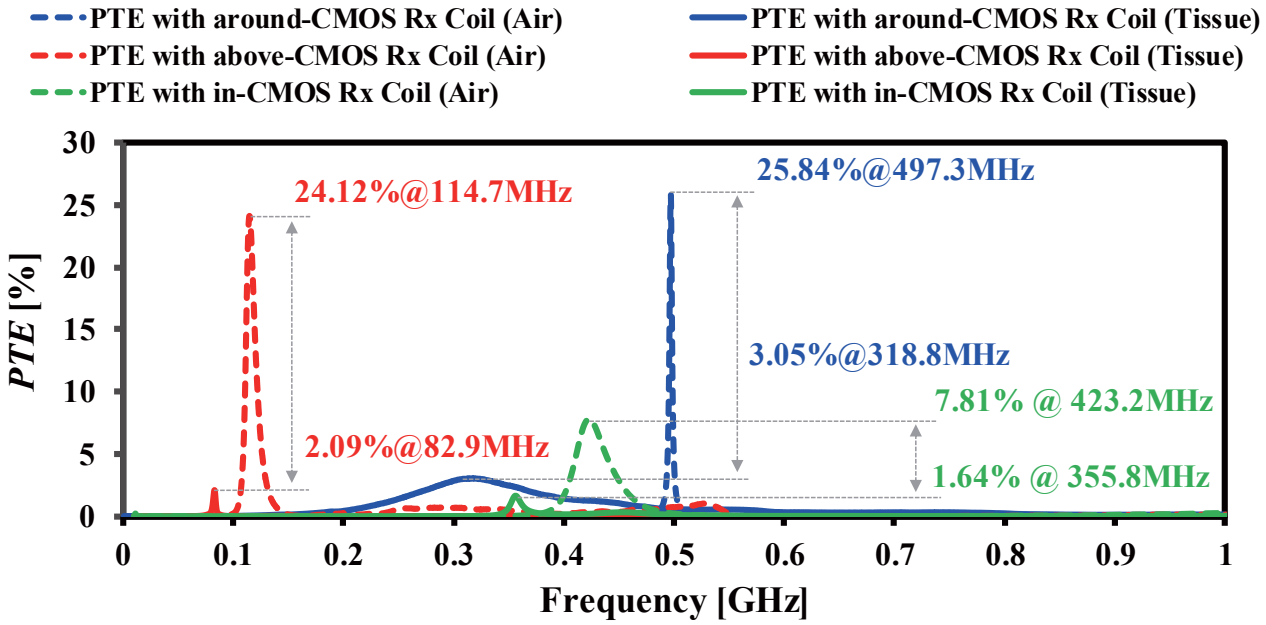


Figure 3.14: Measured PTE of 2-coil inductive links to deliver power to the 4 mm×4 mm around-CMOS, above-CMOS, and in-CMOS Rx coils.

Table 3.4: Comparison between around-CMOS, above-CMOS, and in-CMOS coils.

Parameters	[Unit]	[100]	[58]	This work	[118]	[119]	This work	[50]	This work
Type	-	*around-CMOS*	*around-CMOS*	*around-CMOS*	*above-CMOS*	*above-CMOS*	*above-CMOS*	*in-CMOS*	*in-CMOS*
Diameter (D_{o2})	[mm]	1	1	4	0.3	1.53×1.03	4	2	4
Trace width (w_2)	[μm]	25	25	25	20	55-65	250	140	175
Trace spacing (s_2)	[μm]	25	-	-	30	100	-	40	-
Trace thickness (t_2)	[μm]	25	25	25	10	8-12	25	-	4
Number of turns (N_2)	-	5	7	2	4	1.5	1	4	1
Inductance (L_{s2})	[nH]	40	94	60.7	3.19	1.14	5.43	70	7.11
Resistance (R_{s2})	[Ω]	2.2	-	3.12	3.32	-	0.12	-	1.92
Q factor (Q_2)	-	50	22	26.23	25.7	55	24.61	11.05	10.5
Frequency@Q_{max}	[MHz]	400	130	283	13700	6750	85	100	450.3
SRF	[GHz]	-	-	-	14	21	1.9	0.22	0.9
PTE	[%]	-	9.13 (3-coil)	3.05	-	-	2.09	-	1.64
Frequency@PTE_{max}	[MHz]	-	275	318.8	-	-	82.9	-	355.8
Medium	-	Air	Tissue	Tissue	Air	Air	Tissue	Air	Tissue

The around-CMOS coil has the highest Q factor and PTE, but is facing the variation of electrical properties in the manufacturing process, particularly in the current manual fabrication process. However, an advanced process proposed in [100] by using a high-end fully automated wire-bonder to control the pitch and shape of around-CMOS coil well results in a reduction of process variations. The fatal defect of this type of coil is to increase the risk of hermetic failure and unstable mechanical structure due to the fragile bonding wire wound around package without any protection.

Above-CMOS coil has modest electromagnetic property and acceptable other characteristics in terms of fabrication, hermeticity and mechanical stability. Thus, it is suitable for system

Table 3.5: Comparison between different types of mm-scale Rx coils.

Parameter/Type	Around-CMOS coil	Above-CMOS coil	In-CMOS coil
Manufacturability	Low	Medium	High
Repeatability	Low	Medium	High
Hermeticity	Low	Medium	High
Mechanical stability	Low	Medium	High
Electrical property	High	Medium	Low

integration. The potential improvements for the above-CMOS coil are reducing the substrate loss by etching silicon substrate to form a suspended coil [104, 118] or replacing the silicon substrate with polymer to enhance the Q factor [119], at the expense of increased fabrication complexity. Coils' SRF is determined by the distance from metal tracks to the silicon substrate and relative permittivity of dielectric materials. Based on the measured results, the SRF of the above-CMOS coil is below 100 MHz, which is significantly lower than that of other coils. The thickness of the silicon dioxide layer between the above-CMOS coil and the silicon substrate is only 5 nm, as illustrated in Figure 3.15. Thus, the increment of C_{ox} leads to a decrease in SRF.

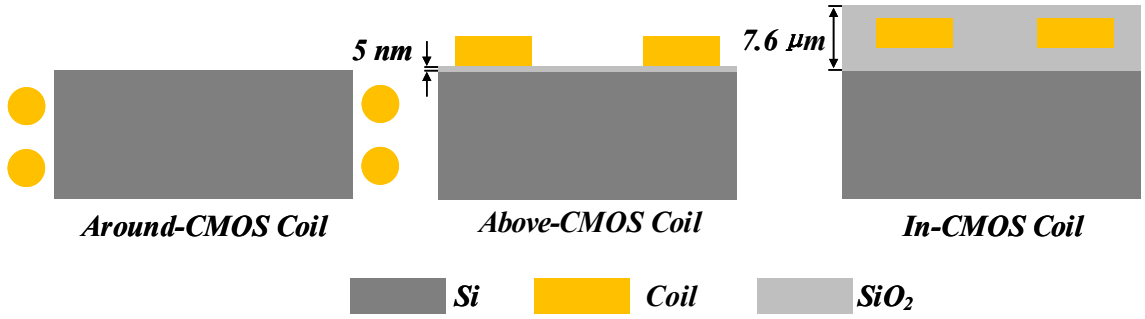


Figure 3.15: Cross-section of Around-CMOS, Above-CMOS, and In-CMOS coils.

In-CMOS coils take advantages of standard CMOS processes to have a well-controlled repeatability, mechanical stability and cost-effectiveness. However, it has the lowest Q factor due to thin metal layers. The patterned ground shielding technique [117] can slightly improve Q factor at the expense of electromagnetic transparency.

Electrical properties, fabrication methods, hermeticity, and mechanical stability of three types of Rx coils are compared in Table 3.5 to provide guidelines for the mm-scale implantable Rx coil selection. The next-generation distributed mm-sized neural probes are embedded inductively

coupled power coils [95, 122, 123]. Three examples in Figure 3.16 shows three different schemes of around-CMOS, above-CMOS, and in-CMOS coils' system integration. Free-floating wireless implantable neural recording system (FF-WINeR) integrates an around-CMOS coil outside silicon substrate with a polymer packing [122]. Empowering next-generation implantable neural interfaces (ENGINI) contain an above-CMOS coil in the hermetic silicon cavity [95, 98]. Encapsulated neural interfacing acquisition chip (ENIAC) has a well-designed in-CMOS coil [123].

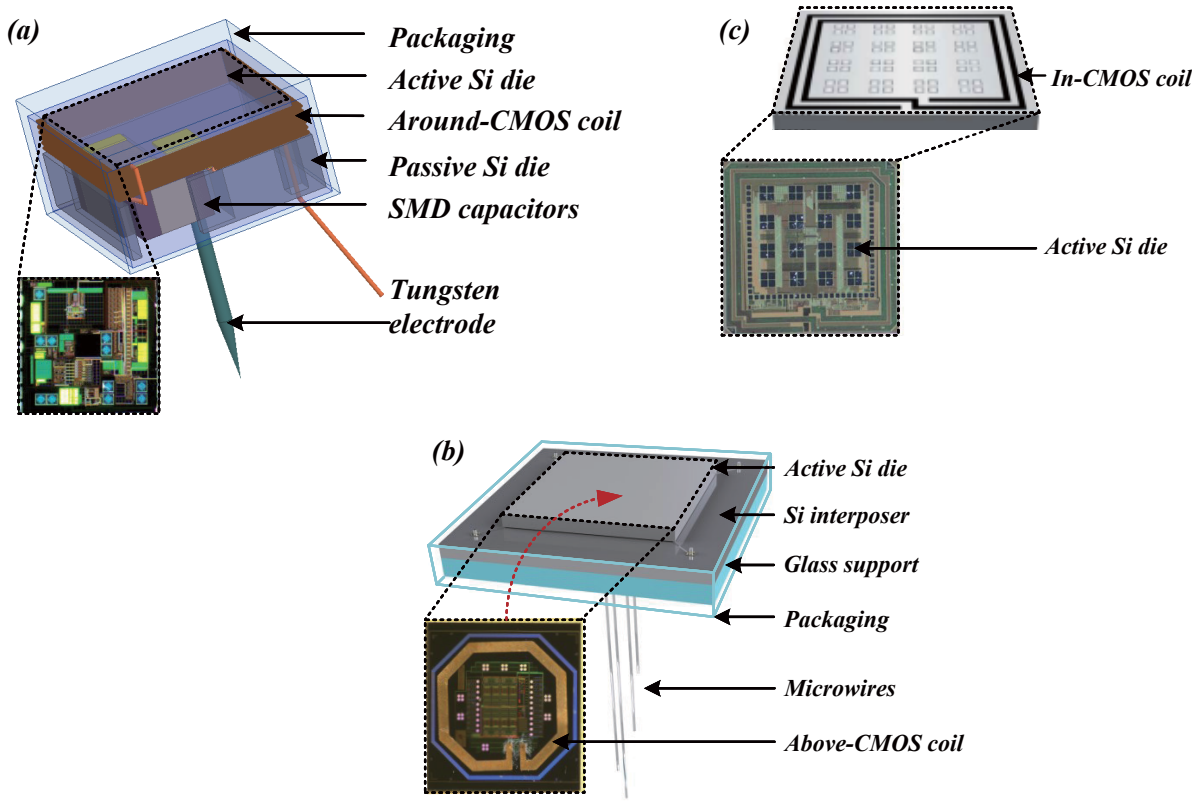


Figure 3.16: Different concepts for probe integration with mm-scale coils: (a) Free-floating wireless implantable neural recording system (FF-WINeR) with an around-CMOS coil [122]; (b) Empowering next generation implantable neural interface (ENGINI) with an above-CMOS coil [95]; (c) Encapsulated neural interfacing acquisition chip (ENIAC) with an in-CMOS coil [123].

3.6 Summary

This chapter has investigated three different types of mm-scale Rx coils: around-CMOS, above-CMOS, and in-CMOS. Analytical and simulation models of the three Rx coils are verified through measurement, which provides a reliable basis for the further optimisation. The electri-

cal characteristics variation of these three Rx coils are demonstrated and analysed when they approach biological tissues. Furthermore, comparison between electrical properties, fabrication methods, hermeticity, and mechanical stability of these three Rx coils are performed to provide a guide for mm-scale CMOS-compatible Rx coil selection.

The technical conclusions for the Rx implantable coils and the 2-coil inductive links in this chapter are summarised as follows three aspects.

- The above-CMOS coil is selected as the Rx implantable coil, instead of around-CMOS and In-CMOS coils, because of its modest electrical properties and stable mechanical structure.

- The 2-coil inductive links with the mm-scale Rx coils in the biological environment suffer from low PTE that is usually less than 10%. Thus, weakly coupled 2-coil inductive link scheme is not suitable for powering mm-scale implantable medical devices.

- Surrounding biological tissues have a significant influence on the electrical properties of Rx implantable coils. The PTE, Q factor and SRF of three coil types have apparent decline when they approach biological tissues.

Chapter 4

EM-Lens Enhanced WPT and Autonomous Power Management

"If you want to find the secrets of the universe, think in terms of energy, frequency and vibration."

– Nikola Tesla, 1856 - 1943

After selecting the above-CMOS coil for mm-scale bio-implants, the subsequent challenge is how to establish an inductive link through biological tissues with enhanced power transmission efficiency and extensive uniform power coverage for multiple distributed implants. Moreover, the objective is to realise robust power management at the Rx side in order to handle unpredictable received power regardless of positional and angular misalignments.

This chapter presents two key components in wireless power transfer systems: intermediate resonators (EM-lens) enhanced WPT and an autonomous power management scheme. The intermediate resonators between Tx and Rx coils can boost power transfer efficiency and extend power coverage. Thus, they are named as EM-lens in this chapter. The autonomous power management scheme can provide a self-regulated stable power supply voltages at the Rx side.

A portion of this work presented in this chapter has been published in [95, 124, 125].

This chapter starts with introducing our system-level concept by highlighting its inherent benefits. Secondly, EM-lens enhanced WPT prototype demonstrates its robustness against positional and angular misalignments or distance offsets. Thirdly, two passive AC-DC conversion topologies are compared through schematic analysis and chip measurements to choose the power-efficient cross-coupled rectifier for the co-design between inductive links and rectifiers. In the last section, the autonomous power management concept at the Rx side is verified by the chip measurement.

4.1 ENGINI System Overview

This section presents the concept of the entire Empowering Next Generation Implantable Neural Interfaces (ENGINI) project and the architecture of the wireless subsystems. ENGINI is an EPSRC supported research project initiated and led by my supervisor Dr Timothy G. Constandinou. The objective of this project is to explore and develop next-generation invasive neural interfaces from wireless, miniaturised, distributed, and autonomous perspectives. I am working with my colleagues to accomplish this ultimate goal. My research investigates reliable and efficient approaches to deliver power and exchange data wirelessly for mm-scale implants.

4.1.1 System Concept

The 2-tier strongly coupled inductive links has been proposed for the conceptual system of ENGINI [126] as shown in Figure 4.1. This is chosen instead of the previous weakly coupled 2-coil link. The principal objective of this wireless scheme is to deliver sufficient power for multiple neural implants regardless of their locations and orientations. The entire system is comprised of a 2-tier hierarchy of near-field inductively coupled links. The top tier establishes a transcutaneous link from a cm-scale scalp-worn primary coil to a subcutaneous resonator array. The EM-lens consists of this subcutaneous resonator array and epidural resonator array. The two arrays are wired through the skull to form a parallel-connected LC tank that eases EM

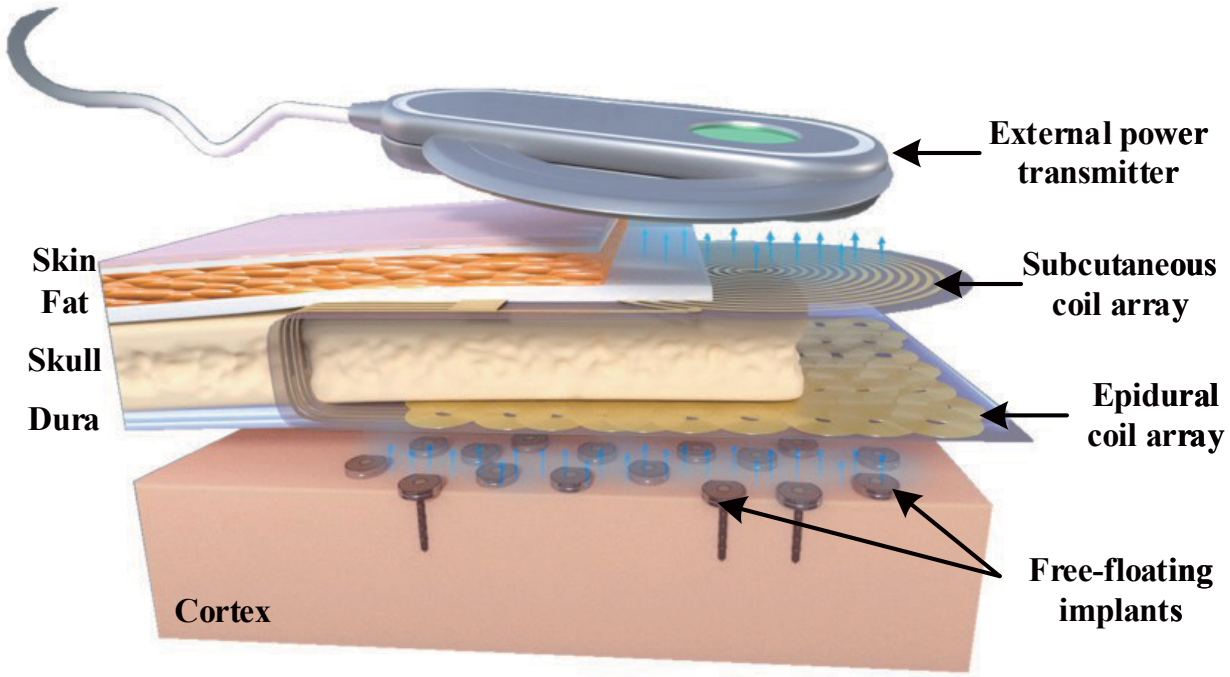


Figure 4.1: Proposed ENGINI system architecture of the 2-tier inductively coupled networks, in which subcutaneous/epidural coil array and removed skull portion can be replaced by a single customised cranioplasty.

transmission through bone. The transdural link in the bottom tier is inductively coupled to free-positioned subdural Rx coils on each distributed implant.

ENGINI scheme has two inherent benefits for wireless power transmission.

(1) Efficient power transfer: PTE is inversely proportional to the sixth power of distance d_{Tx-Rx} ($PTE \propto d_{Tx-Rx}^{-6}$). EM-lens shortens the distance between the transmitter and receiver from 12 mm to 5 mm by using wired connections through the skull. Thus, the PTE through inductive links has an opportunity for considerable improvement.

(2) Uniform power coverage: Power coverage is determined by the magnetic flux density B. The EM-lens evenly distributes the magnetic field density over a more extensive area than that of the Tx coil. Thus, Rx coils outside the Tx coverage can also obtain sufficient power.

Additionally, this scheme has two notable benefits from biological aspects.

(1) Reduced risk of infection: The dura mater can be sutured after the clinical implantation to maintain the blood-CSF barrier. This barrier selectively allows specific substances into

the brain and maintains normal brain homeostasis, thereby reducing the risk of infection.

(2) Increased implant longevity: The implant has no replaceable components like a battery. The relay coils are made up of passive components, thus reducing the stringent requirements for sealing. Consequently, there is a high chance of developing lifetime implants.

4.2 EM-Lens Enhanced Wireless Power Transfer

The schematic of the ENGINI inductive network, as shown in Figure 4.2, contains a serial Tx L_1C_1 tank, intermediate parallel-connected resonator arrays (L_{2i}, C_{2i}, L_{3j}, C_{3j}) and multiple freely-positioned parallel Rx L_4C_4 tank.

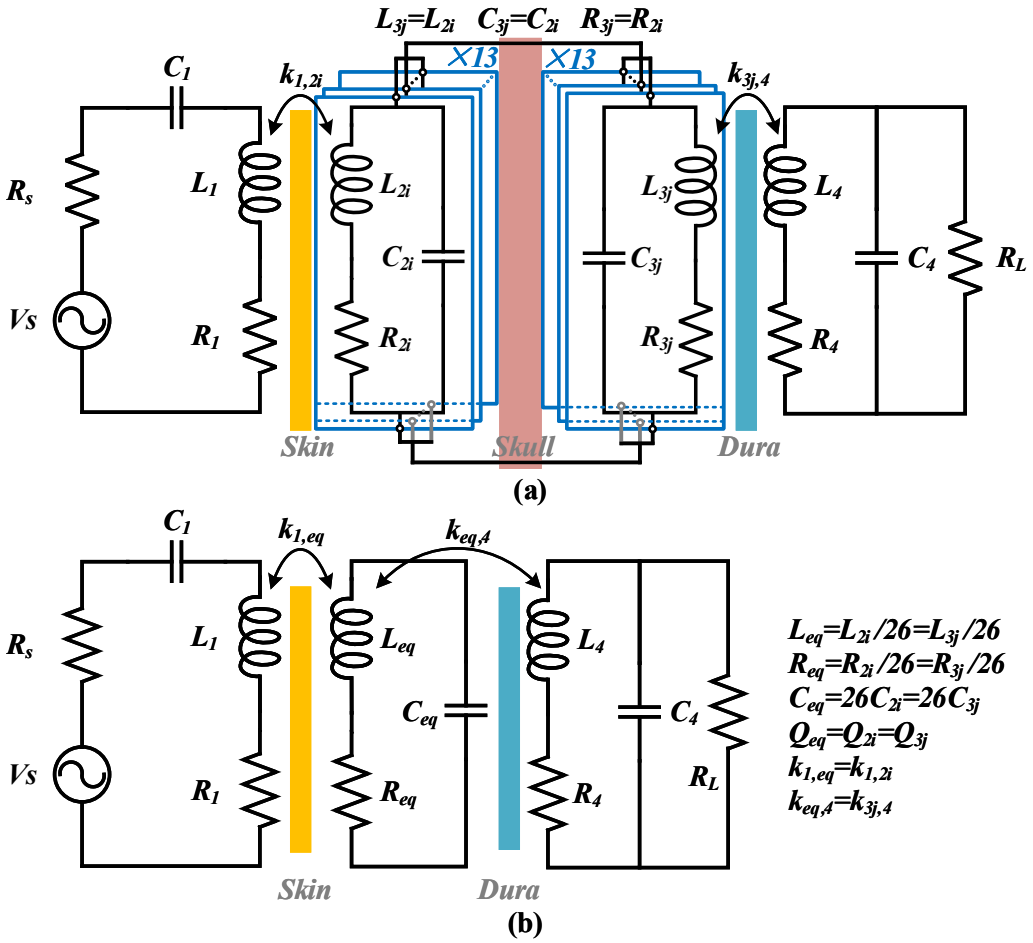


Figure 4.2: Equivalent circuit models for the: (a) proposed EM-lens enhanced WPT system; (b) simplified schematic for PTE derivation.

All LC tanks are tuned to the same frequency to establish strongly coupled magnetic resonances

in the inductive network. The equivalent circuit in Figure 4.2(a) is simplified into a 3-coil link model, since all the inductors and capacitors in intermediate arrays are identical under the assumption of negligible parasitic transcranial interconnections. The PTE of this 3-coil inductive link can be written as

$$\eta_{3\_coil} = \eta_{1,eq} \cdot \eta_{eq,4}, \tag{4.1}$$

where $\eta_{1,eq}$ and $\eta_{eq,4}$ can be found from [43]. For these cross-coupled inductive network, the total PTE of entire system is the sum of each 3-coil inductive link.

$$\eta_{total} = \sum_{i,j=1}^{n} (\eta_{1,2i} \cdot \eta_{3j,4}) \tag{4.2}$$

where the individual element of each cross-coupled 3-coil inductive link can be written as

$$\eta_{1,2i} = \frac{k_{1,2i}^2 Q_1 Q_{2i}}{1 + k_{1,2i}^2 Q_1 Q_{2i} + k_{3j,4}^2 Q_{3j} Q_{4L}}, \tag{4.3}$$

$$\eta_{3j,4} = \frac{k_{3j,4}^2 Q_{3j} Q_{4L}}{1 + k_{3j,4}^2 Q_{3j} Q_{4L}} \frac{Q_{4L}}{Q_L}. \tag{4.4}$$

where $k_{1,2i}$ and $k_{3j,4}$ are the coupling coefficient between the specific intermediate coil and Tx or Rx coil. Loaded Q factor for the Rx is defined as

$$Q_{4L} = \frac{Q_4 Q_L}{Q_4 + Q_L}, \tag{4.5}$$

in which

$$Q_L = \frac{R_L}{\omega L_4}. \tag{4.6}$$

According to equation 4.2, the enhancement of this scheme is caused by the superposition of all the 3-coil inductive links. The second transdural link is the bottleneck of the entire wireless power transmission system. It usually suffers from low PTE due to weak coupling with mm-scale Rx coils. To effectively evaluate the uniformity of power coverage, we define the power

distribution deviation (PDD) as

$$PDD = \frac{\max(\eta_{total}) - \min(\eta_{total})}{avg(\eta_{total})}. \tag{4.7}$$

4.2.1 Design Methodology

A. Simulation Setup

Similar to Section 3.3, the same six-layer head model is utilised and 2-tier inductive links are designed in HFSS simulation as shown in Figure 4.3. The Tx PCB coil and the Rx above-CMOS coil in tissue follow the previous design as shown in Table 3.3. The Rx above-CMOS coil is placed on a 4 mm×4 mm insulated silicon substrate covered with a 1 µm silicon dioxide (SiO_2) layer and 1 µm silicon nitride (Si_3N_4) layer to represent the CMOS passivation layer.

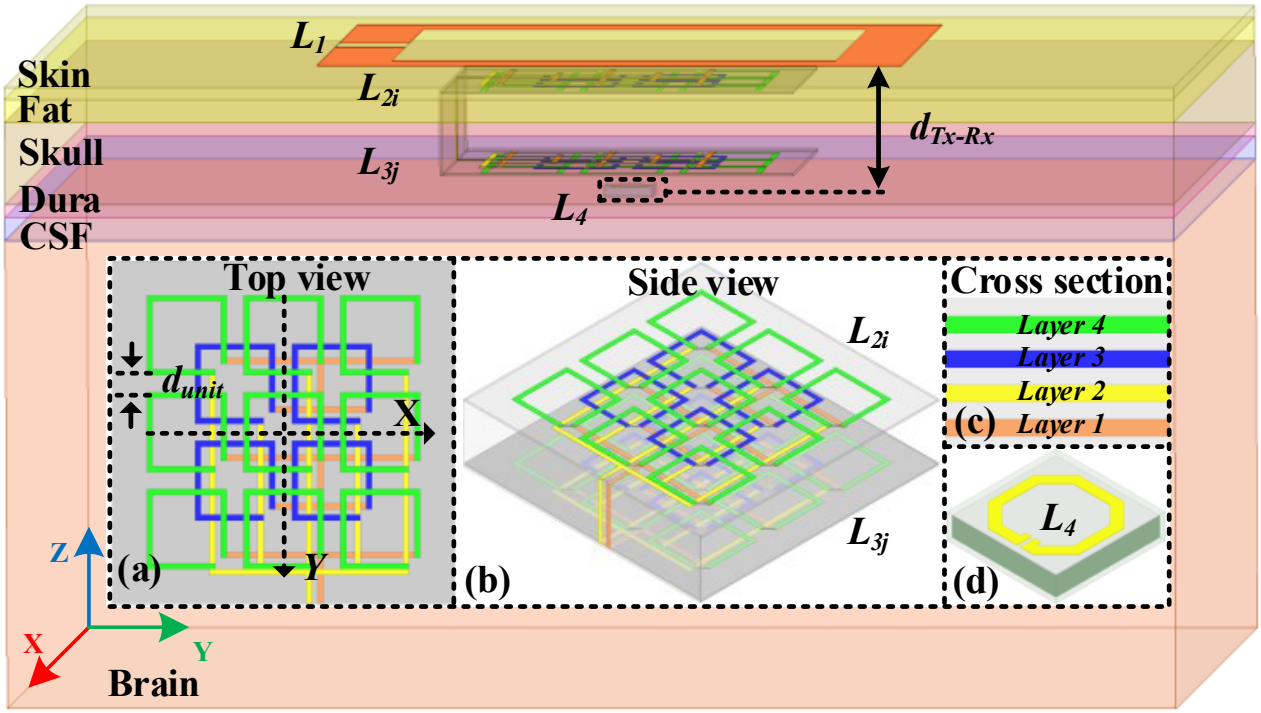


Figure 4.3: Cross-section of the human head model and relative positions of the external power transmitter L_1, free-positioned Rx coils L_4, subcutaneous L_{2i} and epidural coil arrays L_{3j}. Inset: (a) top view of 2-tier multiple coil arrays; (b) side view of wired interconnections; (c) cross-section of multiple coil array; (d) above-CMOS Rx coil.

The multiple coil arrays are shown in the inserts of Figure 4.3. The arrays have four metal

layers. Layer 4 and layer 3 are used to arrange identical arrays of coils L_{2i}, L_{3j}. All parallel interconnected structures are implemented on layer 2 and layer 1. The outer dimension of this intermediate coil relay is 20 mm×20 mm. The distance to Tx and Rx coils are 3 mm and 4 mm, respectively. There are nine coils on the top layer and four coils on layer 3. Each coil connects to a 3.6 pF lumped capacitor to tune their self-resonant frequencies (SRF) to 433 MHz.

B. Optimisation Strategy

The objective of this optimisation procedure is to achieve the maximum PTE and the minimum PDD within SAR constraint. The iterative optimisation process in Figure 4.4 starts from maximising the PTE ($\eta_{3j,4}$) for the critical 2-coil transdural link because it is the bottleneck of the entire WPT system. Next, the second stage performs transcutaneous link design to maximise the PTE ($\eta_{1,2i}$). The last stage focuses on the minimum PDD under the multiple coils coverage by adjusting the spacing of the overlapping multiple coil array. The detailed description of each optimisation stage is stated in the following subsections.

Stage 1: 2-coil Transdural Inductive Link Design

The design constraints of the Rx coil are similar to the 2-coil optimisation in Section 3.3.2. The load resistance R_L, trace thickness t_4,t_{3j} and outer diameter d_4 are 9 kΩ, 25 µm and 4 mm respectively. To achieve the highest Q factor and ensure their SRF is higher than the operating frequency, all coils in the 2-coil transdural inductive link are single-turn devices. In addition, single-turn implanted coils reduce eddy currents that form in the surrounding biological tissue, thereby minimising operating frequency variations after implantation.

The optimal operating frequency of the 2-coil transdural inductive link is selected as 433 MHz, based on the power delivered to the load (PDL), SAR constraints and industrial, scientific and medical (ISM) radio bands. The red straight line in Figure 4.5 indicates the SAR upper limit.

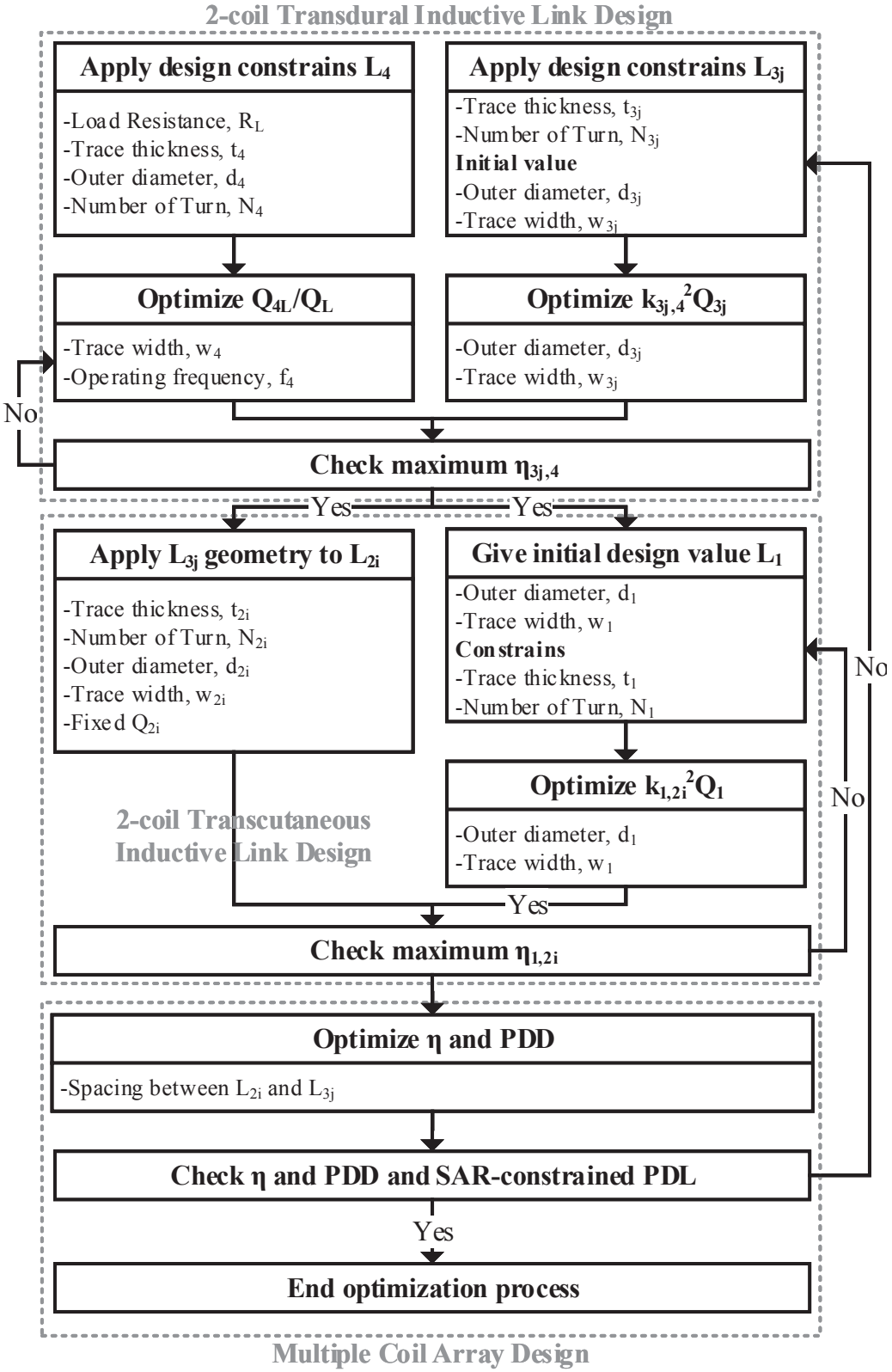


Figure 4.4: Optimisation process of 2-tier inductively coupled WPT system to achieve reasonable PTE and uniform power distribution.

SAR is defined in [26]

$$SAR = \frac{d}{dt}\left(\frac{dW}{dm}\right) = \frac{d}{dt}\left(\frac{dW}{\rho dV}\right) = \frac{\sigma|E|^2}{\rho} \quad W/kg, \tag{4.8}$$

where W is the PDL; m refers to the mass of tissue; ρ and V are the density and volume of the biological tissues, respectively; σ is the electrical conductivity of the tissue, and $|E|^2$ is the square of electronic fields, which is proportional to f_0^2. Thus, SAR is proportional to the square of operating frequency $SAR \propto f_0^2$. In the ISM band, the SAR values are $2.8567 \times 10^{-3} W/Kg, 1.2458 \times 10^{-2} W/Kg$, $2.8873 \times 10^{-2} W/Kg$, $1.0513 W/Kg$, and $2.004 W/Kg$ at 13.56 MHz, 27.12 MHz, 40.68 MHz, 433 MHz and 915 MHz, respectively. The SAR at 915 MHz exceeds the $1.6 W/Kg$ constraint. The maximum PDL of 406.79 μW is achieved at 433 MHz with a reasonable SAR of $1.0513 W/Kg$. Thus, the optimal operating frequency is selected as 433 MHz.

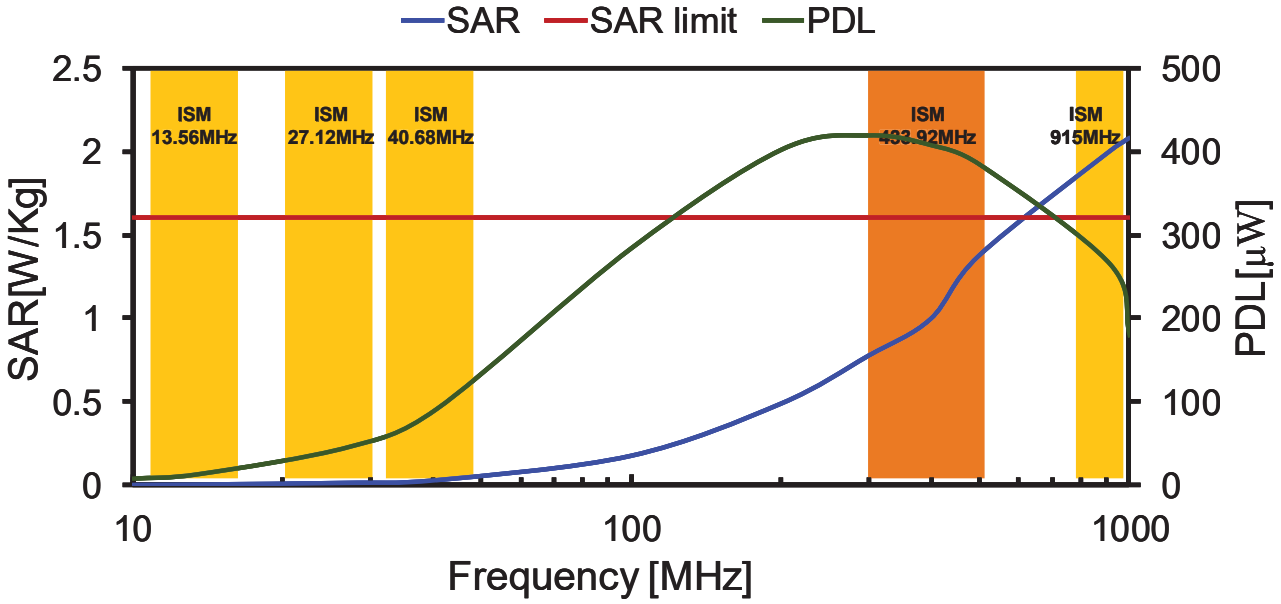


Figure 4.5: (a) The optimal operating frequency of ENGINI wireless power transfer system under SAR restriction; (b) measured reflection coefficient of Voyager active chip with above-chip Au coil. Optimal frequency under SAR restriction. Red line represents the $1g$ tissue limits at $1.6 W/Kg$ SAR. Yellow regions indicate ISM bands. Average SAR reaches $1.0513 W/Kg$ and PDL achieves $406.79 \mu W$ at $433.92 MHz$.

The PTE $\eta_{3j,4}$ is proportional to Q_{4L}/Q_L and $k_{3j,4}^2 Q_{3j}$. After the HFSS parametric sweep, the trace widths w_3 and outer diameter d_3 of the unit coil in the intermediate array are 500 μm and 7 mm, respectively. The simulated maximum PTE of the 2-coil transdural link achieves 19.2%

at 433 MHz.

Stage 2: 2-coil Transcutaneous Inductive Link Design

In this stage, the optimisation mainly focuses on the Tx coil, since the subcutaneous coil array L_{2i} is identical to the epidural coil arrays L_{3j} to guarantee the same SRF. Thus, the term $k_{1,2i}^2 Q_1$ needs to be maximised to enhance PTE. The outer diameter d_1 of 50 mm is selected to reinforce coupling coefficient $k_{1,2i}$ and the trace width w_1 of 12 mm is chosen to improve the Q factor Q_1. The simulated maximum PTE of this 2-coil transcutaneous link is 55.3% at 433 MHz.

Stage 3: Multiple Coil Array Design

The main objective of this stage is to determine the spacing among unit coils in arrays that extend the power coverage and maintain the PTE. The simulation results with various inter-unit spacings indicate a maximum 13.29% PTE and minimum 26.6% PDD across the 18 mm × 18 mm covered area, when the spacing $d_{unit} = 0.5$ mm. All specifications after optimisation are summarised in Table 4.1.

Table 4.1: Design geometry and electrical properties of the proposed two-tier inductively coupled WPT system.

Parameter/Type	[Unit]	L_1	L_{2i}	L_{3j}	L_4
Inductance (L_1-L_4)	[nH]	58.2	16.37	16.37	4.56
Resistance (R_1-R_4)	[Ω]	0.92	0.81	0.81	0.35
Quality factor (Q_1-Q_4)	-	172.1	55.0	55.0	35.8
Outer diameter (d_1-d_4)	[mm]	50	7	7	3.5
Trace width (w_1-w_4)	[mm]	12	0.5	0.5	0.25
Trace thickness (t_1-t_4)	[μm]	35	25	25	25
Number of turns (N_1-N_4)	-	1	1	1	1
Tx-Rx Distance (d_{Tx-Rx})	[mm]	12			
Operating frequency (f)	[MHz]	433			
PTE	[%]	13.29			

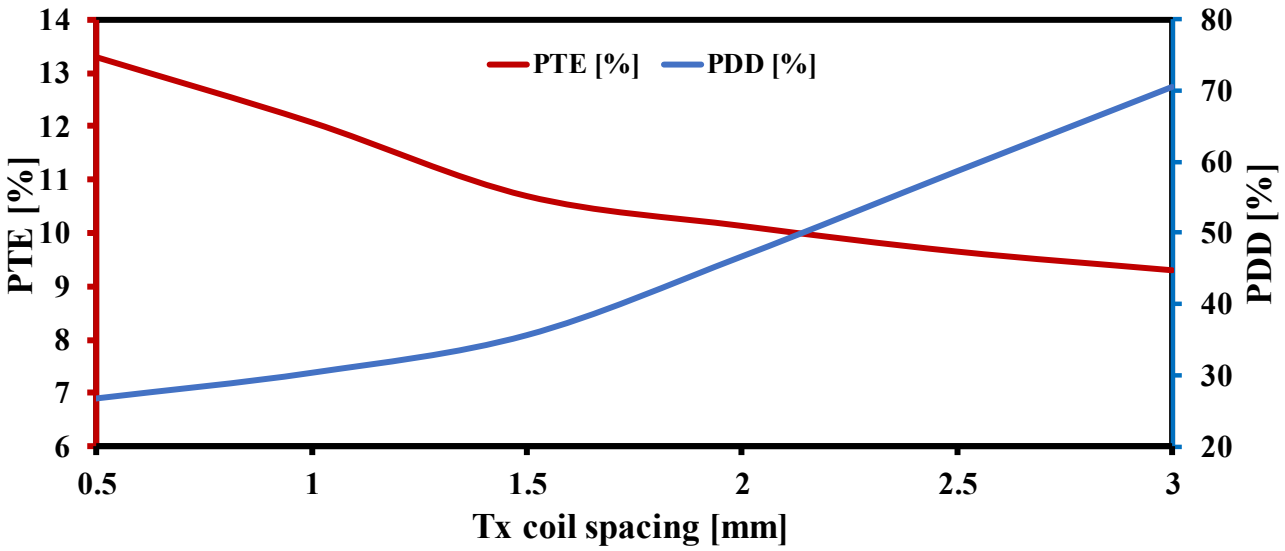


Figure 4.6: The maximum PTE and PDD across the 18 mm×18 mm covered area for different unit cell spacings d_{unit} within the multiple coil array.

4.2.2 HFSS Simulation

To demonstrate the improvement of the EM-lens, the 2-tier inductive link is compared with a conventional 2-coil link. The PDD is evaluated within 18 mm ×18 mm, when the Rx coil is parallel or perpendicular to the Tx coil. According to the simulated results in Figure 4.7, the PDD of the conventional 2-coil link (without EM-lens between Tx and Rx) varies significantly $> 95\%$, regardless of the Rx orientations.

The magnetic flux density of a single transmitter is not uniform, and hence the PTE is extremely sensitive to the positional and oriental misalignments. The PTE of the vertically placed Rx coil is less than 0.5% due to a weak magnetic fields through the surface of the Rx coil. With the EM-lens in the 2-tier inductive link, the PDD values at 0° and 90° angular alignment dramatically drop to 26.6% and 62.8% to guarantee sufficient power for the free-positioned Rx coils. Additionally, the apparent PTE improvement of the 2-tier inductive link is their maximum values at 13.29% for 0° angular alignment, or 3.32% even for 90° angular alignment.

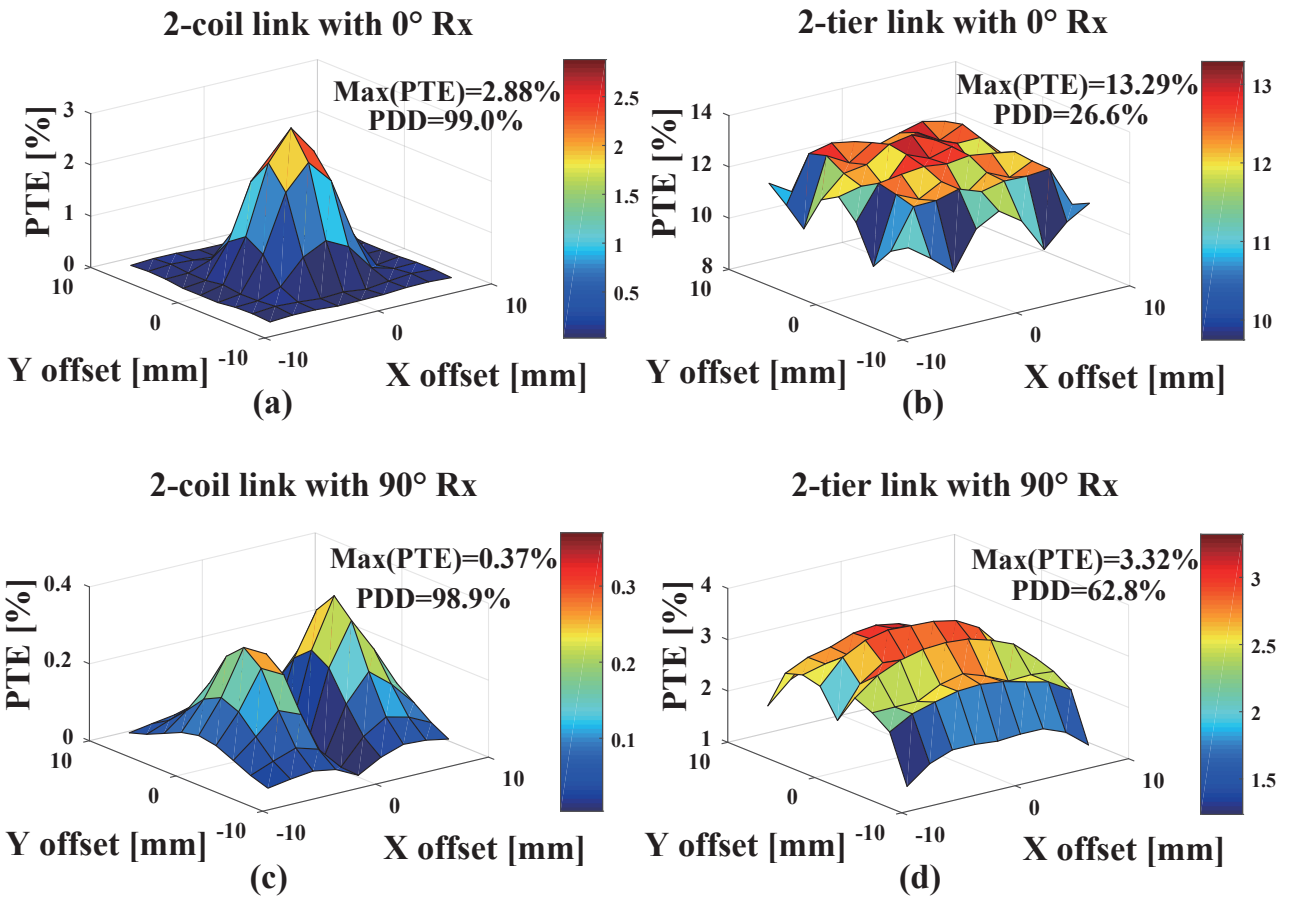


Figure 4.7: Comparison of simulated PTE and PDD between: (a) (c) conventional 2-coil link and (b) (d) the proposed 2-tier inductive link with a freely-positioned Rx coil at 0° and 90° angular alignment.

4.2.3 WPT Measurement Setup

Instead of evaluating the passive inductive link performance through S-parameters in Section 3.4.3, the active AC-DC conversion is implemented by a full-wave rectifier with a 10.89$k\Omega$ load resistance (3.3 V received voltage and 1 mW power) to measure the received voltage and demonstrate EM-lens enhanced power coverage. The experimental setup of the rectified voltage V_{rec} and power coverage evaluation is shown in Figure 4.8. Firstly, a power carrier with -10 dBm @ 433 MHz is generated by the RF signal generator SML03 (Rohde & Schwarz, Germany). Next, the power amplifier HMC1099 (Analog Devices, USA) boosts the power level to 10 dBm and transmits to the Tx LC tank through an impedance matching network. The PCB EM-lens that is coated in the biologically compatible PMMA to mimic artificial skulls is placed between the Tx and Rx. The Rx PCB contains an LC tank, load resistor, and passive full-

wave rectifier which is comprised of four Schottky diodes (1SS351, On Semiconductor, Phoenix, Arizona, United States). The rectified voltage is measured by a high impedance probe of LeCroy 7300A oscilloscope (Teledyne Technologies, USA) through Hirose U.FL RF connectors (Hirose Electric, Japan). The relative position between the Tx and Rx coils is precisely controlled by two RVX500 manual linear motion manipulators (Wentworth Laboratories, USA). The rectified voltage variations are measured against distances from 12.5 mm to 32.5 mm, and this 15 mm × 15 mm area is measured by this experimental setup with/without the EM-lens.

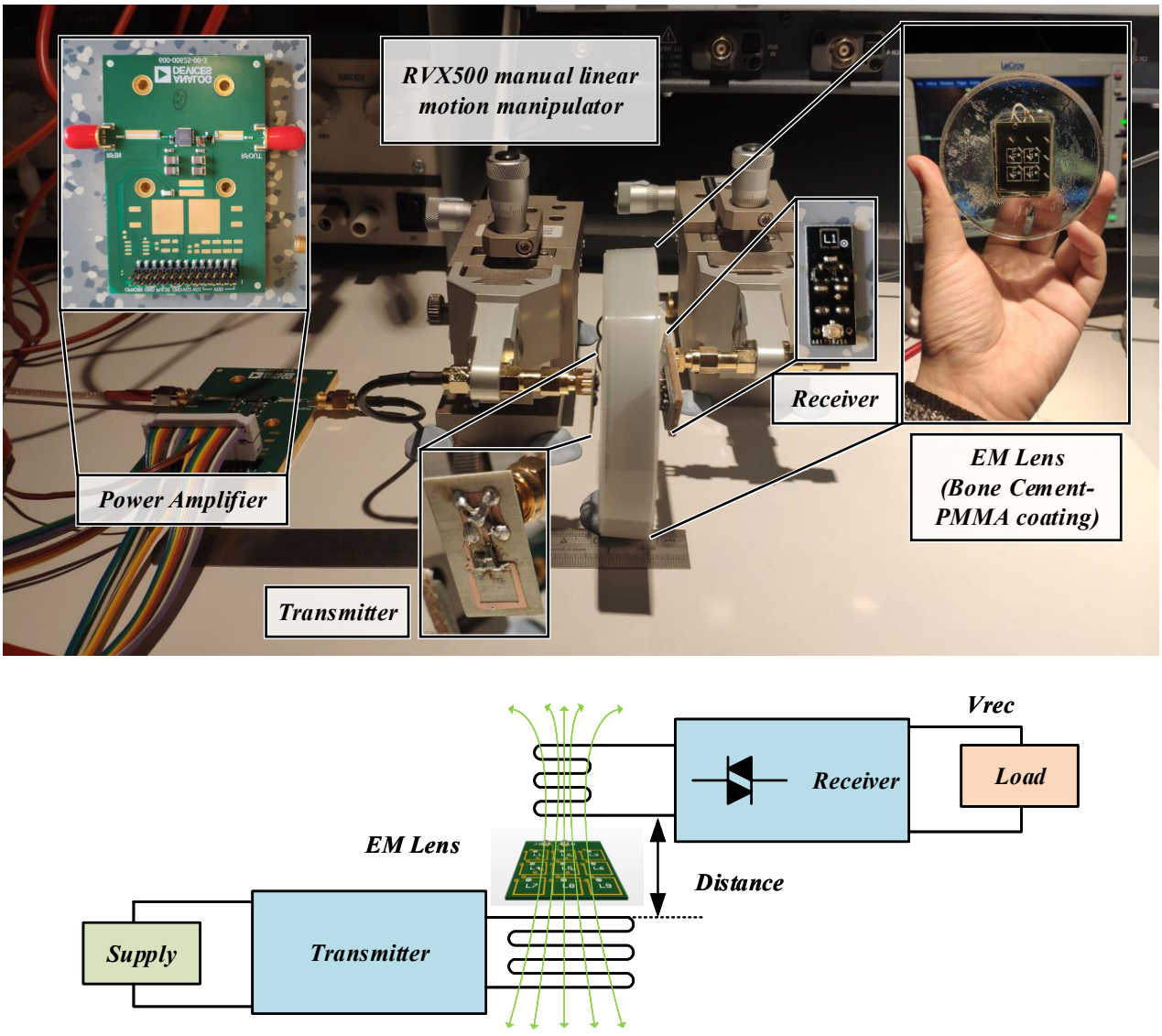


Figure 4.8: Measurement setup for EM-lens enhanced wireless power transfer system

4.2.4 WPT Measured Results

The prerequisite for maximising the received voltage of the WPT system is the consistent SRF of the Tx, Rx and EM-lens [127]. The serial capacitor C_1, parallel capacitors C_2i, C_3j and C_4 are used to tune all LC tanks at the same frequency. The measured return loss of all components, as shown in Figure 4.9, are -11.52 dB (Tx), -7.93 dB (EM-lens) and -10.95 dB (Rx) at 433 MHz. They are less than or close to -10 dB to indicate that most of the electromagnetic energy can be injected into each LC tank.

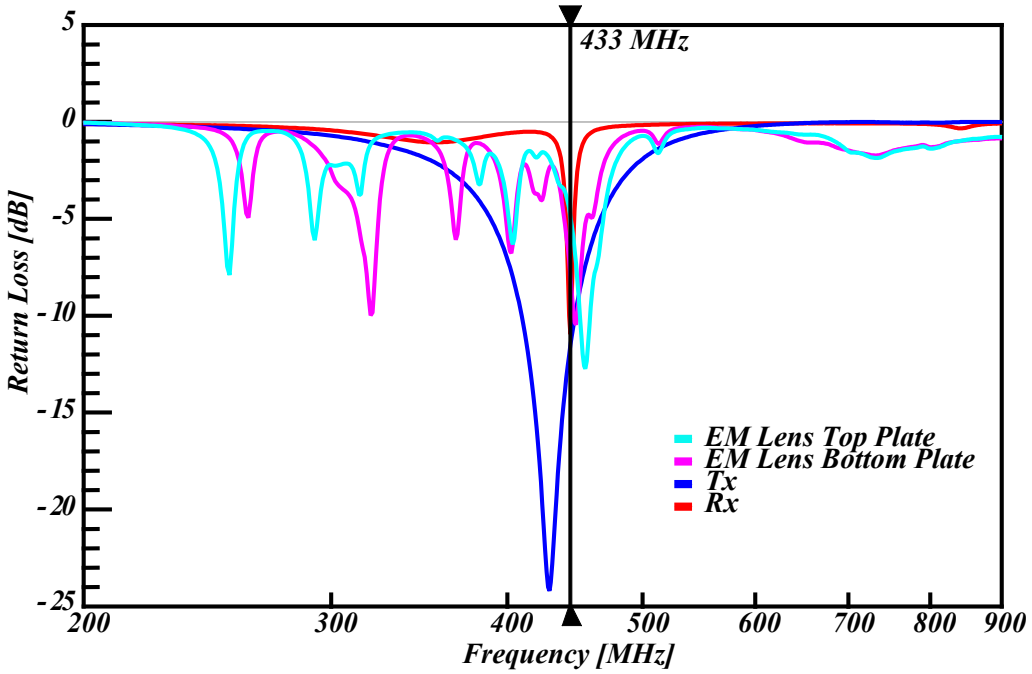


Figure 4.9: Measured results of return loss about Tx, EM-lens and Rx.

The measured rectified voltage over spatial variables is shown in Figure 4.10 and compared to with conventional 2-coil links. The benefits of the EM-lens enhanced WPT system are summarised as

- The EM-lens provides a notable enhancement on the rectified voltage when the distance between the Tx and Rx coils is less than 20 mm, as illustrated in Figure 4.10(a);

- The EM-lens spreads the power coverage four times from the previous 9 mm×5 mm (conventional 2-coil link) to the current 14 mm×13 mm (EM-lens enhanced link).

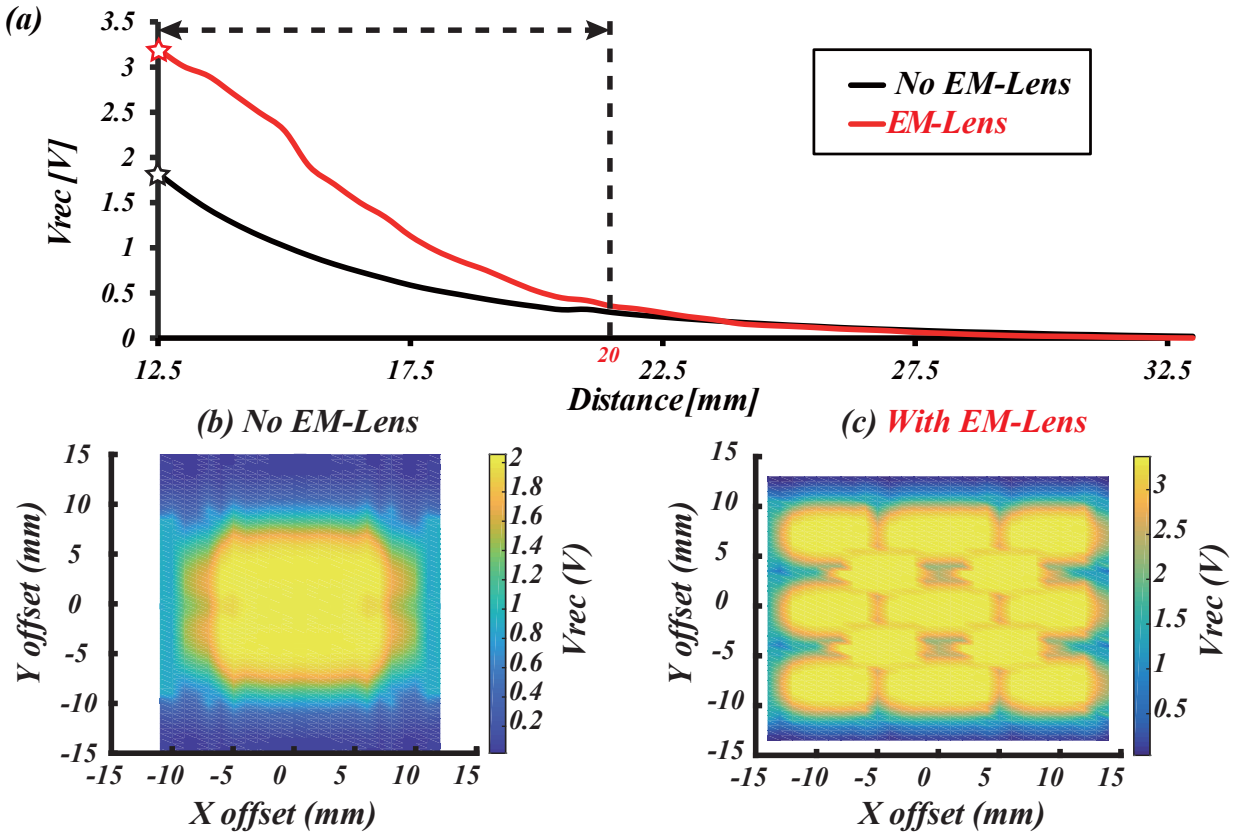


Figure 4.10: Measured results of EM-lens enhanced WPT: (a)Rectified voltage on Rx side with various distance, compared with air gap inductive link; (b) Power coverage of air gap inductive link; (c) Power coverage of EM-lens enhanced inductive link.

4.3 AC-DC Conversion Components

The induced AC voltage generated by alternating electromagnetic fields transmit through inductive links in the secondary LC tank. AC-DC conversion must be done to supply the remaining microelectronic circuits. Various AC-DC conversion topologies have been proposed for inductive links: half-wave rectifiers, full-wave rectifiers, bridge rectifiers, voltage doublers. The topologies can be divided into passive and active types dependent on whether they would require additional DC power supplies.

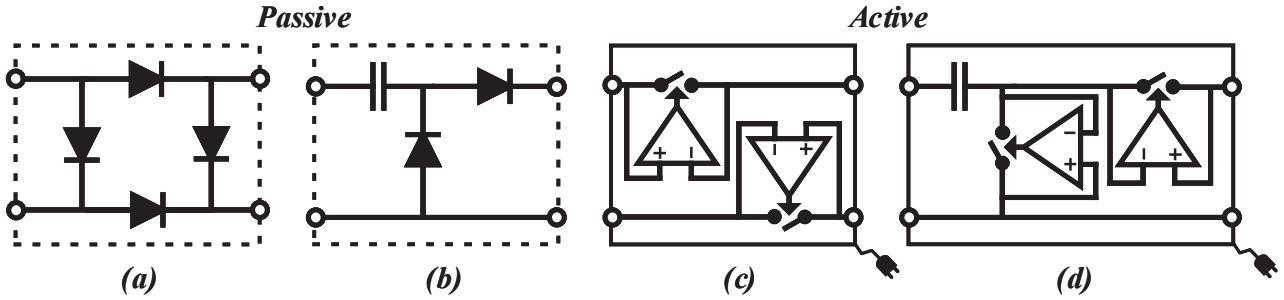


Figure 4.11: Various AC-DC converter topologies: (a) passive full-wave rectifier; (b) passive voltage doubler; (c) active full-wave rectifier; (d) active voltage doubler.

4.3.1 Passive AC-DC Converter

Schottky diodes are the most competitive and popular solution among various passive AC-DC conversion circuits. It has a lower forward voltage drop and smaller junction capacitance than MOSFETs, which means that it has a higher power conversion efficiency (PCE) which also operating at a relatively high operating frequency [128]. Only discrete Schottky components can be integrated with power management IC, because standard CMOS technologies do not support the Schottky diode options.

Half-wave rectification with a single diode is preferred for low-power energy conversion systems (1 - 500 μW) because minimised input power is required to turn on the diode. However, the PCE is less than 50% due to wastage of half the AC waves. Full-wave, bridge, and multiple stage rectifications are usually used to load > 500 μW circuitry [129]. The theoretical PCE is 40.6% for half-wave and 81.2% for both full-wave and bridge rectifiers when the load resistance R_L is much larger than diodes' forward resistance $r_f \ll R_L$.

$$\begin{aligned} \eta_{half} &= \frac{4/\pi^2}{1+r_f/R_L} = 40.6\% \\ \eta_{full} &= \frac{8/\pi^2}{1+r_f/R_L} = 81.2\% \end{aligned} \tag{4.9}$$

Passive CMOS-based rectifiers are diode-connected MOSFETs to facilitate CMOS integration, but their PCE is generally worse than Schottky diodes due to the larger threshold voltage (V_{th}) of the MOSFET. Therefore, several V_{th} cancellation techniques [130–133] have been proposed to achieve significant PCE improvement. Standard static V_{th} cancellation techniques use additional circuits to provide constant compensation, regardless of the transient AC voltage applied

on the gate of the MOSFET [130, 131]. Although static V_{th} cancellation effectively reduces the on-resistance and allows smaller diode losses in the forward bias condition, the increment in reverse leakage limits the PCE enhancement when the gate voltage becomes excessively high. Subsequently, an H-bridge rectifiers [132] are proposed to achieve active V_{th} cancellation by using self-V_{th}-cancellation (SVC) technique and self-body-biasing technique [133]. Additionally, differential-drive cross-coupled connections in the H-bridge rectifiers reduce the reverse leakage current.

4.3.2 Active AC-DC Converter

To further reduce the forward voltage drop, active rectifiers [134] with additional comparators properly control the gate voltage of the switching MOSFET, such that the diode-connected MOSFET operates in the triode region with low on-resistance. However, this method is mostly adopted with low-frequency RF inputs because high-speed comparators inevitably increase power consumption. Moreover, comparators need an additional DC supply voltages to ensure their normal behaviour. Most importantly, an active rectifier usually has difficulty at start-up, particularly in low supply voltage conditions. The wireless power management unit on the Rx side fails to start autonomously due to low available DC voltages or power. Therefore, active rectifiers are not suitable for uncertain AC input, especially wireless power transmission with free-positioned receivers.

The selection in various AC-DC conversion topologies is based on design requirements, such as operating frequency, dropout voltage, input/output power, or PCE, in which the PCE is a crucial factor that affects the efficiency of the entire wireless power transmission system. The PCE is particularly sensitive to the operating frequency, input/output power, and load resistance. Therefore, it is necessary to clarify the constraints of the above parameters before rectifier design and optimisation.

4.3.3 Design Constraints

The on-chip rectification aims to provide 500 μW power and 1.5 V supply voltage for a $4.5k\Omega$ load resistance. The operating frequency of the rectifier depends on the resonant frequency of the EM-lens enhanced inductive link. According to Table 4.1, the operating frequency is selected as 433 MHz. The PCEs of the two passive full-wave rectifier types are compared based on their schematics and measurements.

4.3.4 Cross-Coupled Rectifier

The CMOS-based cross-coupled rectifier is shown in Figure 4.12(a). Input $RF+$ and $RF-$ AC voltages are obtained from the secondary LC tank. After passing through cross-coupled MOSFETs, the rectified DC voltage $VP+/-$ charges the smoothing capacitor C_s and load resistor R_L. When the electrical potential difference between $RF+$ and $RF-$ is positive, transistors M_{p1} and M_{n2} are switched on. Meanwhile, M_{p2} and M_{n1} turn off. Conversely, M_{p2} and M_{n1} are switched on to maintain the high voltage potential at $VP+$. Since all transistors are in the saturation mode, the dropout voltage of this rectifier can be written as

$$V_{drop-\mathrm{H}} = \sqrt{\frac{2I_d}{KP_N}\frac{L_n}{W_n}} + \sqrt{\frac{2I_d}{KP_P}\frac{L_p}{W_p}} \approx 0.39V \tag{4.10}$$

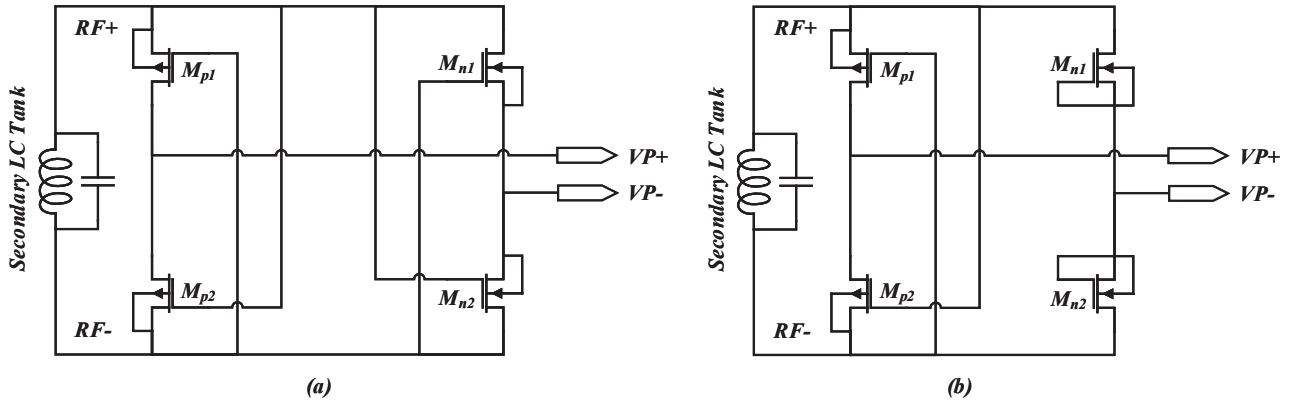


Figure 4.12: Schematics of two passive full-wave rectifier: (a) cross-coupled rectifier; (b) diode-connected rectifier.

4.3.5 Diode-Connected Rectifier

The diode-connected rectifier in Figure 4.12(b) replaces the cross-coupled connections M_{p2} and M_{n1} as diode-connections to prevent reverse currents. The dropout voltage is given by

$$V_{drop-\mathrm{D}} = V_{thn} + \sqrt{\frac{2I_d}{KP_P}\frac{L_p}{W_p}} \approx 0.89V \tag{4.11}$$

The dropout voltage of the cross-coupled rectifier is 500 mV less than that of the diode-connected rectifier[1]. The dropout voltage of the diode-connected rectifier can be reduced from 0.89 V to 0.66 V by using the low V_{thn} N-channel MOSFETs. The simulated results of the cross-coupled rectifier, low Vt and standard Vt diode-connected rectifier in Figure 4.13(a) shows the dropout voltages are close to the calculated values in equations 4.10 and 4.11. The DC voltages are obtained by adding a 660 pF smoothing capacitor C_S in parallel with the load resistance R_L.

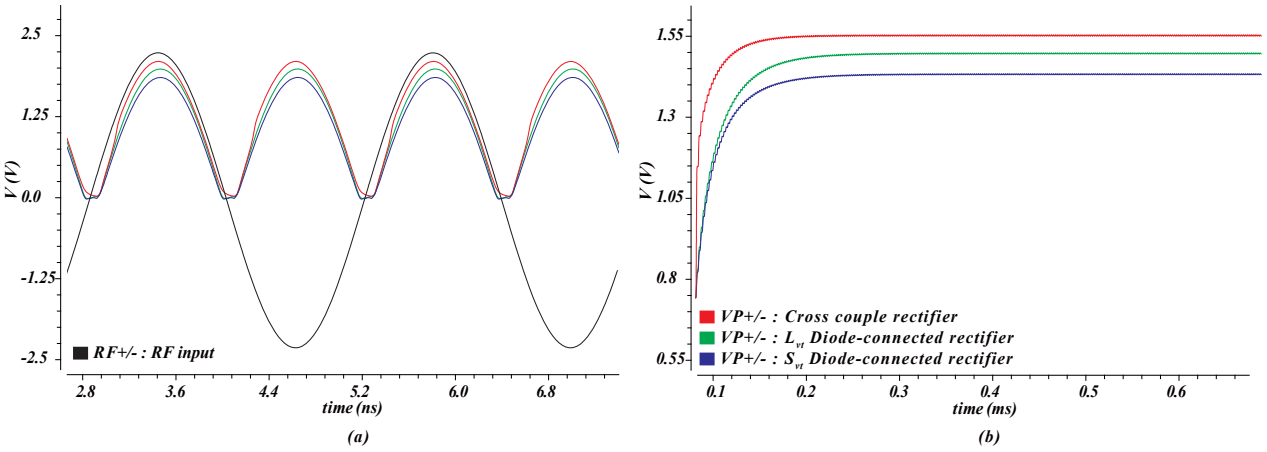


Figure 4.13: Simulated results for cross-coupled rectifier, low Vt and standard Vt diode-connected rectifiers: (a) dropout voltage comparison; (b) rectified DC voltage with 660 pF smoothing capacitor.

[1]Transconductance coefficients KP_P, KP_N of PMOS and NMOS in AMS H35B4 technology are 58 $\mu A/V^2$ and 170 $\mu A/V^2$. The current I_d flowing through the load resistance is 333.3μA. Threshold voltages V_{thn} of 5 V standard Vt and low Vt N-channel MOSFETs are 0.7 V and 0.47 V, respectively.

4.3.6 Measurement Results

The cross-coupled rectifier, low Vt and standard Vt diode-connected rectifiers are designed and fabricated in AMS 0.35 μm process. The chip microphotographs of all the rectifiers are shown in Figure 4.14. All the width and length ratios (W_n/L_n) of the NMOS devices are set as 100 to reduce V_{drop}, and the W_p/L_p of the PMOS devices are set as 300 due to its low transconductance coefficient. The chips under test (DUT) are wire-bonded to pads on the test PCB, thereby avoiding the use of a ceramic leadless chip carrier (LCC), which can introduce extra parasitic capacitance in the input impedance.

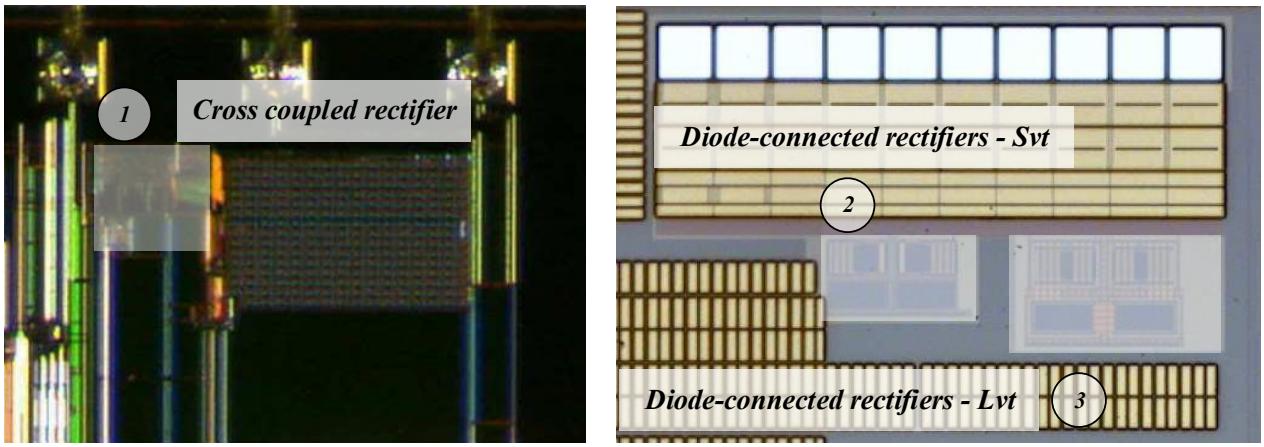


Figure 4.14: Chip microphotograph of (a) cross-coupled rectifier; (b) standard Vt and low Vt diode-connected rectifiers.

To analyse the PCE of these on-chip rectifiers with respect to the operating frequency, it is necessary to control both the RF signal generator and the oscilloscope to perform data acquisition and analysis. Labview is used to control concurrent measurements of these two devices through a GPIB and an Ethernet connection. The measurement process is shown in the graphical user interface (GUI) in Figure 4.15. First, the RF signal generator (R&S SML03) produces AC signal sources as inputs of the on-chip rectifier. Meanwhile, the LeCroy 7300A oscilloscope measures the instantaneous waveforms at the input and output of the rectifier to verify the input frequency, amplitude, and evaluate the output DC voltage, ripple, including the power conversion efficiency calculations.

Three rectifiers with different topologies are compared through measurements. After performing

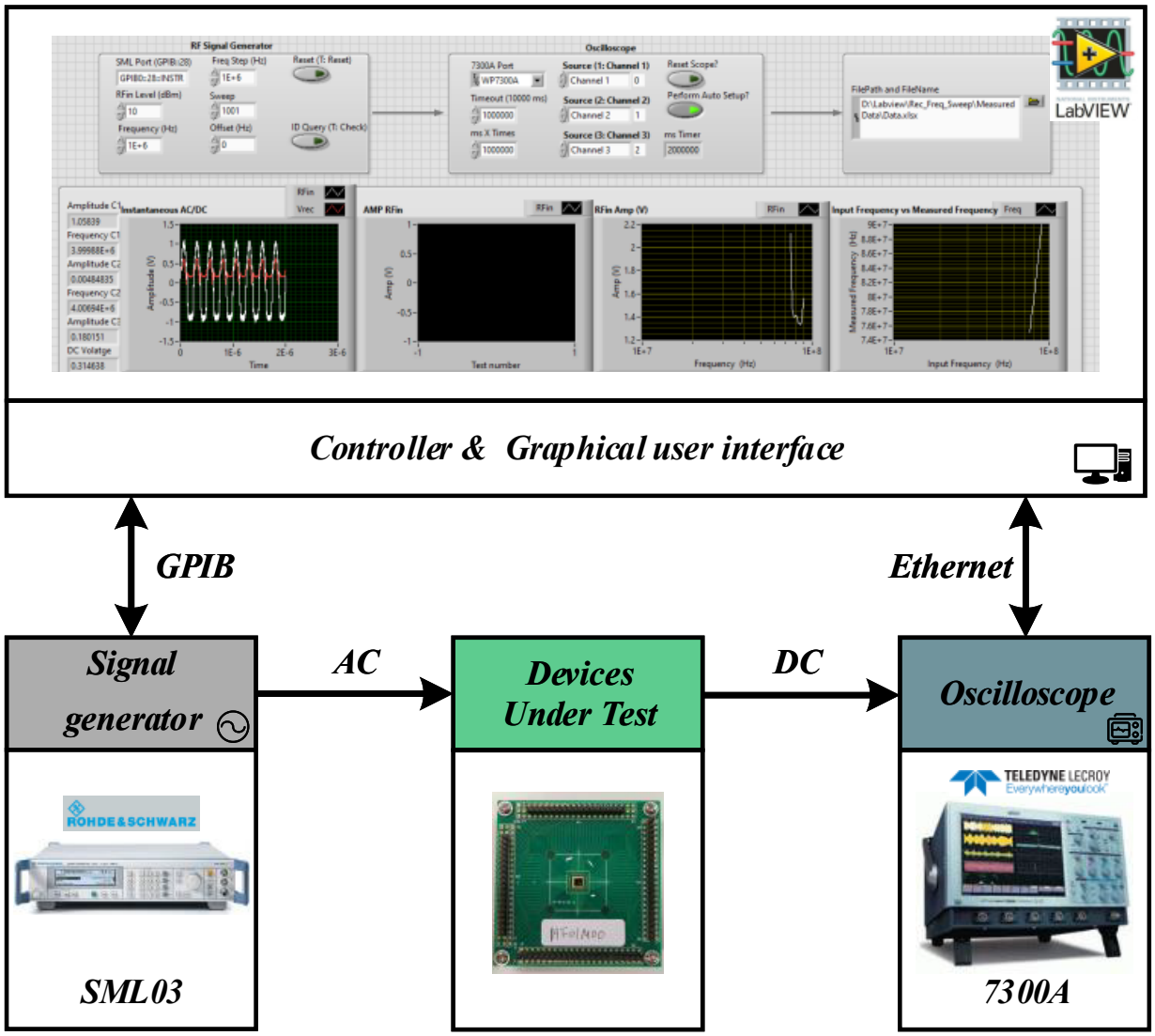


Figure 4.15: Experimental setup of PCE evaluation in terms of operating frequency.

a frequency sweep from 1 MHz to 1 GHz, the measurement results of three different rectifier topologies are shown in Figure 4.16. The PCE of the cross-coupled rectifier is 68.02% at 141 MHz. Two diode-connected rectifiers are designed with standard V_{th} MOSFETs or low V_{th} MOSFETs, and their PCEs are 48.78% at 207 MHz and 64.14% at 245 MHz, respectively. The dynamic output ranges of diode-connected MOSFETs are not as wide as those of cross-coupled ones, so their power conversion efficiency is limited. Low V_{th} NMOS decreases the standard V_{th} from 0.7 V to 0.47 V, which results in a dropout voltage reduction and hence improves the PCE of the low V_{th} rectifier. The typical characteristics of the high-frequency Lecroy HFP2500 probe introduces the following effects on the measurement results. The input capacitance of the

probe is 0.7 pF, which causes 12.03% reduction of SRF at the primary LC tank. In addition, the 100 kΩ DC probe resistance at the output terminals, in parallel with the 4.5 kΩ load resistance, will also cause 4.22% deviation.

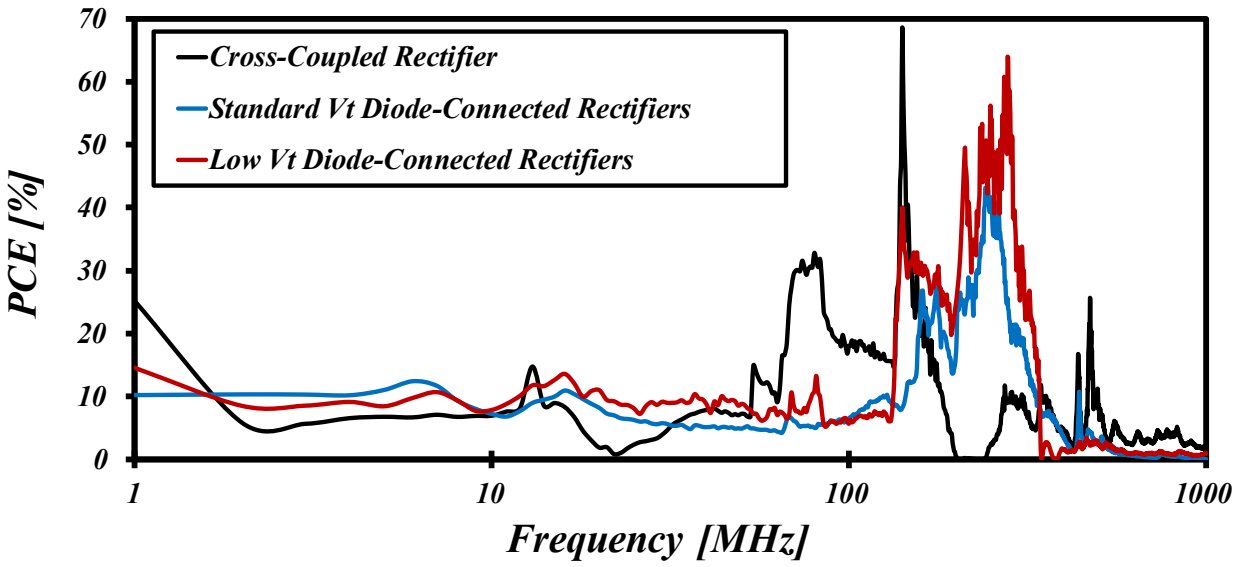


Figure 4.16: Measured PCE of cross-coupled rectifier, standard threshold and low threshold diode-connected rectifiers.

4.4 Inductive Link and Rectifier Co-design

In recent years, wireless power receivers have become prevalent, but their power efficiency cannot always be correctly evaluated. Since the inductive link and the rectifier are often optimised separately, a matching network sloppily inserted into them to match the impedance without optimising the inductive link and the rectifier together during the design phase. This often results in the entire system working in sub-optimal conditions. Recently, the co-design of rectifiers and antennas has been achieved for long-range RF energy harvesters, but the antenna is often treated as an accessory of the rectifier. After the optimal rectifier is implemented, the antenna is designed to match its input impedance [135,136]. This is because the power efficiency is extremely low in far-field conditions, and the optimisation of the antenna cannot bring significant improvements to the entire system. However, in near-field regions, the inductive link is often optimised first to achieve the maximum power transmission efficiency. The rectifier is then co-designed to fit the determined input power and operating frequency.

4.4.1 Analytical Model

The rectifier is essentially a nonlinear circuit, which means that a nonlinear model needs to be established to accurately predict the performance of the rectifier. The nonlinear model of the MOSFET rectifier in [137] contains the effect of conduction angle, leakage current and body effects, but optimise the PCE without considering the inductive links. Nevertheless, this sophisticated model cannot perform intuitive analysis from the impedance and frequency domains. Additionally, this model has been created for a specific rectifier structure, and cannot perform general analysis on any rectifier topology. Figure 4.17 combines the simplified rectifiers model from [136] and an inductive link model. This simplified equivalent model provides an intuitive understanding of the essential characteristics for the co-design of the inductive link and the rectifier.

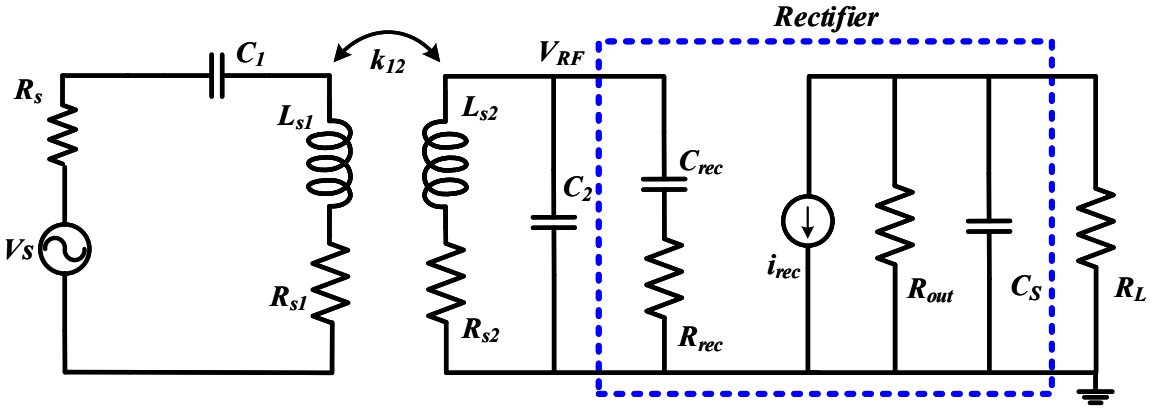


Figure 4.17: Inductive link and rectifier equivalent circuit model.

The equivalent circuit of the rectifier (in the blue dashed box) consists of input capacitance C_{rec}, input impedance R_{rec}, and load current source i_{rec}, output impedance R_{out}, and smoothing capacitor C_s. C_{rec} is composed of MOSFETs' overlap and junction capacitance and side-wall junction capacitance, which can be expressed as:

$$C_{rec} = C_{pmos} + C_{nmos}, \tag{4.12}$$

where

$$C_{pmos,nmos} = C_{ovl}W + C_jWL + 2C_{jsw}(W + L). \tag{4.13}$$

Input impedance R_{rec} of rectifier depends on the serial source impedance of MOSFETs. It can be expressed as

$$R_{rec} = \frac{1}{g_{m,nmos}} + \frac{1}{g_{m,pmos}} = \sqrt{\frac{1}{2\mu_n C_{ox} I_d} \frac{L_n}{W_n}} + \sqrt{\frac{1}{2\mu_p C_{ox} I_d} \frac{L_p}{W_p}}. \tag{4.14}$$

The equivalent current source generates the current i_{rec} to load the resistance R_L. This current can be written as

$$i_{rec} = (g_{m,nmos} + g_{m,pmos})\, V_{RF} = \left(\sqrt{2\mu_n C_{ox} I_d \frac{W_n}{L_n}} + \sqrt{2\mu_p C_{ox} I_d \frac{W_p}{L_p}} \right) V_{RF}. \tag{4.15}$$

Thus, we can define the transconductance of rectifier as

$$g_{m,rec} = \frac{i_{rec}}{V_{RF}}. \tag{4.16}$$

The output impedance of rectifier R_{out} is parallel with load resistance R_L, which depends on the drain impedance of switching MOSFETs. If the channel-length modulation λ is ignored here, the output impedance of rectifiers tend to be infinite, thus the current i_rec mainly flows through the load resistance R_L. The expression of output impedance R_{out} can be written as

$$R_{out} = r_{o,nmos} + r_{o,pmos} = \frac{1}{\lambda_{nmos} I_d} + \frac{1}{\lambda_{pmos} I_d}. \tag{4.17}$$

The smoothing capacitor C_s can be defined as

$$C_s = \frac{1}{2\pi f} \frac{I_d}{V_{ripple}}. \tag{4.18}$$

The converted DC power on the load is express as

$$P_{out} = i_{rec}^2 (R_{out} \parallel R_L) \approx i_{rec}^2 R_L, \tag{4.19}$$

where R_{out} in order of $M\Omega$ is much larger than the load resistance $4.5k\Omega$ ($R_{out} \gg R_L$). The

input power can be written as

$$P_{in} = \frac{V_{RF}^2}{2\left(R_{rec} + X_{rec}\right)}. \tag{4.20}$$

Therefore, the PCE of rectifiers can be defined as

$$\eta_{PCE} = \frac{P_{out}}{P_{in}} = 2g_{m,rec}^2 R_L \left(R_{rec} + X_{rec}\right), \tag{4.21}$$

where $X_{rec} = 1/(\omega C_{rec})$. The PCE of CMOS-based rectifiers depends on the width and length ratio, since $g_{m,rec}$ is proportional to $\sqrt{W/L}$, and R_{rec} is proportional to $\sqrt{L/W}$. In addition, load resistance R_L and operating frequency $\omega = 2\pi f$ are defined by the previous EM-lens enhanced inductive link.

4.4.2 Rectifier Optimisation

Figure 4.18 shows the simulated results of the PCE for a cross-coupled rectifiers with various width-length ratios W/L and input power levels. The simulated results suggest that the maximum PCE of 60% can be achieved when the W/L is set to 18 and the input power fixed at 14 dBm.

4.5 Self-Regulated Power Management

The sulci and gyri of the cerebral cortex lead to an uneven brain surface. Thus, the distances, alignments and orientations between each implant and the EM-lens are different. This results in different coupling coefficients with each distributed Rx coil such that the induced electromagnetic fields on the secondary side are unpredictable. Meanwhile, considering the micromotion of the brain in the skull, the received electromagnetic fields may be varied for the same Rx device at the different time. The adjustment of adaptive transmitter output power to compensate secondary voltage fluctuations is a feasible solution for a single implants. It is, however, not a practical scheme for multiple implants, which might have independent voltage variations.

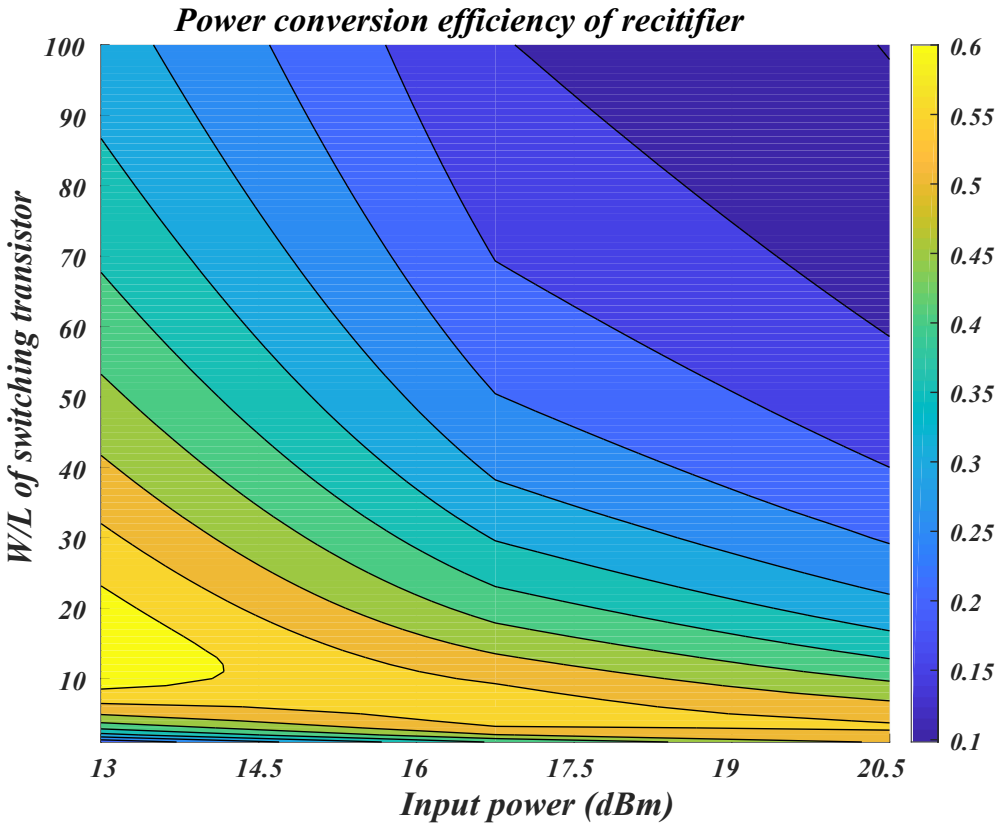


Figure 4.18: Simulated PCE in terms of W/L and input power.

The conventional power management circuits in wireless power transmission systems are composed of two independent parts: an AC-DC rectifier and a DC-DC regulator. The voltage regulator consists of a voltage reference, an error amplifier, a resistor divider and a pass transistor. Its power loss, however, is high because the internal feedback loop contains a resistor divider [138]. Some circuits use buck/boost DC-DC converters to replace the regulator. However, standard DC-DC converters require an additional inductor, which leads to an undesirable increase in chip area and inevitable interference with the inductive link. Hence, it is not a favoured design decision.

The concept of autonomous power management for each implant aims to provide a self-regulated and stable supply voltage. A conventional two-stage cascade power management design consists of a rectifier and a voltage regulator. The power loss through the two stages is undesirable, particularly for implants with limited available power (usually in the 100s of μW). Thus, the solution of combining AC-DC rectification with voltage regulation has been frequently proposed for neural implants [55, 139] even for low power RFID [140].

4.5.1 System Architecture

Figure 4.19 shows the system architecture of the self-regulated power management unit. This block diagram contains a cross-coupled rectifier, supply voltage detector, digital tuning capacitor C_T, and auto-tuning module to implement both AC-DC voltage conversion and supply voltage stabilisation. The principal operating procedure of these modules starts from an AC-DC conversion through the cross-coupled rectifier. The rectified DC voltage V_{dd} then passes through the voltage detection module, which generates corresponding digitised flags to indicate change direction of the supply voltage. The finite state machine (FSM) generates 8-bit tuning data based on these flags to control corresponding bits of the capacitor array C_T. The capacitors C_2, C_D, C_T and the Rx coil L_{s2} determine the SRF of the secondary LC tank. The received voltage on the secondary side can be effectively maintained by tuning its SRF because the entire inductive link is resonance-based wireless power transfer. The final judgement of supply voltage V_{dd} is determined by the overvoltage and undervoltage flags generated by a bandgap reference (BGR). Therefore, the entire system ensures that the DC power supply voltage is stable at 1.5 V.

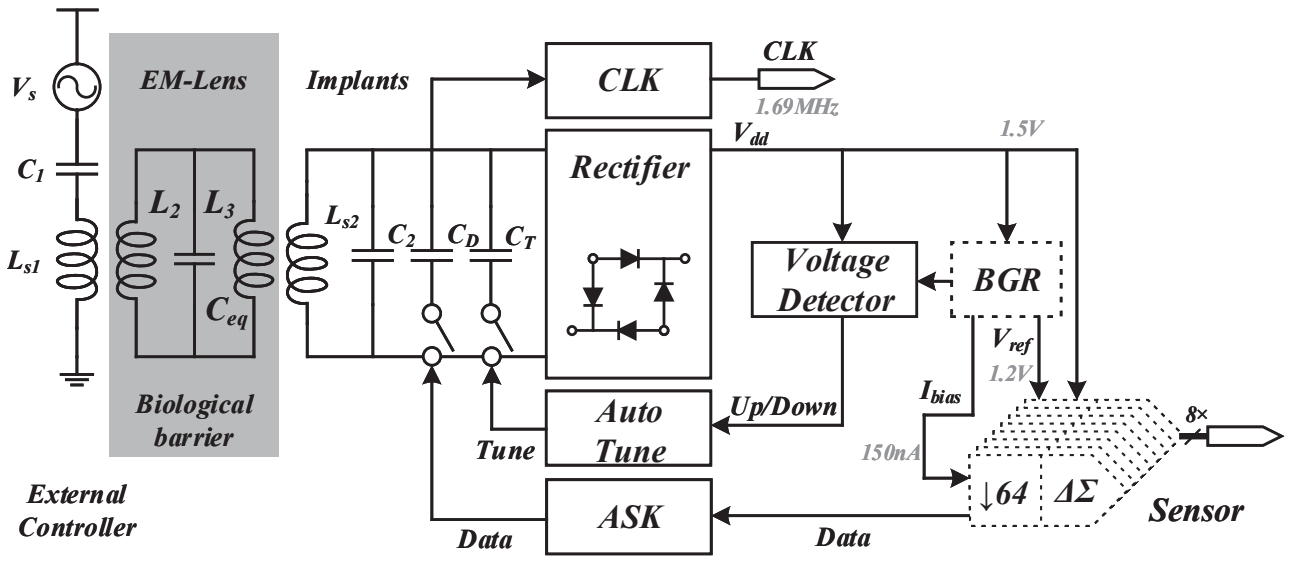


Figure 4.19: Proposed self-regulated power management system includes: cross-coupled rectifier, supply voltage detector, digital tune capacitor, and auto-tune FSM.

4.5.2 Supply Voltage Detector

The supply voltage detector is a key analogue circuitry in this power management system. It detects the fluctuation of the power supply voltage and generates digital flags for the FSM to provide a judgement of its operational process. This circuit is composed of a switch capacitor amplifier and a strong-arm comparator [141], as shown in Figure 4.20. The switch capacitor amplifier is a common two-stage OPAMP with a wide swing cascode current source to provide a stable tail current and bias voltage for OPAMP. The start-up circuit in the current source ensures automatic start-up behaviour. Two dummy switches are placed on both sides of the source and drain the NMOS switch S_1 to reduce the effects of charge injection and clock feed through. The operational flow of this circuit consists of the following three steps: sampling, tuning, and comparison. In the sampling phase, the circuit operates as a unity gain buffer when the switch S_1 is on. The current supply voltage V_{in} is sampled and stored in capacitor C_1. In tuning mode, S_1 is off while the FSM changes the SRF by adding one unit capacitor to the secondary side LC tank. Variations in the SRF inevitably cause V_{in} fluctuations. This voltage fluctuation causes the charge to change on the capacitor C_1; it then amplifies the negative feedback capacitor C_2 and appears as a positive or negative voltage V_x. In the final phase, V_x is compared with the ground V_{gnd} in a strong-arm comparator to indicate the polarity of the voltage change as a 1-bit digital output D_{PN}.

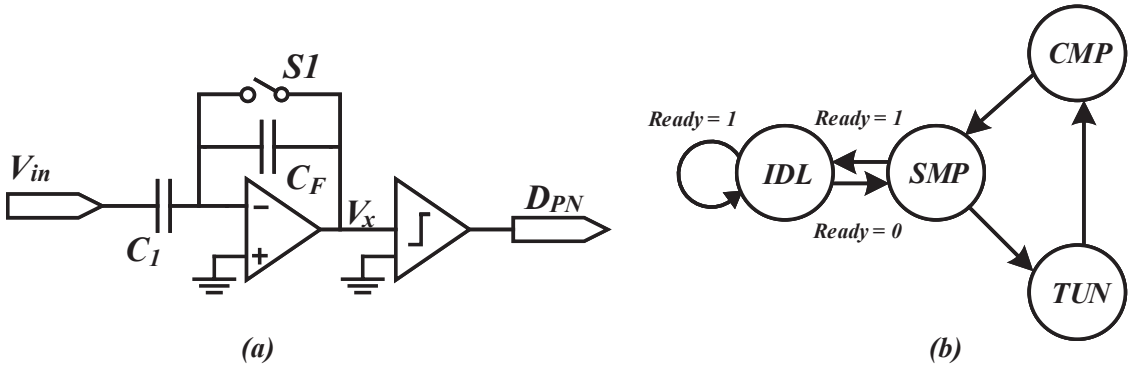


Figure 4.20: Detailed architecture of (a) supply voltage detector; (b) auto-tune finite-state machine (FSM).

4.5.3 Auto-Tune Module

A simple four-state FSM is implemented to control the switches in the supply voltage monitor and the 8-bit digital inputs of the capacitor array. The four states are idle, sample, tune and compare. The switching conditions between them are shown in Figure 4.20(b). The state machine continues running until the subsequent BGR generates a flag to inform the state machine that the power supply voltage is between 1.45 V and 1.55 V.

4.5.4 Digital Tune Capacitor

The unit capacitance of the 8-bit binary-weighted capacitor array is 59.64 fF (including parasitic capacitance), and its total capacitance of this array is 15.27 pF. The SRF is inversely proportional to the square root of capacitance $f \propto 1/\sqrt{C}$. SRF variations lead to induced voltage fluctuations on the secondary side. The maximum induced voltage is achieved when the secondary SRF is the same as the EM-lens. The induced voltage curve in terms of operating frequency conforms to a Gaussian distribution. This means that the unit capacitance may cause drastic changes in the induced voltage when the secondary SRF is close to the primary SRF. According to the simulation results, the rectified voltage variation is from 12.4 mV to 52.8 mV. The initial value of the binary-weighted capacitor array is set to 128 to ensure sufficient tuning range from 381.89 MHz to 509.99 MHz.

4.6 Measured Results

The method of connecting the above-CMOS coil to the active silicon die is shown in the insets of Figure 4.22. The previous above-CMOS coils are transferred from the 4-inch silicon wafer to a piece of polyvinyl chloride (PVC) transparent sheet by etching off the adhesive Cr layer that is shown in Figure 3.8. Then the two terminals of the above-CMOS coils are attached to pads of the active silicon die by using silver epoxy resin with 30 mins curing time at 100 °C. The active silicon chip contains on-chip tuning capacitors such that the secondary LC tank is

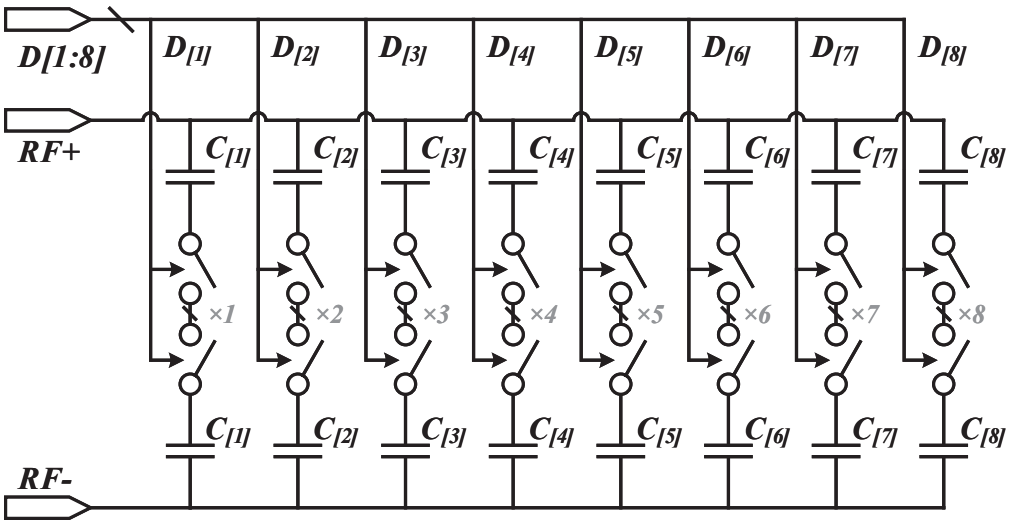


Figure 4.21: Digital tune capacitor schematic.

formed with this above-CMOS coil. The reflection coefficient Γ of the secondary LC tank is measured by VNA after assembling the above-CMOS coil, as shown in Fig. 4.22. Γ is less than -10 dB at 433 MHz, which proves this LC-tank has been successfully tuned to 433 MHz.

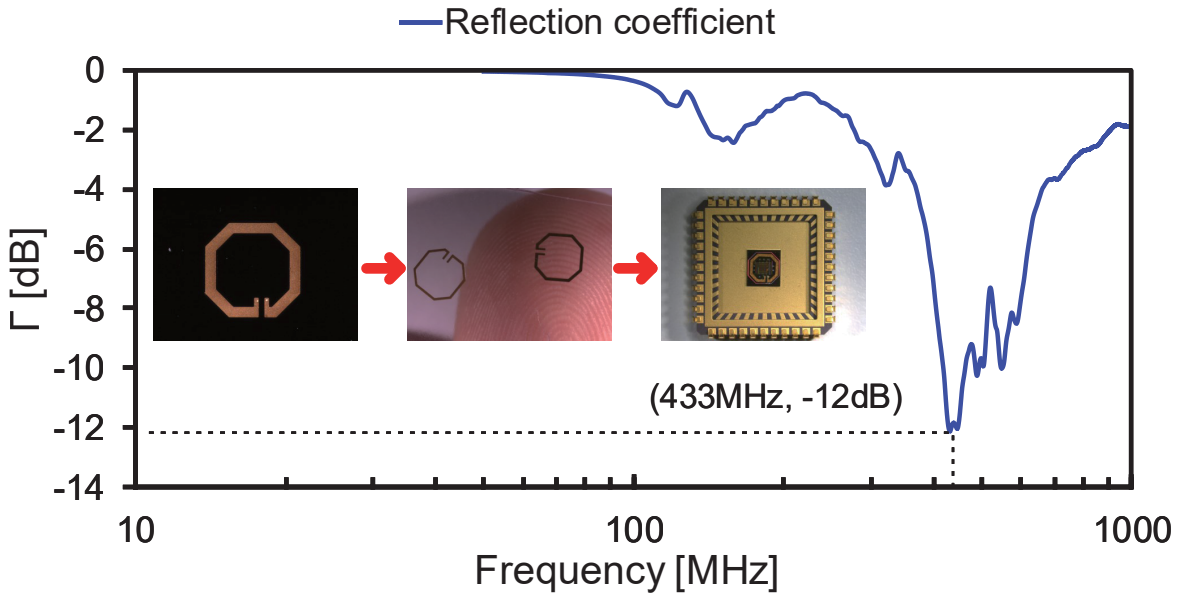


Figure 4.22: Measured reflection coefficient of the secondary LC tank to show its self-resonant frequency. Insets depict the transfer above-CMOS coil integration with active CMOS chip.

The first generation of ENGINI chip, as shown in Figure 4.23, is designed and fabricated in AMS 0.35 µm CMOS technology. This prototype is constructed to evaluate our inductively coupled wireless power transmission and on-chip self-regulated power management unit. Even though the entire chip area reaches to 4 mm × 4 mm, the core area is only 1.6 mm × 1.3 mm.

The rest of the unused area is saved for above-CMOS Rx coil and seal-ring.

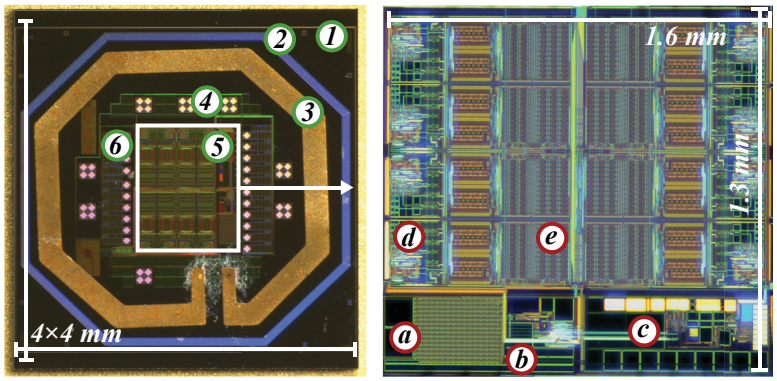


Figure 4.23: ENGINI chip microphotograph with a close-up of the electronic subsystem. The chip is labelled as follows: 1. silicon substrate, 2. seal ring, 3. above-CMOS Rx Coil, 4. pads for electrode connections, 5. active core, 6. pads for testing , a. auto-tuning capacitor, b. self-regulated power management, c. bandgap reference, d.$\Sigma\Delta$ ADC, e. CIC decimation filter.

Figure 4.24(a) shows the measured RF input of the LC tank from the primary side. Measured amplitude variations of the Tx RF input voltage indicates the auto-tune mechanism are working constantly. Since the FSM did not define the overflow flag, the 8-bit digital input of the tune capacitor overflows to over approximately 0.5 ms. Figure 4.24(b) show both the input and output voltage of the cross-coupled rectifier on the secondary side. The ripple voltage reaches up to 378 mV with 130 pF on-chip smoothing capacitor. These measurement results indicate the potential improvements of this chip prototype: (1) well-controlled digital input for the tune capacitor by adding overflow flag into FSM; (2) ripple voltage suppression by increasing on-chip smoothing capacitor to 1.3 nF.

4.7 Summary

This chapter presents the EM-lens enhanced WPT and an autonomous power management unit for powering multiple free-floating implants, while achieving adaptive voltage regulation. We have additionally introduced theoretical models for inductive links and rectifiers co-design, and an optimisation strategy for EM-lens enhanced 2-tier inductive link. The measured results of the active WPT verify the functionalities of EM-lens to demonstrate a four times improvement

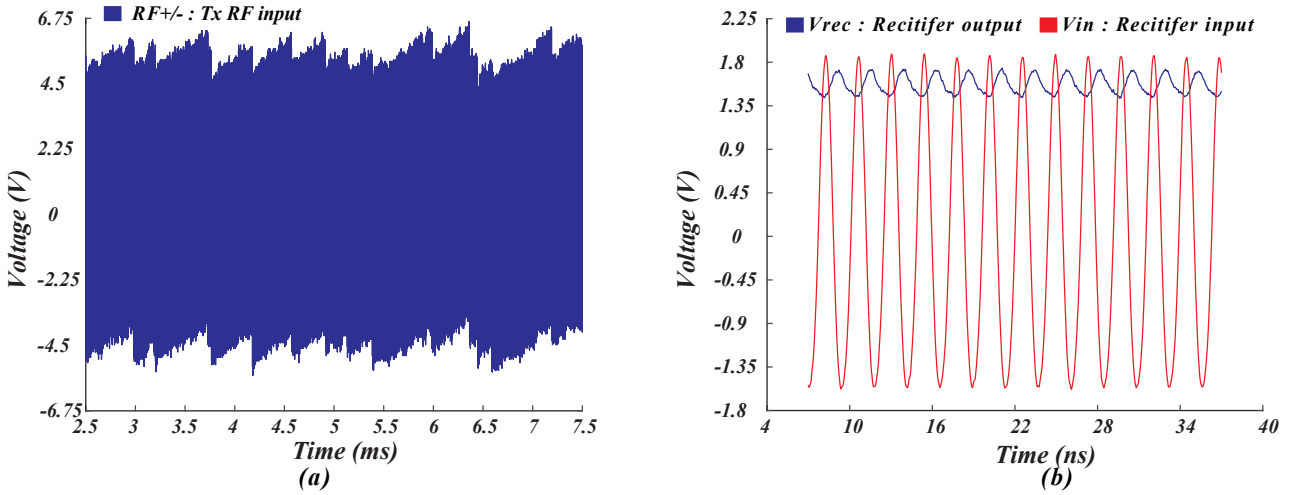


Figure 4.24: Measurement results of ENGINI chip: (a) RF input of LC tank from primary side; (b) input and output voltage of cross-couple rectifier.

in power coverage and a maximum two times enhancement of received voltage. Three different structures of passive full-wave rectifiers are compared by measuring the PCE in terms of frequency and input power to prove the highest PCE of the cross-coupled rectifier.

The technical recommendations in this chapter focus on wireless power transmission techniques and are summarised into the following four points.

- The EM-lens has significant improvement for the weakly coupled wireless power transfer system. The work in this chapter demonstrates received voltage enhancement from 1.8 V to 3.2 V at 12.5 mm Tx-to-Rx distance and power coverage extension from 45 mm^2 to 182 mm^2.

- The passive rectifier is preferable in the distributed wireless power transmission system since the active rectifier require stable AC input and an extra DC supply voltage at the startup condition.

- The cross-coupled rectifier has a lower dropout voltage than that of the diode-connected rectifier, which results in a higher PCE for the cross-coupled rectifier. In addition, the co-design of the rectifier and the inductive link is essential to match the impedance and maximise the total power efficiency of entire WPT systems.

- The self-regulated power management unit is one of the most critical components in distributed WPT to ensure each receiver maintain a stable power supply voltage.

Chapter 5

Multi-Node Data Transmission for Implantable Medical Devices

"Information is the resolution of uncertainty."

– Claude Shannon, 1916 - 2001

This chapter introduces a novel multiple-node data communication scheme for distributed implantable medical devices. The proposed scheme aims to tackle the general problem caused by concurrent data communication among multiple devices. For instance, these issues include intermodulation distortion with adjacent channels, data/power carrier interference, limited spectrum and channel capacity. In this chapter, a PCB prototype system has been implemented with commercially available discrete components as a proof of concept. The key technology of data communication is backscatter-based code division multiple access (CDMA). The backscatter scheme avoids on-chip data carrier generation to reduce the power consumption of implanted micro-system. The CDMA scheme spreads the spectrum based on a narrow wireless power transfer bandwidth with uncorrelated channelisation codes.

A portion of this work presented in this chapter has been published in [142].

5.1 Multiple Access for Multiple Implantable Devices

There are four standard multiple access techniques: frequency-division multiple access (FDMA), time-division multiple access (TDMA), code-division multiple access (CDMA), and space-division multiple access (SDMA) [143]. The illustrative comparison between FDMA, TDMA, CDMA is shown in Figure 5.1 and in Table 5.1.

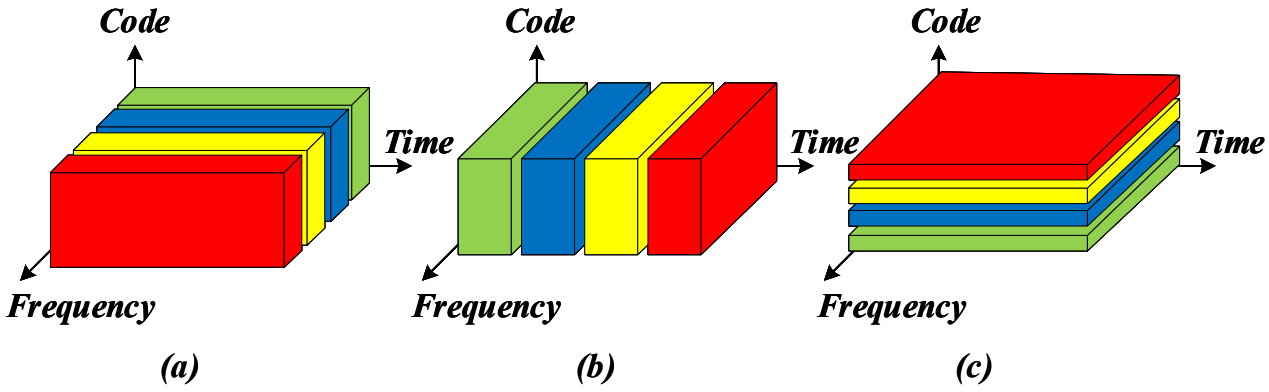


Figure 5.1: Comparison between (a) FDMA, (b) TDMA,and (c) CDMA.

The SDMA scheme uses spot beam antennas to separate RF channels by pointing in different directions. Focused ultrasound has high spatial resolution, so ultrasound-powered implants have been demonstrated by using SDMA to establish multiple simultaneous data links in different sectors [144]. Even though the SDMA scheme has a straightforward structure, only one node can be active in one sector. Thus, it is not suitable for concurrent EM data transmission in distributed implantable wireless systems.

The FDMA scheme assigns a specific frequency to each channel. The channel capacity is limited since the operating frequencies of EM implantable medical devices are usually selected in the 100s of the MHz domain. An ultrasonic FDMA approach starts to explore two MHz frequency channels [144]. To increase channel capacity and reduce interference, orthogonal frequency division multiplexing (OFDM) uses adjacent orthogonal multiple sub-carriers to transfer a data stream from a single channel. Therefore, OFDM utilises narrow bandwidth more efficiently than FDMA. The ultrasonic OFDM system for intra-body communication has been demonstrated to achieve a data rate up to 28.12 Mbps [145].

The TDMA scheme assigns a specific time slot to each channel. The channel capacity is also limited, and synchronisation between the Tx and Rx is key to achieving real-time data communication. Asynchronous TDMA has been implemented into 'Neurograins' and claims a 10 Mbps data rate [62, 146].

The CDMA scheme allocates an orthogonal or nearly orthogonal spreading code to each channel such that each channel uses its full bandwidth. The most significant advantage of CDMA is higher channel capacity within the same bandwidth than those of TDMA and FDMA. An ultrasonic CDMA systems has been implemented for 'Neural Dust' and achieved data rate up to 35 Kbps [94].

Table 5.1: Comparison between different coding techniques.

	SDMA	FDMA	TDMA	CDMA
Mechanism	Space	Frequency	Time	Code
Capacity	Limited	Limited	Limited	Unlimited
Transmission	Continuous	Continuous	Discontinuous	Continuous
Tx Complexity	Simplest	Most complex	Complex	Simple
Rx Complexity	Simplest	Simple	Most complex	Complex

We select CDMA as our multiple access technique based on the above review. It allows concurrent data communication with multiple nodes, and also takes advantage of a narrowband power carrier to perform modulation. Additionally, the data sender in each implant has a simple structure with low power consumption. Most importantly, the frequency spreading property is preferred for multiple access at high capacity.

5.2 Wireless Information and Power Transmission

The wireless information and power transmission (WIPT) system architecture of the multiple-node data communication for brain-machine interfaces is shown in Figure 5.2. The operational principle of proposed wireless information and power transfer (WIPT) system is described as *Power In & Data Out*. The downlink performs wireless power transmission from the external transceiver to free-positioned implants through the EM-lens. The uplink allows data communication for simultaneously collecting recorded neural activity data from multiple implants.

We propose the backscatter modulation and CDMA technique. The benefits of this wireless information transmission (WIT) scheme can be summarised as follows.

(1) High channel capacity : Channelisation codes spread the narrow frequency bandwidth and hold high capacity nodes at the same frequency to avoid allocating the limited time slots or frequency bands.

(2) Interference suppression : The encoded information is robust against channel fading and noisy environments due to the spectrum being spread over a wide bandwidth.

(3) Low power consumption : Power carriers are used to modulate data signals, thus no data carriers need to be generated in the implanted microelectronic systems.

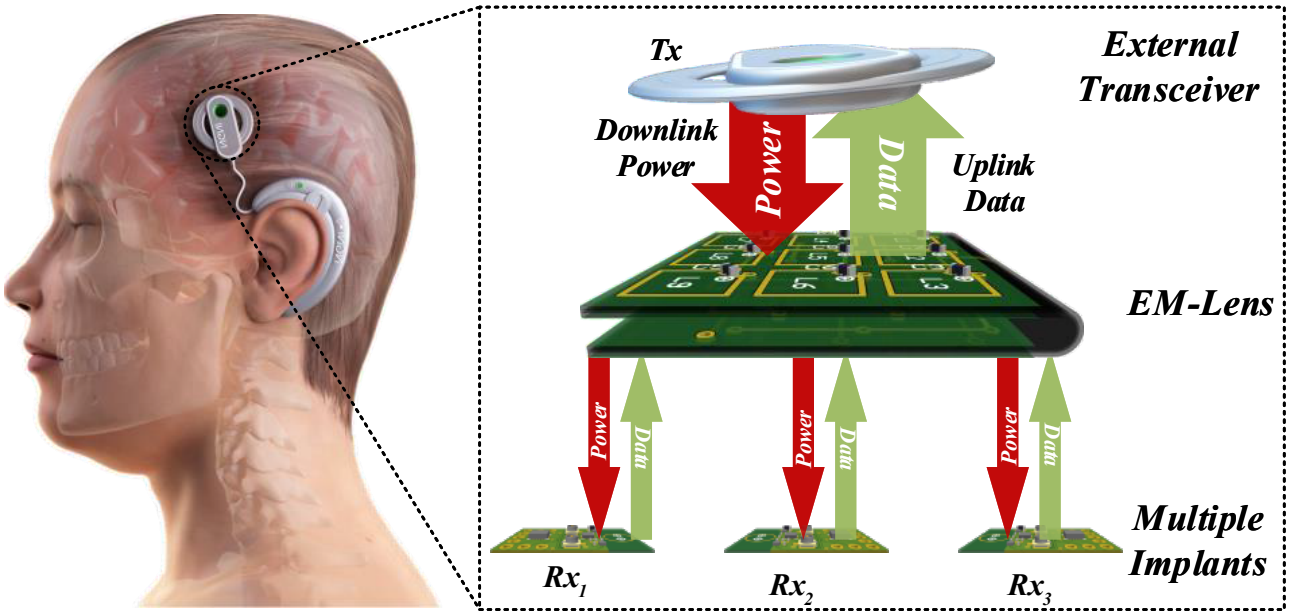


Figure 5.2: Proposed architecture of EM-lens enhanced wireless power transfer and multiple nodes data communication system for implantable medical devices.

5.2.1 WIPT Operating Principle

The simplified system schematic, as shown in Figure 5.3, contains the external transmitter, EM-lens, implanted power management and the data communication module. The detailed operating principle of the wireless power path starts from a -10 dBm power carrier generation

in the external transceiver. It is amplified up to 10 dBm through a power amplifier (PA) and injected into the primary L_1C_1 tank. The power carrier transmits through the EM-lens in the secondary L_4C_4 tank and is rectified from inductive AC voltage to DC voltage in the passive full-wave rectifier as stated in the previous chapter. The entire process of the data path starts from the input data $Data_{in}$ encoded by 16-element Walsh matrix channelisation codes in the MCU. It then sends the data to the tuning capacitor C_{TData} to perform backscatter modulation through the LPUART of the microcontroller (MCU). The transceiver on the primary side recovers the baseband information by using an I/Q demodulator and decodes the data from each node by using a synchronised code generator.

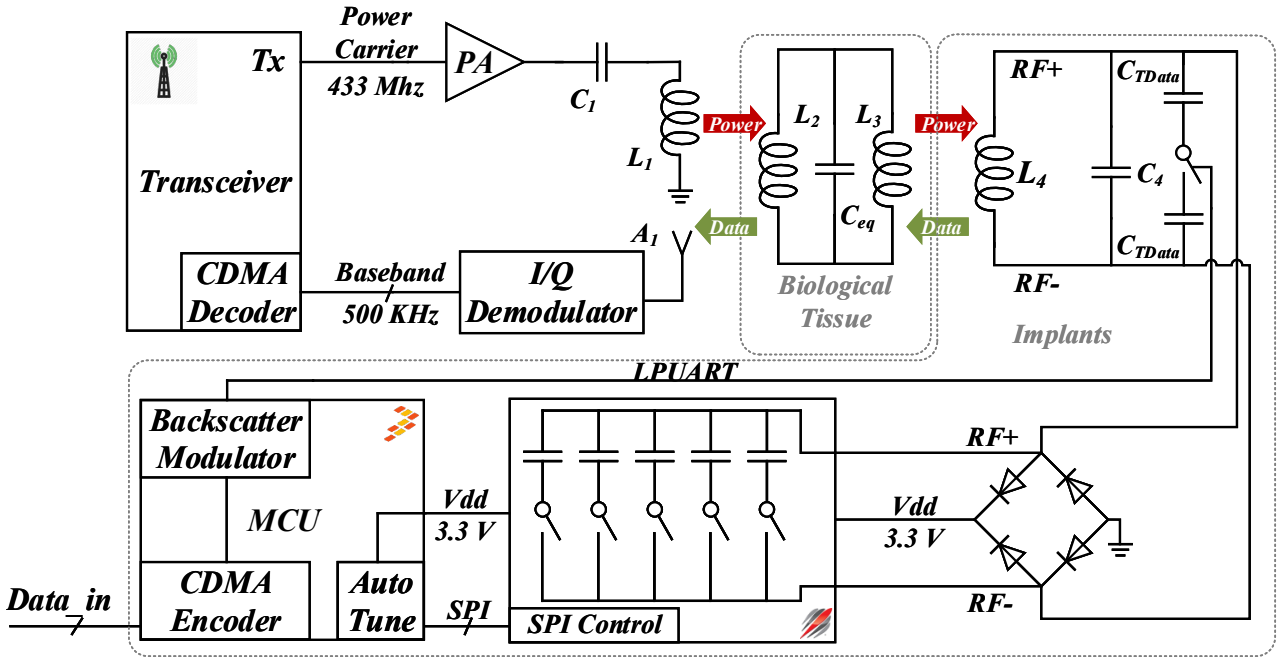


Figure 5.3: Simplified block diagram of external devices, implanted wireless interface and equivalent circuit model of EM-lens.

5.2.2 Proof of concept

The entire system is first built with discrete components on the PCB to verify the feasibility of the proposed wireless information transmission scheme between two nodes and a transceiver.

A. Experimental Setup

Figure 5.4 shows the experimental setup of the wireless backscatter-CDMA information transmission system. The CDMA encoding and the backscatter modulation processes are performed on wireless powered receivers Rx_1 and Rx_2. The wireless power scheme in Section 4.2.3 is adopted here. The differences from the previous scheme are that the RF signal generator is replaced by the software-defined radio frequency (SDR) platform and receiver Rx_1 and Rx_2 have been redesigned with data transmission capabilities. Moreover, the auto-tuning is realised by a digitally tunable capacitor (PE64102, Peregrine Semiconductor, USA). The SDR platform is based on a high performance, highly integrated RF transceiver daughterboard (AD-FMCOMMS4-BZ, Analog Devices, USA) and a Xilinx Zynq-7000 SoC motherboard (Zedboard, Avnet, USA). The received data signals from two nodes (Rx_1 and Rx_2) are first down-converted to the baseband through a built-in I/Q demodulation in the RF transceiver, then digitised by 12-bit sigma-delta ($\Sigma-\Delta$) ADCs. The digital signal process chain is implemented on a Zynq-7000 SoC, which contains a raised cosine FIR filter, Walsh code generator, serial search, and CDMA decoder. In addition, the power breakdown of each Rx node is reported in Figure 5.4 and the power consumption of each Rx device is 1047.6 µW.

B. Measured Results

Each node uses predefined index of Walsh matrix as the channelisation code to encode the input data in MCU. Encoded data is then sent through MCU's serial peripheral interface (SPI) to control the switch (RV1C002UN, Rohm semiconductor, Japan) of 5 pF tuning capacitor C_{TData}, resulting in $\approx$ 500 mV voltage variation on the primary RF signal. Meanwhile, rectifier has 660 pF smoothing capacitor to suppress this voltage variation within 40 mV on the rectified supply voltage. The measured signals on primary and secondary side are shown in Figure 5.5. The data from each node can be decoded by multiplying the corresponding channelisation code with $Data_{All}$, then averaging the decoded signal during every four clock cycles.

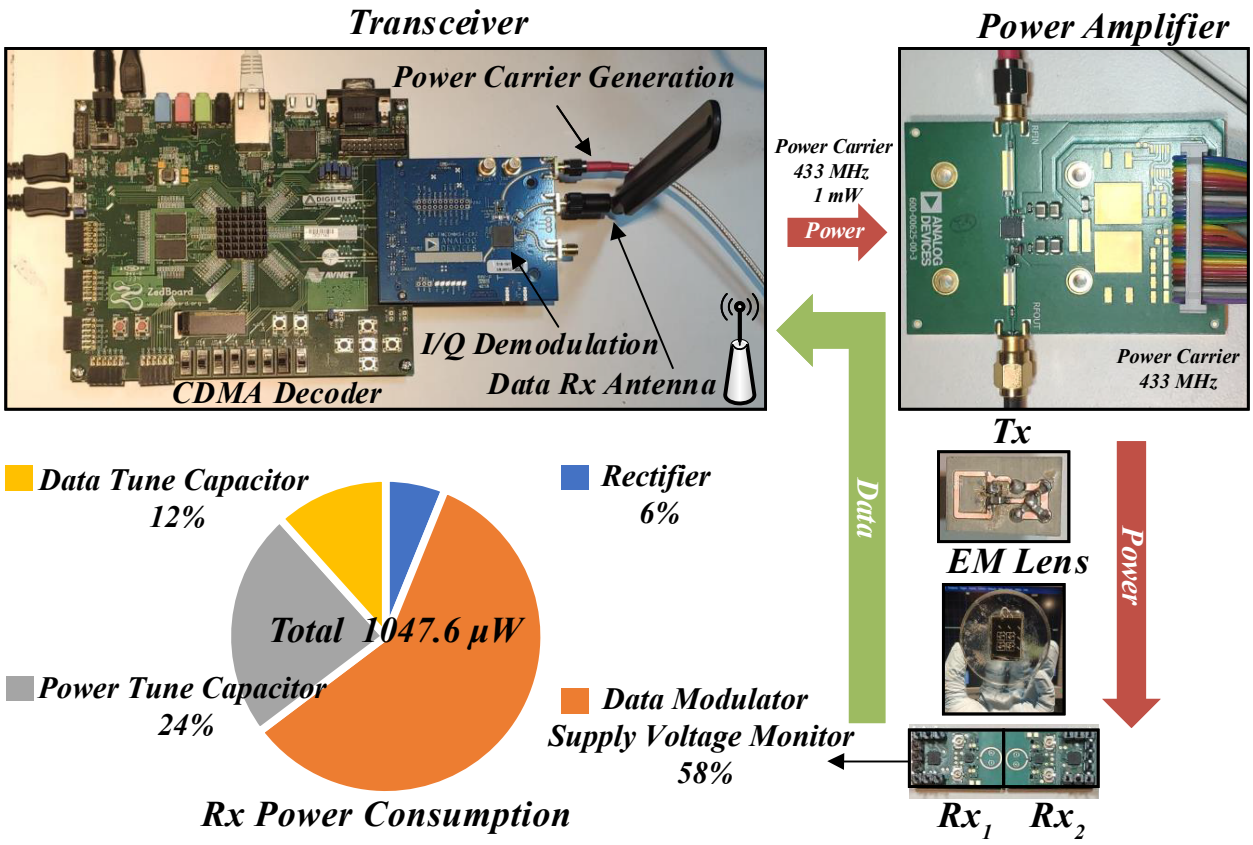


Figure 5.4: Experiment setup and Rx power consumption breakdown.

5.2.3 Discussion

This PCB prototype demonstrates the feasibility of code-division multiple nodes communication. Data modulation is realised by adopting backscatter the power carrier. Hence, it avoids the data carrier generation on the secondary side and reduces the power consumption of each data sender. CDMA takes advantage of narrowband inductive links for the power transmission to the spread spectrum, which enables all data channels to be located on the same frequency. The proposed backscatter-CDMA data communication technique shows a new direction for the following research about completely wireless infrastructure for distributed mm-sized neural implants.

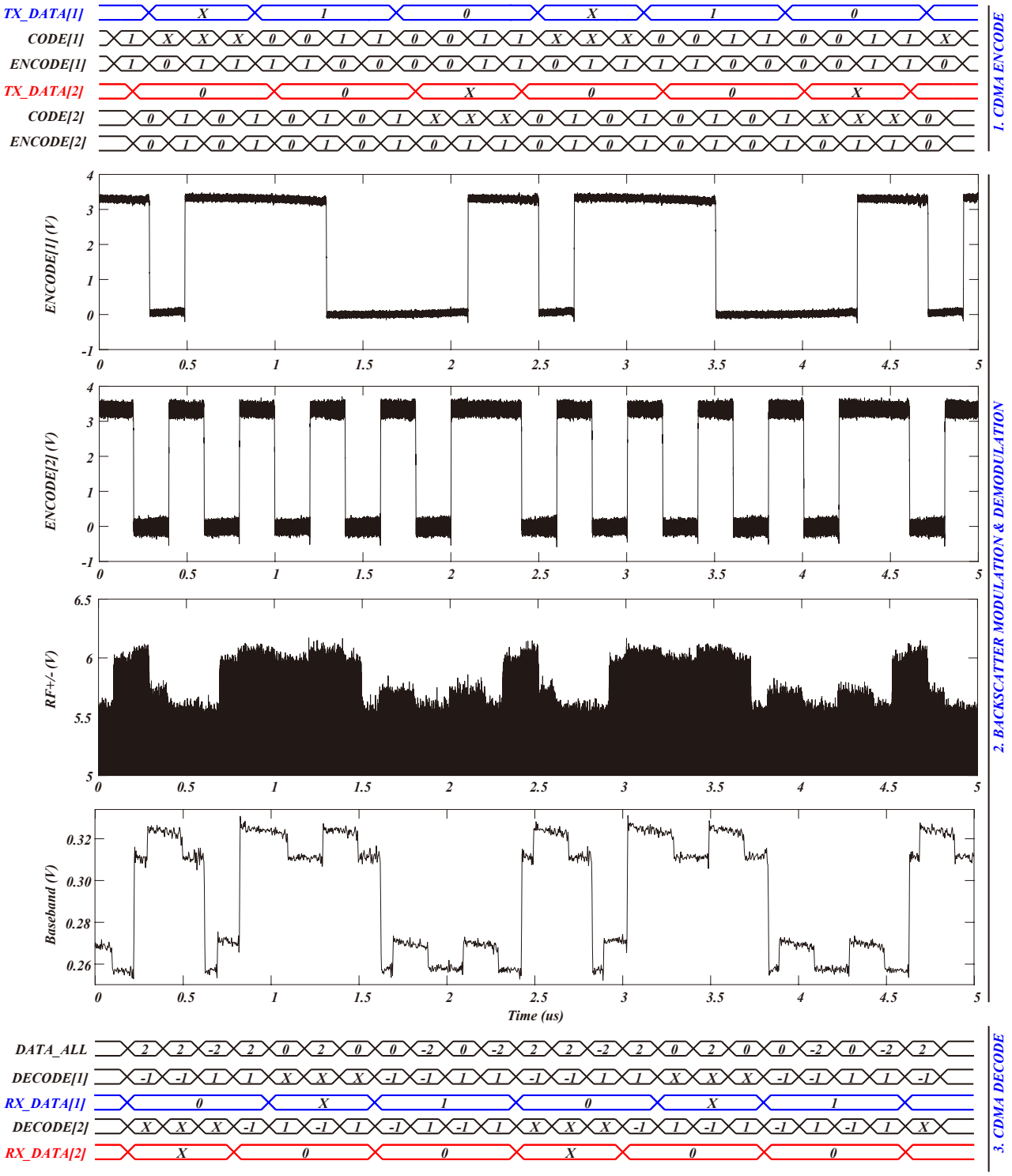


Figure 5.5: Time diagram of 2-node backscatter-CDMA data communication contains: (1). CDMA encoding stage; (2). Backscatter modulation and demodulation; (3). CDMA decoding process.

5.3 Autonomous SoC for Wireless Data Communication

The size of the PCB prototype with discrete devices reaches 308 cm^2, which is out of the range of millimetre-scale requirement. Additionally, the PCB substrate (FR4) is not biocompatible, and thus the integrated on-chip wireless powered data transmitter is designed on a silicon substrate. This is an essential step for reducing the system area and ensuring that it can fit into a hermetic package.

5.3.1 System Architecture

The system architecture diagram of wireless data communication is shown in Figure 5.6. FSK is selected as the wireless data modulation method. The demodulation method on the primary side comprises a bandpass filter, low noise amplifier (LNA) to recover the data. The operating principle and detailed diagram for the self-regulated power management have been previously stated in Section 4.5. The system has to complete the automatic power supply adjustment. After the power supply voltage reaches the required range of 1.45 - 1.55 V, the FSM generates an enable flag EN to start data modulation, and the input data can choose different frequencies of clock signals CLK_1 and CLK_2, by using the multiplexer MUX. These two clock signals originate from the secondary side RF signals and pass through the frequency divider to generate 54.125 MHz and 27.0625 MHz clocks. These two clock signals control the switches Mn_1 and Mn_2. These equivalent 50 fF capacitors are connected in parallel with the secondary side L_2C_2 tank, which can change its self-resonant frequency and reflect or scatter power carriers back to the primary side to achieve FSK modulation. The reasons for modulating input data to these two clock signals are summarised as:

1) High-frequency signals can effectively reduce the ripple generated on the rectified DC voltage ($V_{ripple} \propto 1/f_0$);

2) High-frequency signals can pass mm-sized inductive links and presents a significant voltage amplitude variation on the primary side.

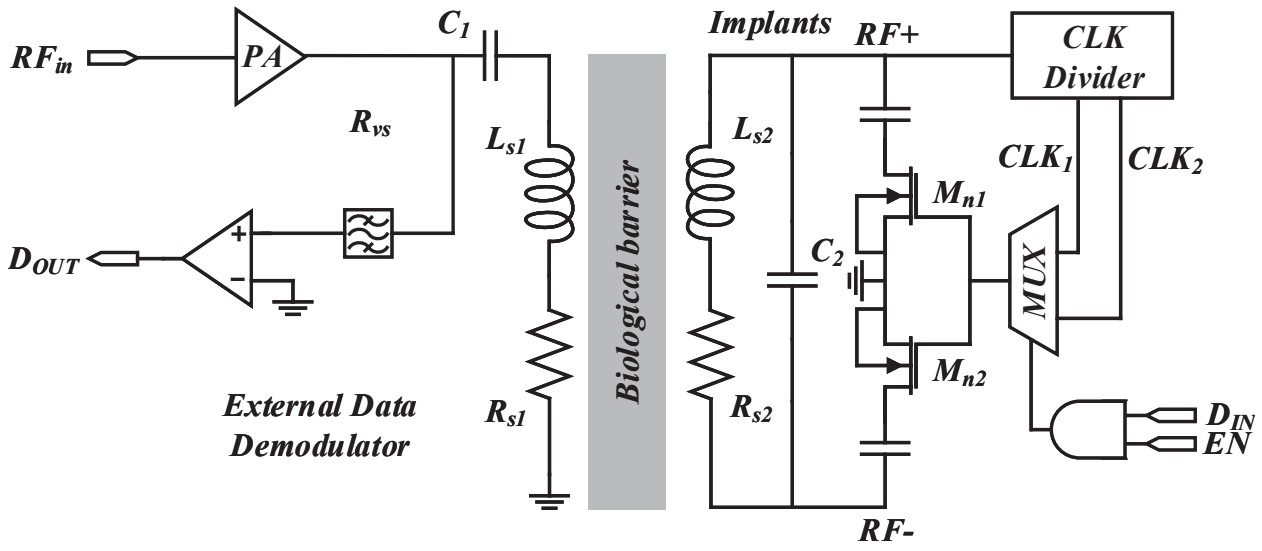


Figure 5.6: System architecture of autonomous SoC for wireless data communication.

5.3.2 System Validation

The wireless data communication system is simulated in Advanced Design System (ADS, Keysight Technologies, US), which is an electronic design automation software for RF application. This software enables simultaneous simulation of integrated circuits at the secondary side and discrete components at the primary side. The measured S-parameters of EM-lens enhanced inductive networks are imported into ADS as a two-port network. The BSIM3 model of HV NMOS switches M_{n1}, M_{n2} comes from AMS C35B4 process. They are simulated with PSpice models of LNA and lumped elements of RLC to perform the complete system analysis.

The simulated results in Figures 5.7(a) and (b) the peak-to-peak amplitude of RF input at 3.6 V and rectified DC voltage at 1.5 V with 30 mV ripple. The recovered data through the passive L-type bandpass filter and two-stage LNA have approximately 2 V at 25 MHz and 0.35 V at 50 MHz. Thus, the feasibility of the proposed wireless data communication system has been proved, since this recovered data from the primary side is consistent with the input data (blue curves in Figures 5.7(c) and (d)) from the secondary side.

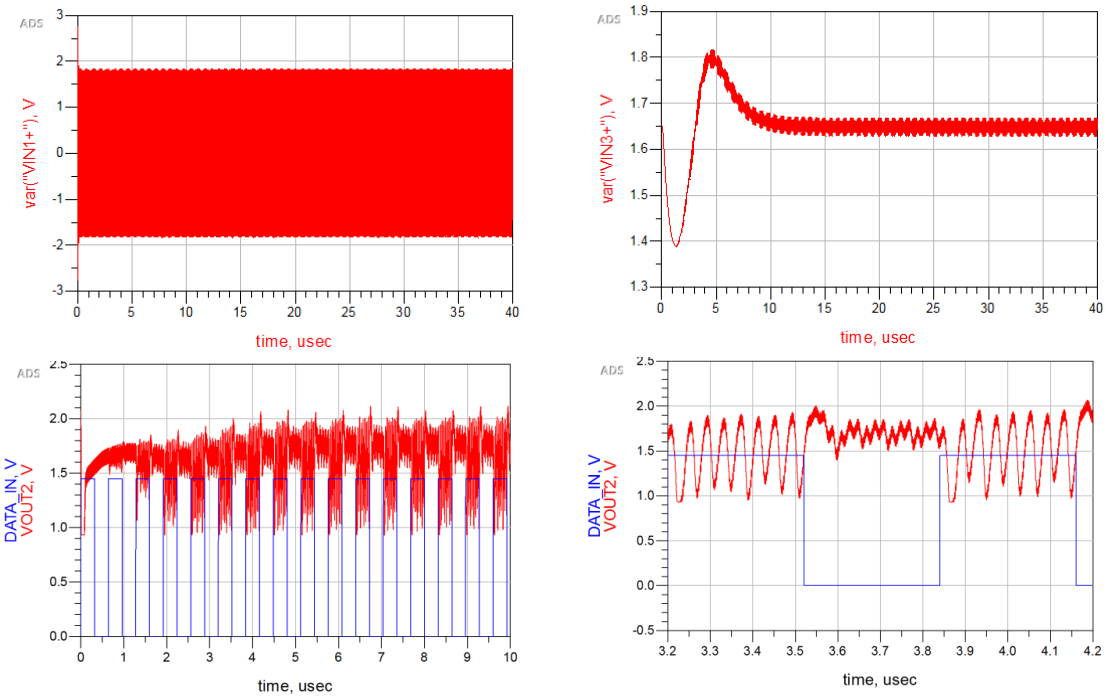


Figure 5.7: Simulated results of entire wireless data communication system: (a) Tx RF input; (a) Rx rectified DC voltage; (c) and (d) Tx recovered data.

5.3.3 Experimental Setup

The microphotograph of the mm-scale freely-floating neural probe is shown in Figure 5.8(b). This chip is designed and fabricated in the same 0.35 µm CMOS technology, as the first generation of ENGINI chip in Figure 4.23. The purpose of this prototype is to evaluate on-chip wireless data modulation. The core area of the data modulator occupies 205 µm×163 µm. The rest of the area is filled by smoothing capacitors and tuning capacitor array.

The dies under test (DUT) are directly wire-bonded to pads on the PCIe testing PCB as shown in Figure 5.8(a), thereby avoiding the use of ceramic leadless chip carrier (LCC) to introduce extra parasitic capacitance in the secondary LC tank. The on-chip tuning capacitor directly connects to the secondary coil on the PCB through the UF.L connector. The DUTs placed on Mini-PCIe daughter cards for multiple wireless powered data sender measurements. The motherboard has digital and analogue test ports that extend from dies. The on-chip digital debug ports with SPI implementation connect to Raspberry Pi for data collection. The analogue ports connect to the oscilloscope for measurement via SMA connectors for high

operating frequencies.

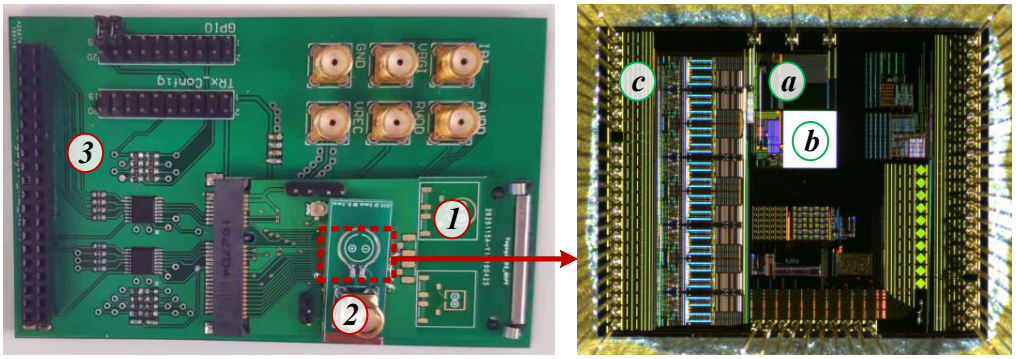


Figure 5.8: Experimental setup and chip microphotograph: (1) PCIe chip carrier; (2) inductive link; (3) debug motherboard; (a) wireless powered data modulator; (b) bandgap reference; (c) testing ports.

5.3.4 Measured Results

The limited measured results are caused by severe mistakes made during the chip design phase. A part of RF input metal track is less than 1 µm. The maximum current density of input RF power is limited to 0.5 mA and the highest induced AC amplitude at the secondary is limited to 1.3 V. The rectified DC voltage at 0.8 V is not sufficient to the rest of the circuit. If we attempt to increase the Rx induced voltage to over 1.5 V, the DUT can be damaged by electromigration failure to show approximately 0 V at the rectified DC voltage.

To bypass this issue, the low Vt rectifier, as shown in Figure 4.14(b), connects in parallel with this chip through bonding wires. These unexpected extra connections introduce parasitic capacitance into the secondary LC tank resulting in a reduction of self-resonant frequency. The measured spectrum of induced Rx voltage at the secondary LC tank indicates the 258MHz power carrier frequency and two data carriers at 31.6 MHz and 15.1 MHz.

5.3.5 Discussion

The chip prototype partly demonstrates the functionality of wireless data modulation scheme. The potential improvements for the next generation will be multiple access implementation.

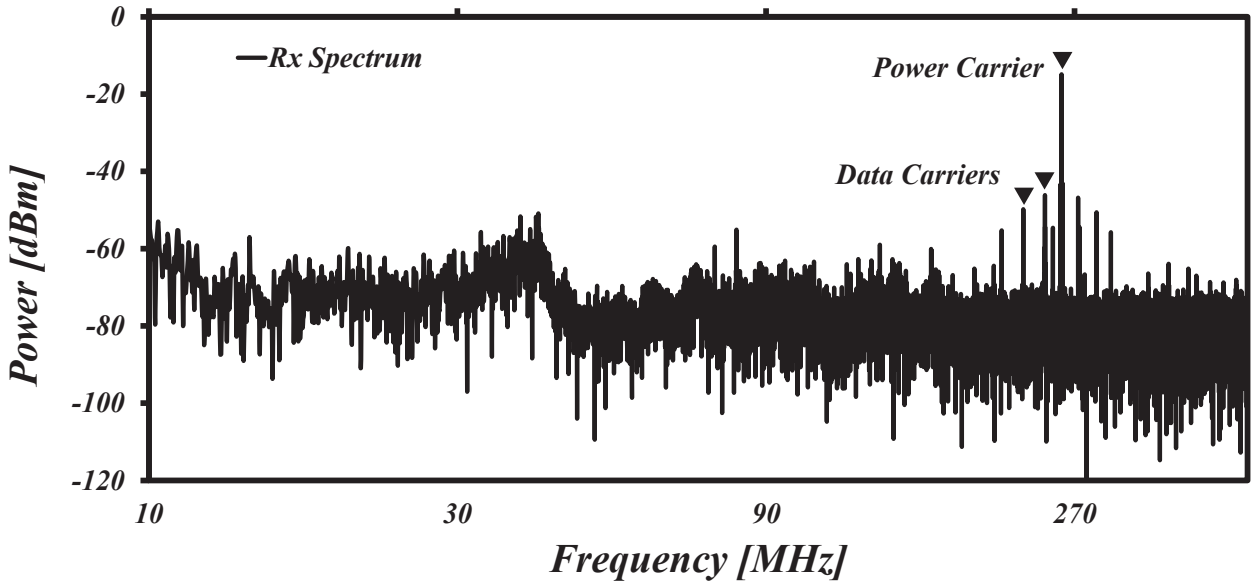


Figure 5.9: Measured spectrum of induced Rx voltage at the secondary LC tank.

The demonstrated discrete components based CDMA system will be transferred to the chip integration stage. In addition, chip identification techniques should be explored to find the way to defining different initial values in PN codes.

5.4 Summary

This chapter demonstrates the backscatter-based data communication technique for multiple passive implantable devices. This multi-node data communication system achieves 1.25Mbps data rate per node and 1mW power consumption per passive devices by implementing discrete components on an FR4 substrate. In addition, the autonomous SoC with the ASK data modulator proves the feasibility of two data carriers detection. These results suggest the new direction for passive, low-power, multi-access implantable medical devices.

The technical recommendations in this chapter focus on wireless information communication techniques and are summarised into the following two points.

• The code-division multiple access technique has higher channel capacity for narrow-band inductive powered distributed implantable medical devices than that of the time-division and

frequency-division techniques.

• The backscatter data modulation enable low power and low cost data transmitter design since the data carrier generation and mixer are not required. This modulation scheme simplifies the structure of the data transmitter, however, increases the complexity of the data receiver, particularly the backscattered power falls dramatically as the inverse fourth power of the Tx-to-Rx distance ($P_{back} \propto 1/d^4_{Tx-Rx}$).

Chapter 6

Conclusions and Future Work

"You never fail until you stop trying."

– Albert Einstein, 1879 - 1955

As Einstein stated, scientific progress develops under constant numerous efforts. With intensive research and various attempts on neural interfaces, I believe that a brain in a vat, as portrayed in science fiction media, will become a reality in the foreseeable future. In this thesis, we explore the critical technical bottlenecks of wireless link schemes in neural interfaces.

In chapter 2, we reviewed the wireless link scheme from the past to the present. We also propose and verify the feasibility of the ENGINI concept from technical aspects. However, the wireless infrastructure still faces complicated obstacles before its final application in brain integration, such as hermetic packaging, interconnection, and on-chip data compression. Apart from electromagnetic power and data transmission, ultrasound has also been proven to deliver power and communicate data successfully. Besides, optical coupling and electrochemical energy harvesting also have high potential.

6.1 Original Contributions

The contributions of each technical chapter are summarised below. The related publications about each chapter are listed in Appendix B.

Chapter 3 presents detailed methodology for modelling, simulating, fabricating and characterising mm-scale Rx coils to investigate and evaluate three different types of 2-coil inductive links. The original contributions in this chapter can be summarised in the following three quantitative points.

- Above-CMOS Rx coil with high Q-factor (24.61 at 85 MHz) provides 24.12% PTE in 12 mm air gap and 2.09% PTE through biological tissues.
- Measured CMOS Rx coil with moderate Q-factor (10.50 at 450.3 MHz) achieve 7.81% PTE in 12 mm air gap and 1.64% PTE through biological tissues.
- 2-coil inductive link characterisation with three coil types from fabrication, electrical properties aspects.

Chapter 4 proposes EM-lens enhanced inductive networks to improve received voltage and extend power coverage. In addition, the self-regulated power management mechanism is proposed and co-designed with the above-CMOS Rx coil to maximise the total PTE. Three quantitative points are summarised as follow:

- Proposed multiple-resonator enhanced wireless power transfer achieves maximum PTE 13.29% @ 433 MHz and with uniform power coverage within 182 mm^2.
- Co-design the cross-coupled rectifier with above-CMOS coil and measured the maximum PCE 68.02% at 141 MHz.
- Self-regulated power management within 128 MHz tune bandwidth and regulated voltage from 1.3 V to 1.7 V.

Chapter 5 demonstrates the prototype of the multi-node data communication scheme for distributed implants. The backscatter modulation reduces the power consumption of data transmitter and code-division multiple access enables a high channel capacity over the narrow inductively powered bandwidth.

- The 1 mW implantable wireless device with 1.25 Mbps data rate and backscatter based code division multiple access real-time data decoding platform.
- Multiple data carriers transmission and detection system in the inductive powered autonomous SoC with the FSK data modulator.

6.2 Future Work

For the existing designs and prototypes in this thesis, the technical improvement of power transmission efficiency and data communication rate will be performed based on the aspects below. First, the power transmission efficiency can be further enhanced by improving the Q factor of the Rx coils. It is feasible to etch a silicon substrate to form a suspended coil or replace it with a silicon on insulator (SOI) substrate. Second, the power carriers design, such as multiple sine inputs, has been proven to effectively increase power transmission efficiency [147]. Third, the EM-Lens in this work is a planar 2.5D structure. A 3D structure resonator array is an inevitable development direction for resonant inductive links. Additionally, an injection-locked power oscillator can realise automatic tracking of the frequency from the transmitting side [148]. Last but not least, the inherent disadvantage of the CDMA data transmission scheme has been solved by second-generation communication technology from cellular networks, and the development of WCDMA or OFDMA technology can effectively increase the communication rate.

From a high-level design perspective, three points should be considered for future work. First, flexible antenna design will become a mainstream development direction in the future. In particular, flexible antennas provide remarkable freedom for the implantation process [149].

Moreover, an in-vivo experimentation is necessary to verify the functionality of PCB or chip prototypes. Experiments in biological tissue environments will reveal the potential limitations of our current scheme, such as the start-up condition in the worst scenarios, for instance, being at the edge of power coverage due to a critical misalignment. Finally, an ambitious goal of this work is to design a wireless information and power transfer platform for general-purpose implantable medical devices.

6.3 Concluding Remarks

In the last section of my thesis, I would like to share my understanding and imagination of the wireless power and data transmission fields. The electromagnetic wireless communication techniques have profoundly affected our social life. Contemporary wireless networks are usually designed for data communication purposes. The mature mobile communication networks are currently evolving to the fifth generation. However, the current wireless power transmission standards have not reached their first generation.

Interestingly, electromagnetic waves carry both energy and information, but information and energy transmissions are traditionally treated as separate links. Thus, we imagine the future wireless network with both wireless power transmission and data communication capabilities. Low-power devices will perform wireless power harvesting and data communication simultaneously.

The current commercial products and industrial standards for wireless power transmission are only focused on near-field. There is even no industrial standard for far-field wireless power transmission. Recently, it has been considered a feasible solution for powering ultra low power devices due to the reduced power requirements of electronic devices.

Koomey [150] predicts that electronic devices will maintain the current trend of power consumption reduction within 20 years. Thus, the far-field technique might be a new opportunity for future wireless power transmission, as well as numerous challenges. Solving these challenges requires research in a wide range of disciplines, including communication theory, circuit theory,

signal processing, optimization methods, RF design, prototype and experimental verification. We believe that the wireless power transmission field will evolve rapidly in the future, and once again shape our society.

Bibliography

[1] R. Sabatowski, D. Schafer, S. M. Kasper, H. Brunsch, and L. Radbruch, "Pain treatment: A historical overview," *Current Pharmaceutical Design*, vol. 10, no. 7, pp. 701–716, 2004, [Online].

[2] The Scientist Magazine. "Animal Electricity, circa 1781: How an Italian scientist doing Frankenstein-like experiments on dead frogs discovered that the body is powered by electrical impulses,". [Online], Accessed 30 December 2019.

[3] The Burton Report. (2016, June) "the Gaiffe transcutaneous nerve stimulator". [Online], Accessed 30 December 2019.

[4] Cohen, "Richard caton (1842–1926) pioneer electrophysiologist," *Proceedings of the Royal Society of Medicine*, vol. 52, no. 8, pp. 645–651, 1959, [Online].

[5] P. S. Reif, A. Strzelczyk, and F. Rosenow, "The history of invasive EEG evaluation in epilepsy patients," *Seizure*, vol. 41, pp. 191 – 195, 2016, [Online].

[6] V. A. Sironi, "Origin and evolution of deep brain stimulation," *Frontiers in Integrative Neuroscience*, vol. 5, p. 42, 2011, [Online].

[7] A. Mudry and M. Mills, "The early history of the cochlear implant: A retrospective," *JAMA Otolaryngology–Head & Neck Surgery*, vol. 139, no. 5, pp. 446–453, 05 2013, [Online].

[8] National Institute of Neurological Disorders and Stroke. “Deep brain stimulation (DBS) for the treatment of Parkinson’s disease and other movement disorders”. [Online], Accessed 30 December 2019.

[9] U.S. Food and Drug Administration. “Humanitarian Device Exemption (HDE)”. [Online], Accessed 30 December 2019.

[10] ——. “Medtronic DBS System for Epilepsy - P960009/S219”. [Online], Accessed 30 December 2019.

[11] S. Bozinovski, M. Sestakov, and L. Bozinovska, “Using EEG alpha rhythm to control a mobile robot,” in *Proceedings of the Annual International Conference of the IEEE Engineering in Medicine and Biology Society*, Nov 1988, pp. 1515–1516 vol.3, [Online].

[12] L. R. Hochberg, M. D. Serruya, G. M. Friehs, J. A. Mukand, M. Saleh, A. H. Caplan, A. Branner, D. Chen, R. D. Penn, and J. P. Donoghue, “Neuronal ensemble control of prosthetic devices by a human with tetraplegia,” *Nature*, vol. 442, no. 7099, pp. 164–171, 2006, [Online].

[13] J. L. Collinger, B. Wodlinger, J. E. Downey, W. Wang, E. C. Tyler-Kabara, D. J. Weber, A. J. C. McMorland, M. Velliste, M. L. Boninger, and A. B. Schwartz, “High-performance neuroprosthetic control by an individual with tetraplegia,” *Lancet (London, England)*, vol. 381, no. 9866, pp. 557–564, Feb 2013, [Online].

[14] M. Elon et al., “An integrated brain-machine interface platform with thousands of channels,” *bioRxiv*, 2019, [Online].

[15] Defense Advanced Research Projects Agency. “Towards a High-Resolution, Implantable Neural Interface”. [Online], Accessed 30 December 2019.

[16] N. Statt. (2017, Apr) “Facebook is working on a way to let you type with your brain”. [Online], Accessed 30 December 2019.

[17] A. B. Schwartz, X. T. Cui, D. J. Weber, and D. W. Moran, "Brain-controlled interfaces: Movement restoration with neural prosthetics," *Neuron*, vol. 52, no. 1, pp. 205 – 220, 2006, [Online].

[18] R. Das, F. Moradi, and H. Heidari, "Biointegrated and wirelessly powered implantable brain devices: A review," *IEEE Transactions on Biomedical Circuits and Systems*, pp. 1–1, 2020, [Online].

[19] Research Briefs, CBInsights. "21 Neurotech Startups To Watch: Brain-Machine Interfaces, Implantables, And Neuroprosthetics". [Online], Accessed 30 December 2019.

[20] C. M. Michel and M. M. Murray, "Towards the utilization of eeg as a brain imaging tool," *NeuroImage*, vol. 61, no. 2, pp. 371 – 385, 2012, [Online].

[21] P. R. Kennedy, A. Hopper, C. Linker, and S. M. Sharpe, "A system for real time processing of neural signals for use as prosthetic controllers," in *1992 14th Annual International Conference of the IEEE Engineering in Medicine and Biology Society*, vol. 4, Oct 1992, pp. 1343–1344, [Online].

[22] S. Radiom, M. Baghaei-Nejad, K. Aghdam, G. A. E. Vandenbosch, L. Zheng, and G. G. E. Gielen, "Far-Field On-Chip Antennas Monolithically Integrated in a Wireless-Powered 5.8-GHz Downlink/UWB Uplink RFID Tag in 0.18-μm Standard CMOS," *IEEE Journal of Solid-State Circuits*, vol. 45, no. 9, pp. 1746–1758, Sep. 2010, [Online].

[23] E. Y. Chow, A. L. Chlebowski, and P. P. Irazoqui, "A miniature-implantable RF-wireless active glaucoma intraocular pressure monitor," *IEEE Transactions on Biomedical Circuits and Systems*, vol. 4, no. 6, pp. 340–349, Dec 2010, [Online].

[24] J. C. Barrese, N. Rao, K. Paroo, C. Triebwasser, C. Vargas-Irwin, L. Franquemont, and J. P. Donoghue, "Failure mode analysis of silicon-based intracortical microelectrode arrays in non-human primates," *Journal of Neural Engineering*, vol. 10, no. 6, p. 066014, nov 2013, [Online].

[25] F. Mazza, K. M. Szostak, P. Feng, and T. G. Constandinou, *Distributed Neural Interfaces-Challenges and Trends in Scaling Implantable Technology.* Springer, Under review, pp. 1–22, [Online].

[26] IEEE, "IEEE standard for safety levels with respect to human exposure to radio frequency electromagnetic fields, 3 kHz to 300 GHz," *IEEE Std C95.1-2005 (Revision of IEEE Std C95.1-1991)*, pp. 1–238, April 2006, [Online].

[27] Food and Drug Administration, "Information for manufacturers seeking market clearance of diagnostic ultrasound systems and transducers." *Food and Drug Administration (2008)*, pp. 1–64, September 2008, [Online], Accessed 30 December 2019.

[28] N. Mano, "A 280 μWcm^{-2} biofuel cell operating at low glucose concentration," *Chem. Commun.*, pp. 2221–2223, 2008, [Online].

[29] J. M. Roseman, J. Lin, S. Ramakrishnan, J. K. Rosenstein, and K. L. Shepard, "Hybrid integrated biological-solid-state system powered with adenosine triphosphate," *Nature*, vol. 6, p. 10070, 2015, [Online].

[30] R. Venkatasubramanian, E. Siivola, T. Colpitts, and B. O'Quinn, "Thin-film thermoelectric devices with high room-temperature figures of merit," *Nature*, vol. 413, no. 6856, pp. 597–602, 2001, [Online].

[31] E. Yoon, J. Park, and C. Yu, "Thermal energy harvesting circuit with maximum power point tracking control for self-powered sensor node applications," *Frontiers Inf. Technol. Electron. Eng.*, vol. 19, no. 2, pp. 285–296, 2018, [Online].

[32] B. Shi, Z. Li, and Y. Fan, "Implantable energy-harvesting devices," *Advanced Materials*, vol. 30, no. 44, p. 1801511, 2018, [Online].

[33] J. Katic, S. Rodriguez, and A. Rusu, "A high-efficiency energy harvesting interface for implanted biofuel cell and thermal harvesters," *IEEE Transactions on Power Electronics*, vol. 33, no. 5, pp. 4125–4134, May 2018, [Online].

[34] M. Etemadrezaei, "Chapter 22 - wireless power transfer," in *Power Electronics Handbook*, 4th ed., M. H. Rashid, Ed. Butterworth-Heinemann, 2018, pp. 711 – 722, [Online].

[35] L.-G. Tran, H.-K. Cha, and W.-T. Park, "RF power harvesting: a review on designing methodologies and applications," *Micro and Nano Systems Letters*, vol. 5, no. 1, p. 14, 2017, [Online].

[36] M. H. Ouda, M. Arsalan, L. Marnat, A. Shamim, and K. N. Salama, "5.2-GHz RF power harvester in 0.18-μm CMOS for implantable intraocular pressure monitoring," *IEEE Transactions on Microwave Theory and Techniques*, vol. 61, no. 5, pp. 2177–2184, May 2013, [Online].

[37] M. Kiani and M. Ghovanloo, "A figure-of-merit for designing high-performance inductive power transmission links," *IEEE Transactions on Industrial Electronics*, vol. 60, no. 11, pp. 5292–5305, Nov 2013, [Online].

[38] D. Ahn and M. Ghovanloo, "Optimal design of wireless power transmission links for millimeter-sized biomedical implants," *IEEE Transactions on Biomedical Circuits and Systems*, vol. 10, no. 1, pp. 125–137, Feb 2016, [Online].

[39] J. S. Ho, A. J. Yeh, E. Neofytou, S. Kim, Y. Tanabe, B. Patlolla, R. E. Beygui, and A. S. Y. Poon, "Wireless power transfer to deep-tissue microimplants," *Proceedings of the National Academy of Sciences*, vol. 111, no. 22, pp. 7974–7979, 2014, [Online].

[40] M. S. Beauchamp, M. R. Beurlot, E. Fava, A. R. Nath, N. A. Parikh, Z. S. Saad, H. Bortfeld, and J. S. Oghalai, "The developmental trajectory of brain-scalp distance from birth through childhood: Implications for functional neuroimaging," *PLOS ONE*, vol. 6, no. 9, pp. 1–9, 09 2011, [Online].

[41] U. Jow and M. Ghovanloo, "Design and optimization of printed spiral coils for efficient transcutaneous inductive power transmission," *IEEE Transactions on Biomedical Circuits and Systems*, vol. 1, no. 3, pp. 193–202, Sep. 2007, [Online].

[42] J. S. Ho, S. Kim, and A. S. Y. Poon, "Midfield wireless powering for implantable systems," *Proceedings of the IEEE*, vol. 101, no. 6, pp. 1369–1378, June 2013, [Online].

[43] P. Yeon, S. A. Mirbozorgi, J. Lim, and M. Ghovanloo, "Feasibility study on active back telemetry and power transmission through an inductive link for millimeter-sized biomedical implants," *IEEE Transactions on Biomedical Circuits and Systems*, vol. 11, no. 6, pp. 1366–1376, 2017, [Online].

[44] M. Kiani, U. M. Jow, and M. Ghovanloo, "Design and optimization of a 3-coil inductive link for efficient wireless power transmission," *IEEE Transactions on Biomedical Circuits and Systems*, vol. 5, no. 6, pp. 579–591, Dec 2011, [Online].

[45] M. Kiani and M. Ghovanloo, "The circuit theory behind coupled-mode magnetic resonance-based wireless power transmission," *IEEE Transactions on Circuits and Systems I: Regular Papers*, vol. 59, no. 9, pp. 2065–2074, Sep. 2012, [Online].

[46] M. Ettorre and A. Grbic, "A transponder-based, nonradiative wireless power transfer," *IEEE Antennas and Wireless Propagation Letters*, vol. 11, pp. 1150–1153, 2012, [Online].

[47] M. W. Baker and R. Sarpeshkar, "Feedback analysis and design of RF power links for low-power bionic systems," *IEEE Transactions on Biomedical Circuits and Systems*, vol. 1, no. 1, pp. 28–38, March 2007, [Online].

[48] D. Pozar, *Microwave Engineering*. Wiley, 2011, [Online].

[49] M. Ghovanloo, M. Kiani, and K. S. Nikita, *Inductive Coupling*. John Wiley & Sons, Inc., 2014, pp. 174–208, [Online].

[50] M. Zargham and P. G. Gulak, "Fully integrated on-chip coil in 0.13 μm CMOS for wireless power transfer through biological media," *IEEE Transactions on Biomedical Circuits & Systems*, vol. 9, no. 2, pp. 259–271, 2015, [Online].

[51] M. Mark, T. Björninen, L. Ukkonen, L. Sydänheimo, and J. M. Rabaey, "SAR reduction and link optimization for mm-size remotely powered wireless implants using segmented loop antennas," in *2011 IEEE Topical Conference on Biomedical Wireless Technologies, Networks, and Sensing Systems*, Jan 2011, pp. 7–10, [Online].

[52] A. S. Royet, J. P. Michel, B. Reig, J. L. Pornin, M. Ranaivoniarivo, B. Robain, P. de Person, and G. Uren, "Design of optimized high Q inductors on SOI substrates for RF ICs," in *2016 IEEE International Conference on Electronics, Circuits and Systems (ICECS)*, Dec 2016, pp. 324–327, [Online].

[53] J. Park, C. Kim, A. Akinin, S. Ha, G. Cauwenberghs, and P. P. Mercier, "Wireless powering of mm-scale fully-on-chip neural interfaces," in *2017 IEEE Biomedical Circuits and Systems Conference (BioCAS)*, Oct 2017, pp. 1–4, [Online].

[54] U. Jow and M. Ghovanloo, "Modeling and optimization of printed spiral coils in air, saline, and muscle tissue environments," *IEEE Transactions on Biomedical Circuits and Systems*, vol. 3, no. 5, pp. 339–347, Oct 2009, [Online].

[55] C. Kim, J. Park, S. Ha, A. Akinin, R. Kubendran, P. P. Mercier, and G. Cauwenberghs, "A 3 mm $\times$ 3 mm fully integrated wireless power receiver and neural interface system-on-chip," *IEEE Transactions on Biomedical Circuits and Systems*, pp. 1–1, 2019, [Online].

[56] M. Kiani and M. Ghovanloo, "The circuit theory behind coupled-mode magnetic resonance-based wireless power transmission," *IEEE Transactions on Circuits and Systems I: Regular Papers*, vol. 59, no. 9, pp. 2065–2074, Sep. 2012, [Online].

[57] S. A. Mirbozorgi, P. Yeon, and M. Ghovanloo, "Robust wireless power transmission to mm-sized free-floating distributed implants," *IEEE Transactions on Biomedical Circuits and Systems*, vol. 11, no. 3, pp. 692–702, June 2017, [Online].

[58] P. Yeon, S. A. Mirbozorgi, B. Ash, H. Eckhardt, and M. Ghovanloo, "Fabrication and microassembly of a mm-sized floating probe for a distributed wireless neural interface," *Micromachines*, vol. 7, no. 9, p. 154, 2016, [Online].

[59] B. Lee, D. Ahn, and M. Ghovanloo, "Three-phase time-multiplexed planar power transmission to distributed implants," *IEEE Journal of Emerging and Selected Topics in Power Electronics*, vol. 4, no. 1, pp. 263–272, March 2016, [Online].

[60] P. Yeon, S. A. Mirbozorgi, and M. Ghovanloo, "Optimal design of a 3-coil inductive link for millimeter-sized biomedical implants," in *2016 IEEE Biomedical Circuits and Systems Conference (BioCAS)*, Oct 2016, pp. 396–399, [Online].

[61] Y. Karimi, A. Khalifa, W. Montlouis, M. Stanaćević, and R. Etienne-Cummings, "Coil array design for maximizing wireless power transfer to sub-mm sized implantable devices," in *2017 IEEE Biomedical Circuits and Systems Conference (BioCAS)*, Oct 2017, pp. 1–4, [Online].

[62] J. Lee, F. Laiwalla, J. Jeong, C. Kilfoyle, L. Larson, A. Nurmikko, S. Li, S. Yu, and V. W. Leung, "Wireless power and data link for ensembles of sub-mm scale implantable sensors near 1GHz," in *2018 IEEE Biomedical Circuits and Systems Conference (BioCAS)*, Oct 2018, pp. 1–4, [Online].

[63] J. Lee, E. Mok, J. Huang, L. Cui, A. Lee, V. Leung, P. Mercier, S. Shellhammer, L. Larson, P. Asbeck, R. Rao, Y. Song, A. Nurmikko, and F. Laiwalla, "An implantable wireless network of distributed microscale sensors for neural applications," in *2019 9th International IEEE/EMBS Conference on Neural Engineering (NER)*, March 2019, pp. 871–874, [Online].

[64] P. Troyk, S. Bredeson, S. Cogan, M. Romero-Ortega, S. Suh, Z. Hu, A. Kanneganti, R. Granja-Vazquez, J. Seifert, and M. Bak, "In-vivo tests of a 16-channel implantable wireless neural stimulator," in *2015 7th International IEEE/EMBS Conference on Neural Engineering (NER)*, April 2015, pp. 474–477, [Online].

[65] P. R. Troyk, D. Bradley, M. Bak, S. Cogan, R. Erickson, Z. Hu, C. Kufta, D. McCreery, E. Schmidt, S. Sung, and V. Towle, "Intracortical visual prosthesis research - approach and progress," in *2005 IEEE Engineering in Medicine and Biology 27th Annual Conference*, Jan 2005, pp. 7376–7379, [Online].

[66] S.-I. Chang, S.-Y. Park, and E. Yoon, "Minimally-invasive neural interface for distributed wireless electrocorticogram recording systems," *Sensors*, vol. 18, no. 1, 2018, [Online].

[67] A. Khalifa, Y. Liu, Y. Karimi, Q. Wang, A. Eisape, M. Stanaćević, N. Thakor, Z. Bao, and R. Etienne-Cummings, "The microbead: A 0.009 mm3 implantable wireless neural stimulator," *IEEE Transactions on Biomedical Circuits and Systems*, vol. 13, no. 5, pp. 971–985, Oct 2019, [Online].

[68] S. A. Mirbozorgi, H. Bahrami, M. Sawan, and B. Gosselin, "A smart cage with uniform wireless power distribution in 3D for enabling long-term experiments with freely moving animals," *IEEE Trans. BioCAS*, vol. 10, no. 2, pp. 424–434, April 2016, [Online].

[69] Y. Jia, S. A. Mirbozorgi, P. Zhang, O. T. Inan, W. Li, and M. Ghovanloo, "A dual-band wireless power transmission system for evaluating mm-sized implants," *IEEE Transactions on Biomedical Circuits and Systems*, vol. 13, no. 4, pp. 595–607, Aug 2019, [Online].

[70] P. Yeon, S. A. Mirbozorgi, J. Lim, and M. Ghovanloo, "Feasibility study on active back telemetry and power transmission through an inductive link for millimeter-sized biomedical implants," *IEEE Transactions on Biomedical Circuits and Systems*, vol. 11, no. 6, pp. 1366–1376, Dec 2017, [Online].

[71] G. Lipworth, J. Ensworth, K. Seetharam, D. Huang, J. S. Lee, P. Schmalenberg, T. Nomura, M. S. Reynolds, D. R. Smith, and Y. Urzhumov, "Magnetic metamaterial superlens for increased range wireless power transfer," *Scientific Reports*, vol. 4, no. 1, p. 3642, 2014, [Online].

[72] M. Kiani and M. Ghovanloo, "A 13.56-Mbps pulse delay modulation based transceiver for simultaneous near-field data and power transmission," *IEEE Transactions on Biomedical Circuits and Systems*, vol. 9, no. 1, pp. 1–11, Feb 2015, [Online].

[73] P. D. Wolf, "Thermal considerations for the design of an implanted cortical brain–machine interface (bmi)," in *Indwelling Neural Implants: Strategies for Contending with the In Vivo Environment*, B. Raton, Ed. Boca Raton (FL): CRC Press Taylor & Francis, 2008, ch. 3, pp. 63–86, [Online].

[74] K. Agarwal, R. Jegadeesan, Y. Guo, and N. V. Thakor, "Wireless power transfer strategies for implantable bioelectronics," *IEEE Reviews in Biomedical Engineering*, vol. 10, pp. 136–161, 2017, [Online].

[75] D. Seo, R. M. Neely, K. Shen, U. Singhal, E. Alon, J. M. Rabaey, J. M. Carmena, and M. M. Maharbiz, "Wireless recording in the peripheral nervous system with ultrasonic neural dust," *Neuron*, vol. 91, no. 3, pp. 529 – 539, 2016, [Online].

[76] M. L. Wang, S. Baltsavias, T. C. Chang, M. J. Weber, J. Charthad, and A. Arbabian, "Wireless data links for next-generation networked micro-implantables," in *2018 IEEE Custom Integrated Circuits Conference (CICC)*, April 2018, pp. 1–9, [Online].

[77] S. Ozeri and D. Shmilovitz, "Ultrasonic transcutaneous energy transfer for powering implanted devices," *Ultrasonics*, vol. 50, no. 6, pp. 556 – 566, 2010, [Online].

[78] Hua Meng and M. Sahin, "An electroacoustic recording device for wireless sensing of neural signals," in *2013 35th Annual International Conference of the IEEE Engineering in Medicine and Biology Society (EMBC)*, July 2013, pp. 3086–3088, [Online].

[79] R. V. Taalla, M. S. Arefin, A. Kaynak, and A. Z. Kouzani, "A review on miniaturized ultrasonic wireless power transfer to implantable medical devices," *IEEE Access*, vol. 7, pp. 2092–2106, 2019, [Online].

[80] J. Charthad, M. J. Weber, T. C. Chang, and A. Arbabian, "A mm-sized implantable medical device (IMD) with ultrasonic power transfer and a hybrid bi-directional data link," *IEEE Journal of Solid-State Circuits*, vol. 50, no. 8, pp. 1741–1753, Aug 2015, [Online].

[81] T. Maleki, N. Cao, S. H. Song, C. Kao, S. Ko, and B. Ziaie, "An ultrasonically powered implantable micro-oxygen generator (IMOG)," *IEEE Transactions on Biomedical Engineering*, vol. 58, no. 11, pp. 3104–3111, Nov 2011, [Online].

[82] S. Ayazian and A. Hassibi, "Delivering optical power to subcutaneous implanted devices," in *2011 Annual International Conference of the IEEE Engineering in Medicine and Biology Society*, Aug 2011, pp. 2874–2877, [Online].

[83] M. Mujeeb-U-Rahman, D. Adalian, C.-F. Chang, and A. Scherer, "Optical power transfer and communication methods for wireless implantable sensing platforms," *Journal of Biomedical Optics*, vol. 20, no. 9, pp. 1 – 9, 2015, [Online].

[84] C. Ash, M. Dubec, K. Donne, and T. Bashford, "Effect of wavelength and beam width on penetration in light-tissue interaction using computational methods," *Lasers in Medical Science*, vol. 32, no. 8, pp. 1909–1918, 2017, [Online].

[85] Y. Lo, Y. Kuan, S. Culaclii, B. Kim, P. Wang, C. Chang, J. A. Massachi, M. Zhu, K. Chen, P. Gad, V. R. Edgerton, and W. Liu, "A fully integrated wireless SoC for motor function recovery after spinal cord injury," *IEEE Transactions on Biomedical Circuits and Systems*, vol. 11, no. 3, pp. 497–509, June 2017, [Online].

[86] A. Ebrazeh and P. Mohseni, "30 pJ/b, 67 Mbps, centimeter-to-meter range data telemetry with an IR-UWB wireless link," *IEEE Transactions on Biomedical Circuits and Systems*, vol. 9, no. 3, pp. 362–369, June 2015, [Online].

[87] F. Inanlou, M. Kiani, and M. Ghovanloo, "A 10.2 Mbps pulse harmonic modulation based transceiver for implantable medical devices," *IEEE Journal of Solid-State Circuits*, vol. 46, no. 6, pp. 1296–1306, June 2011, [Online].

[88] Y. Kuan, Y. Lo, Y. Kim, M. F. Chang, and W. Liu, "Wireless gigabit data telemetry for large-scale neural recording," *IEEE Journal of Biomedical and Health Informatics*, vol. 19, no. 3, pp. 949–957, May 2015, [Online].

[89] D. Jiang, D. Cirmirakis, M. Schormans, T. A. Perkins, N. Donaldson, and A. Demosthenous, "An integrated passive phase-shift keying modulator for biomedical implants with power telemetry over a single inductive link," *IEEE Transactions on Biomedical Circuits and Systems*, vol. 11, no. 1, pp. 64–77, Feb 2017, [Online].

[90] L. B. Leene, S. Luan, and T. G. Constandinou, "A 890fJ/bit UWB transmitter for SOC integration in high bit-rate transcutaneous bio-implants," in *2013 IEEE International Symposium on Circuits and Systems (ISCAS)*, May 2013, pp. 2271–2274, [Online].

[91] M. S. Chae, Z. Yang, M. R. Yuce, L. Hoang, and W. Liu, "A 128-channel 6 mW wireless neural recording IC with spike feature extraction and UWB transmitter," *IEEE Transactions on Neural Systems and Rehabilitation Engineering*, vol. 17, no. 4, pp. 312–321, Aug 2009, [Online].

[92] J. Lim, A. Rezvanitabar, F. L. Degertekin, and M. Ghovanloo, "An impulse radio PWM-based wireless data acquisition sensor interface," *IEEE Sensors Journal*, vol. 19, no. 2, pp. 603–614, Jan 2019, [Online].

[93] M. N. Islam and M. R. Yuce, "Review of medical implant communication system (mics) band and network," *ICT Express: Special Issue on Emerging Technologies for Medical Diagnostics*, vol. 2, no. 4, pp. 188 – 194, 2016, [Online].

[94] M. M. Ghanbari, D. K. Piech, K. Shen, S. Faraji Alamouti, C. Yalcin, B. C. Johnson, J. M. Carmena, M. M. Maharbiz, and R. Muller, "A sub-mm^3 ultrasonic free-floating implant for multi-mote neural recording," *IEEE Journal of Solid-State Circuits*, vol. 54, no. 11, pp. 3017–3030, Nov 2019, [Online].

[95] L. B. Leene, M. Maslik, P. Feng, K. M. Szostak, F. Mazza, and T. G. Constandinou, "Autonomous SoC for neural local field potential recording in mm-scale wireless implants," in *2018 IEEE International Symposium on Circuits and Systems (ISCAS)*, May 2018, pp. 1–5, [Online].

[96] P. Feng, P. Yeon, Y. Cheng, M. Ghovanloo, and T. G. Constandinou, "Chip-scale coils for millimeter-sized bio-implants," *IEEE Transactions on Biomedical Circuits and Systems*, vol. 12, no. 5, pp. 1088–1099, Oct 2018, [Online].

[97] P. Feng, T. G. Constandinou, P. Yeon, and M. Ghovanloo, "Millimeter-scale integrated and wirewound coils for powering implantable neural microsystems," in *2017 IEEE Biomedical Circuits and Systems Conference (BioCAS)*, Oct 2017, pp. 1–4, [Online].

[98] K. M. Szostak, F. Mazza, M. Maslik, L. B. Leene, P. Feng, and T. G. Constandinou, "Microwire-cmos integration of mm-scale neural probes for chronic local field potential

recording," in *2017 IEEE Biomedical Circuits and Systems Conference (BioCAS)*, Oct 2017, pp. 1–4, [Online].

[99] MED Institute Inc. "MRI Safety Information and Labeling (ASTM F2503),". [Online], Accessed 30 December 2019.

[100] K. Kratt, V. Badilita, T. Burger, J. G. Korvink, and U. Wallrabe, "A fully MEMS-compatible process for 3D high aspect ratio micro coils obtained with an automatic wire bonder," *Journal of Micromechanics and Microengineering*, vol. 20, no. 1, p. 015021, dec 2009, [Online].

[101] T. Dohi, K. Kuwana, K. Matsumoto, and I. Shimoyama, "A standing micro coil for a high resolution MRI," in *TRANSDUCERS 2007 - 2007 International Solid-State Sensors, Actuators and Microsystems Conference*, June 2007, pp. 1313–1316, [Online].

[102] M. J. K. Klein, T. Ono, M. Esashi, and J. G. Korvink, "Process for the fabrication of hollow core solenoidal microcoils in borosilicate glass," *Journal of Micromechanics and Microengineering*, vol. 18, no. 7, p. 075002, may 2008, [Online].

[103] A. B. Islam, "Design of wireless power transfer and data telemetry system for biomedical applications," *PhD dissertation., University of Tennessee*, 2011, [Online].

[104] Jun-Bo Yoon, Yun-Seok Choi, Byeong-Il Kim, Yunseong Eo, and Euisik Yoon, "CMOS-compatible surface-micromachined suspended-spiral inductors for multi-GHz silicon RF ICs," *IEEE Electron Device Letters*, vol. 23, no. 10, pp. 591–593, Oct 2002, [Online].

[105] G. W. Dahlmann, E. M. Yeatman, P. R. Young, I. D. Robertson, and S. Lucyszyn, "MEMS high Q microwave inductors using solder surface tension self-assembly," in *2001 IEEE MTT-S International Microwave Sympsoium Digest (Cat. No.01CH37157)*, vol. 1, May 2001, pp. 329–332 vol.1, [Online].

[106] Y. Cheng, G. Wang, and M. Ghovanloo, "Analytical modeling and optimization of small solenoid coils for millimeter-sized biomedical implants," *IEEE Transactions on Microwave Theory & Techniques*, vol. 65, no. 3, pp. 1024–1035, 2017, [Online].

[107] M. Sawan, S. Hashemi, M. Sehil, F. Awwad, M. Hajj-Hassan, and A. Khouas, "Multicoils-based inductive links dedicated to power up implantable medical devices: modeling, design and experimental results," *Biomedical Microdevices*, vol. 11, no. 5, p. 1059, 2009, [Online].

[108] S. S. Mohan, M. del Mar Hershenson, S. P. Boyd, and T. H. Lee, "Simple accurate expressions for planar spiral inductances," *IEEE Journal of Solid-State Circuits*, vol. 34, no. 10, pp. 1419–1424, 1999, [Online].

[109] C. P. Yue and S. S. Wong, "Physical modeling of spiral inductors on silicon," *IEEE Transactions on Electron Devices*, vol. 47, no. 3, pp. 560–568, 2000, [Online].

[110] I. C. H. Lai and M. Fujishima, "A new on-chip substrate-coupled inductor model implemented with scalable expressions," *IEEE Journal of Solid-State Circuits*, vol. 41, no. 11, pp. 2491–2499, 2006, [Online].

[111] X. Huo, P. C. H. Chan, K. J. Chen, and H. C. Luong, "A physical model for on-chip spiral inductors with accurate substrate modeling," *IEEE Transactions on Electron Devices*, vol. 53, no. 12, pp. 2942–2949, 2006, [Online].

[112] J. Song, S. Kim, B. Bae, J. J. Kim, D. H. Jung, and J. Kim, "Design and analysis of magnetically coupled coil structures for PCB-to-active interposer wireless power transfer in 2.5D/3D-IC," in *IEEE Electrical Design of Advanced Packaging Systems Symposium (EDAPS)*, 2014, pp. 1–4, [Online].

[113] S. Gabriel, R. W. Lau, and C. Gabriel, "The dielectric properties of biological tissues: III. parametric models for the dielectric spectrum of tissues," *Physics in Medicine & Biology*, vol. 41, no. 11, p. 2271, 1996, [Online].

[114] S. Kim, J. S. Ho, and A. S. Y. Poon, "Wireless power transfer to miniature implants: Transmitter optimization," *IEEE Transactions on Antennas & Propagation*, vol. 60, no. 10, pp. 4838–4845, 2012, [Online].

[115] P. Nayak, D. K. Schroder, D. Vasileska, M. Kozicki, and J. Aberle, "Characterization of high-resistivity silicon bulk and silicon-on-insulator wafers," *Arizona State University*, pp. 176–178, 2012, [Online].

[116] J. Zou, C. Liu, D. R. Trainor, J. Chen, J. E. Schutt-Aine, and P. L. Chapman, "Development of three-dimensional inductors using plastic deformation magnetic assembly (PDMA)," *IEEE Transactions on Microwave Theory and Techniques*, vol. 51, no. 4, pp. 1067–1075, 2003, [Online].

[117] C. P. Yue and S. S. Wong, "On-chip spiral inductors with patterned ground shields for Si-based RF ICs," *IEEE Journal of Solid-State Circuits*, vol. 33, no. 5, pp. 743–752, 1998, [Online].

[118] H. Lakdawala, X. Zhu, H. Luo, S. Santhanam, L. R. Carley, and G. K. Fedder, "Micromachined high-Q inductors in a 0.18 μm copper interconnect low-k dielectric cmos process," *IEEE Journal of Solid-State Circuits*, vol. 37, no. 3, pp. 394–403, 2002, [Online].

[119] P. A. Thadesar and M. S. Bakir, "Fabrication and characterization of polymer-enhanced TSVs, inductors, and antennas for mixed-signal silicon interposer platforms," *IEEE Transactions on Components, Packaging & Manufacturing Technology*, vol. 6, no. 3, pp. 455–463, 2016, [Online].

[120] S. A. Mirbozorgi, P. Yeon, and M. Ghovanloo, "Robust wireless power transmission to mm-sized free-floating distributed implants," *IEEE Transactions on Biomedical Circuits & Systems*, vol. 11, no. 3, pp. 692–702, 2017, [Online].

[121] Q.-A. Huang, L. Dong, and L.-F. Wang, "LC passive wireless sensors towards a wireless sensing platform: status, prospects, and challenges," *IEEE Journal of Microelectromechanical Systems*, vol. 25, no. 5, pp. 822–841, 2016, [Online].

[122] P. Yeon, J. L. Gonzalez, M. Zia, S. K. Rajan, G. S. May, M. S. Bakir, and M. Ghovanloo, "Microfabrication, assembly, and hermetic packaging of mm-sized free-floating neural probes," in *IEEE Biomedical Circuits & Systems (BioCAS) Conference*, 2017, pp. 608–611, [Online].

[123] S. Ha, A. Akinin, J. Park, C. Kim, H. Wang, C. Maier, P. P. Mercier, and G. Cauwenberghs, "Silicon-integrated high-density electrocortical interfaces," *Proceedings of the IEEE*, vol. 105, no. 1, pp. 11–33, 2017, [Online].

[124] P. Feng and T. G. Constandinou, "Robust wireless power transfer to multiple mm-scale freely-positioned neural implants," in *2018 IEEE Biomedical Circuits and Systems Conference (BioCAS)*, Oct 2018, pp. 1–4, [Online].

[125] N. Ahmadi, M. L. Cavuto, P. Feng, L. B. Leene, M. Maslik, F. Mazza, O. Savolainen, K. M. Szostak, C. Bouganis, J. Ekanayake, A. Jackson, and T. G. Constandinou, "Towards a distributed, chronically-implantable neural interface," in *IEEE/EMBS2019 on NER*, March 2019, pp. 719–724, [Online].

[126] T. Constandinou and A. Jackson, "Implantable neural interface," GB patentwo WO2 017 199 052A3, 2016, [Online].

[127] A. Kurs, A. Karalis, R. Moffatt, J. D. Joannopoulos, P. Fisher, and M. Soljačić, "Wireless power transfer via strongly coupled magnetic resonances," *Science*, vol. 317, no. 5834, pp. 83–86, 2007, [Online].

[128] C. R. Valenta and G. D. Durgin, "Harvesting wireless power: Survey of energy-harvester conversion efficiency in far-field, wireless power transfer systems," *IEEE Microwave Magazine*, vol. 15, no. 4, pp. 108–120, June 2014, [Online].

[129] B. Clerckx, R. Zhang, R. Schober, D. W. K. Ng, D. I. Kim, and H. V. Poor, "Fundamentals of wireless information and power transfer: From RF energy harvester models to signal and system designs," *IEEE Journal on Selected Areas in Communications*, vol. 37, no. 1, pp. 4–33, Jan 2019, [Online].

[130] T. T. Le, Jifeng Han, A. von Jouanne, K. Mayaram, and T. S. Fiez, "Piezoelectric micropower generation interface circuits," *IEEE Journal of Solid-State Circuits*, vol. 41, no. 6, pp. 1411–1420, June 2006, [Online].

[131] H. Nakamoto, D. Yamazaki, T. Yamamoto, H. Kurata, S. Yamada, K. Mukaida, T. Ninomiya, T. Ohkawa, S. Masui, and K. Gotoh, "A passive UHF RF identification CMOS

tag IC using ferroelectric RAM in 0.35-μm technology," *IEEE Journal of Solid-State Circuits*, vol. 42, no. 1, pp. 101–110, Jan 2007, [Online].

[132] K. Kotani, A. Sasaki, and T. Ito, "High-efficiency differential-drive CMOS rectifier for UHF RFIDs," *IEEE Journal of Solid-State Circuits*, vol. 44, no. 11, pp. 3011–3018, Nov 2009, [Online].

[133] M. Ghovanloo and K. Najafi, "Fully integrated wideband high-current rectifiers for inductively powered devices," *IEEE Journal of Solid-State Circuits*, vol. 39, no. 11, pp. 1976–1984, Nov 2004, [Online].

[134] H. Lee and M. Ghovanloo, "An integrated power-efficient active rectifier with offset-controlled high speed comparators for inductively powered applications," *IEEE Transactions on Circuits and Systems I: Regular Papers*, vol. 58, no. 8, pp. 1749–1760, Aug 2011, [Online].

[135] B. Li, X. Shao, N. Shahshahan, N. Goldsman, T. Salter, and G. M. Metze, "An antenna co-design dual band RF energy harvester," *IEEE Transactions on Circuits and Systems I: Regular Papers*, vol. 60, no. 12, pp. 3256–3266, Dec 2013, [Online].

[136] M. Stoopman, S. Keyrouz, H. J. Visser, K. Philips, and W. A. Serdijn, "Co-design of a CMOS rectifier and small loop antenna for highly sensitive RF energy harvesters," *IEEE Journal of Solid-State Circuits*, vol. 49, no. 3, pp. 622–634, March 2014, [Online].

[137] J. Yi, W. Ki, and C. Tsui, "Analysis and design strategy of UHF micro-power CMOS rectifiers for micro-sensor and RFID applications," *IEEE Transactions on Circuits and Systems I: Regular Papers*, vol. 54, no. 1, pp. 153–166, Jan 2007, [Online].

[138] H.-M. Lee and M. Ghovanloo, "Chapter 5 - energy management integrated circuits for wireless power transmission," in *Implantable Biomedical Microsystems*, S. Bhunia, S. J. Majerus, and M. Sawan, Eds. Oxford: William Andrew Publishing, 2015, pp. 87 – 111, [Online].

[139] L. Cheng, W. Ki, and C. Tsui, "A 6.78-MHz single-stage wireless power receiver using a 3-mode reconfigurable resonant regulating rectifier," *IEEE Journal of Solid-State Circuits*, vol. 52, no. 5, pp. 1412–1423, May 2017, [Online].

[140] H. Lee, C. S. Juvekar, J. Kwong, and A. P. Chandrakasan, "A nonvolatile flip-flop-enabled cryptographic wireless authentication tag with per-query key update and power-glitch attack countermeasures," *IEEE Journal of Solid-State Circuits*, vol. 52, no. 1, pp. 272–283, Jan 2017, [Online].

[141] B. Razavi, "The StrongARM latch [A Circuit for All Seasons]," *IEEE Solid-State Circuits Magazine*, vol. 7, no. 2, pp. 12–17, Spring 2015, [Online].

[142] P. Feng, M. Maslik, and T. G. Constandinou, "EM-Lens enhanced power transfer and multi-node data transmission for implantable medical devices," in *2019 IEEE Biomedical Circuits and Systems Conference (BioCAS)*, Oct 2019, pp. 1–4, [Online].

[143] B. Sklar, *Digital communications: fundamentals and applications*, 2nd ed., ser. Prentice Hall Communications Engineering and Emerging Technologies Series. Prentice-Hall PTR, 2001, pp. 656–658, [Online].

[144] T. C. Chang, M. Wang, and A. Arbabian, "Multi-access networking with wireless ultrasound-powered implants," in *2019 IEEE Biomedical Circuits and Systems Conference (BioCAS)*, Oct 2019, pp. 1–4, [Online].

[145] E. Demirors, G. Alba, G. E. Santagati, and T. Melodia, "High data rate ultrasonic communications for wireless intra-body networks," in *2016 IEEE International Symposium on Local and Metropolitan Area Networks (LANMAN)*, June 2016, pp. 1–6, [Online].

[146] J. Lee, E. Mok, J. Huang, L. Cui, A. Lee, V. Leung, P. Mercier, S. Shellhammer, L. Larson, P. Asbeck, R. Rao, Y. Song, A. Nurmikko, and F. Laiwalla, "An implantable wireless network of distributed microscale sensors for neural applications," in *2019 9th International IEEE/EMBS Conference on Neural Engineering (NER)*, March 2019, pp. 871–874, [Online].

[147] B. Clerckx and E. Bayguzina, "Waveform design for wireless power transfer," *IEEE Transactions on Signal Processing*, vol. 64, no. 23, pp. 6313–6328, Dec 2016, [Online].

[148] G. Feng and J. Sit, "Injection-locked power oscillator for resonance frequency tracking in wireless power transfer," in *2018 IEEE Biomedical Circuits and Systems Conference (BioCAS)*, Oct 2018, pp. 1–4, [Online].

[149] J. Liu, T.-M. Fu, Z. Cheng, G. Hong, T. Zhou, L. Jin, M. Duvvuri, Z. Jiang, P. Kruskal, C. Xie, Z. Suo, Y. Fang, and C. M. Lieber, "Syringe-injectable electronics," *Nature Nanotechnology*, vol. 10, no. 7, pp. 629–636, 2015, [Online].

[150] J. Koomey, S. Berard, M. Sanchez, and H. Wong, "Implications of historical trends in the electrical efficiency of computing," *IEEE Annals of the History of Computing*, vol. 33, no. 3, pp. 46–54, March 2011, [Online].

Appendix A

Abbreviations

EEG: Electroencephalography

DBS: Deep Brain Stimulation

ECoG: Electrocorticography

AP: Action Potential

LFP: Local Field Potential

IMD: Implantable Medical Device

MEA: Multielectrode Array

EM: Electromagnetic

RFID: Radio-Frequency Identification

ATP: Adenosine Triphosphate

PTE: Power Transfer Efficiency

Tx: Transmitter

Rx: Receiver

LDO: Low-Dropout Regulator

PAE: Power-Added Efficiency

PCE: Power Conversion Efficiency

VNA: Vector Network Analyser

ASK: Amplitude Shift Keying

PSK: Phase Shift Keying

FSK: Frequency Shift Keying

LSK: Load Shift Keying

TDMA: Time Division Multiple Access

FDMA: Frequency Division Multiple Access

CDMA: Code Division Multiple Access

SDMA: Space-Division Multiple Access

ENGINI: Empowering Next-Generation Implantable Neural Interfaces

Q Factor: Quality Factor

CSF: Cerebrospinal Fluid

PDMS: Polydimethylsiloxane

SRF: Self Resonant Frequency

PDD: Power Distribution Deviation

PDL: Power Delivered To Load

SAR: Specific Absorption Rate

ISM Band: Industrial, Scientific And Medical Radio Band

FSM: Finite State Machine

BGR: Bandgap Reference

WIT: Wireless Information Transmission

WPT: Wireless Power Transmission

WIPT: Wireless Information And Power Transmission

SDR: Software-Defined Radio

MCU: Microcontroller

PA: Power Amplifier

SPI: Serial Peripheral Interface

Appendix B

Publications

The related conference and journal publications that have generated or been generating from this thesis are listed below regarding the corresponding technical chapter.

- **Chapter 2**
  - F. Mazza, K. M. Szostak, **P. Feng**, T. G. Constandinou, "Distributed Neural Interfaces-Challenges and Trends in Scaling Implantable Technology," in *Handbook of Neuroengineering*. (Under review) [Online]
- **Chapter 3**
  - **P. Feng**, P. Yeon, Y. Cheng, M. Ghovanloo and T. G. Constandinou, "Chip-Scale Coils for Millimeter-Sized Bio-Implants," in *IEEE Transactions on Biomedical Circuits and Systems*, vol. 12, no. 5, pp. 1088-1099, Oct. 2018. [Online]
  - **P. Feng**, T. G. Constandinou, P. Yeon and M. Ghovanloo, "Millimeter-scale integrated and wirewound coils for powering implantable neural microsystems," *2017 IEEE Biomedical Circuits and Systems Conference (BioCAS)*, Turin, 2017, pp. 1-4. [Online]
  - K. M. Szostak, F. Mazza, M. Maslik, L. B. Leene, **P. Feng** and T. G. Constandinou, "Microwire-CMOS integration of mm-scale neural probes for chronic local field

potential recording," *2017 IEEE Biomedical Circuits and Systems Conference (BioCAS)*, Turin, 2017, pp. 1-4. [Online]

- **Chapter 4**
  - **P. Feng** and T. G. Constandinou, "Robust Wireless Power Transfer to Multiple mm-Scale Freely-Positioned Neural Implants," *2018 IEEE Biomedical Circuits and Systems Conference (BioCAS)*, Cleveland, OH, 2018, pp. 1-4. [Online]
  - L. B. Leene, M. Maslik, **P. Feng**, K. M. Szostak, F. Mazza and T. G. Constandinou, "Autonomous SoC for Neural Local Field Potential Recording in mm-Scale Wireless Implants," *2018 IEEE International Symposium on Circuits and Systems (ISCAS)*, Florence, 2018, pp. 1-5. [Online]
  - N. Ahmadi, M. L. Cavuto, **P. Feng**, L. B. Leene, M. Maslik, F. Mazza, O. Savolainen, K. M. Szostak, C. Bouganis, J. Ekanayake, A. Jackson, T. G. Constandinou, "Towards a Distributed, Chronically-Implantable Neural Interface," *2019 9th International IEEE/EMBS Conference on Neural Engineering (NER)*, San Francisco, CA, USA, 2019, pp. 719-724. [Online]
- **Chapter 5**
  - **P. Feng**, M. Maslik and T. G. Constandinou, "EM-Lens Enhanced Power Transfer and Multi-Node Data Transmission for Implantable Medical Devices," *2019 IEEE Biomedical Circuits and Systems Conference (BioCAS)*, Nara, Japan, 2019, pp. 1-4. [Online]